Ferromagnetic/nonmagnetic nanostructures for the electrical measurement of the Spin Hall effect and the detection of domain walls

van Tuong Pham

To cite this version:

van Tuong Pham. Ferromagnetic/nonmagnetic nanostructures for the electrical measurement of the Spin Hall effect and the detection of domain walls. Materials Science [cond-mat.mtrl-sci]. Université Grenoble Alpes, 2017. English. NNT : 2017GREAY026 . tel-01665346

HAL Id: tel-01665346
https://theses.hal.science/tel-01665346

Submitted on 15 Dec 2017

Communauté
UNIVERSITÉ Grenoble Alpes

THÈSE

Pour obtenir le grade de

DOCTEUR DE LA COMMUNAUTÉ UNIVERSITÉ GRENOBLE ALPES

Spécialité : NANOPHYSIQUE

Arrêté ministériel : 25 mai 2016

Présentée par

Van Tuong PHAM

Thèse dirigée par **Jean-Philippe ATTANE**, UGA,

et codirigée par **Laurent VILA**

préparée au sein du **Laboratoire Spintronique et Technologie des Composants**
dans **l'École Doctorale Physique**

Nanostructures ferromagnétiques/non-magnétiques pour la mesure électrique de l'effet Spin Hall et la détection de murs de domaine

Ferromagnetic/nonmagnetic nanostructures for the electrical measurement of the Spin Hall effect and the detection of domain walls

Thèse soutenue publiquement le **12 mai 2017**,
devant le jury composé de :

Monsieur DAFINE RAVELOSONA RAMASITERA
DIRECTEUR DE RECHERCHE, CNRS DELEGATION ILE-DE-FRANCE SUD, Rapporteur
Monsieur DAVID HALLEY
MAITRE DE CONFERENCES, UNIVERSITE DE STRASBOURG, Rapporteur
Madame STEFANIA PIZZINI
DIRECTRICE DE RECHERCHE, CNRS DELEGATION ALPES, Examinateur
Monsieur OLIVIER FRUCHART
DIRECTEUR DE RECHERCHE, CNRS DELEGATION ALPES, Président

ACKNOWLEDGMENT

After three years, today is the day: writing this note of thanks is the finishing touch on my thesis. I would like to reflect on the people who have supported and helped me so much throughout this period.

I would first like to acknowledge the thesis director **Jean-Philippe Attané (J. P. A.)** and the co-director **Laurent Vila (L. V.)** who without their participation my thesis have not been successfully conducted. Thanks to them for first bring me to France and give me the nice opportunity to work to make my PhD in CEA-Grenoble. L. V. was always beside me with his patience to help me handling the problems of the nanofabrications. L. V. spent a lot of his time on taking care of me during the three years. The door to J. P. A. office was always open whenever I ran into a trouble spot or had questions about my research or writing. Beside work, they have become my friends in the personal life. At the end, my choice has been perfectly right to come to Grenoble and work with them.

I would like to send my special thanks to **Alain Marty** for his helps and his instruction in the simulation works as same as the discussions during my PhD.

I would also like to give my thanks to **Gilles Zahnd**, **Williams Savero Torres**, and **Céline Vergnaud** for helping me in some e-beam lithography works, to **Chloé Bouard** and **Patrick Warin** for the helps in the alloy depositions, and to **Ariel Brenac** for coating my samples.

I would like to express my thanks to the people in NM group: **VILA Laurent, ATTANÉ Jean-Philippe, MARTY Alain**, **ZAHND Gilles, JAMET Matthieu, ĐẬU Minh Tuấn, RORTAIS Fabien, NOËL Paul, THIERY Nicolas, VERGNAUD Céline, BOUARD Chloé, BEIGNÉ Cyrille, NOTIN Lucien, BRENAC Ariel,** and **MOREL Robert** for creating the warm atmosphere at the laboratory with their friendship to give me motivation to go to work everyday.

I would like to acknowledge the committee of my thesis defense: **Dafiné Ravelosona**, **David Halley**, **Stefania Pizzini**, and **Olivier Fruchart**. Thanks to the committee for reviewing carefully the manuscript, for attending to my defense presentation and gave the nice comments and remarks.

I would like to thank my **colleagues and friends at SPINTEC** for their collaboration and sharing with me the laboratory life.

I would also like to send my thanks to the people in charge of the administration at SPINTEC, the heads and the secretary team, for their helps.

I would like to acknowledge the financial grant of **LANEF**, the "ANR- 13-BS10-0005-01" **SOspin project**, and the **Platforme Technologie Amont in Grenoble** and the support of the **Renatec network**.

Last but not least, I would like to send my thanks to **my parent** and **my family** in Vietnam, who always encourage me with their belief and their love.

TITRE: *Nanostructures ferromagnétiques/non-magnétiques pour la mesure électrique de l'effet Hall de spin et la détection de parois magnétiques*

RÉSUMÉ: La spin-orbitronique est basée sur l'utilisation de l'interaction spin-orbite pour réaliser la conversion directe ou inverse de courants de charge en courants de spin. L'évaluation de l'efficacité de cette conversion est un problème central : le besoin de développer des méthodes de mesure directes de cette conversion apparaît aujourd'hui comme l'un des défis majeurs de l'électronique de spin.

Cette thèse porte sur l'étude d'une nouvelle nanostructure permettant de caractériser l'effet Hall de spin, et sur la détection de parois magnétiques dans des nanofils par effet Hall de spin direct et inverse. Le premier chapitre présente certains concepts de base en spintronique, ainsi que l'état de l'art concernant la détection de l'effet Hall de spin. Le second chapitre présente une nanostructure ferromagnétique/non-magnétique, dans laquelle il est possible de réaliser la conversion courant de charge-courant de spin. Cette nanostructure est utilisée pour mesurer l'angle de Hall de spin et la longueur de diffusion de spin du Pt. La même méthode permet dans le troisième chapitre de caractériser l'effet Hall de spin dans différents métaux, et dans des alliages à base d'Au. Le quatrième chapitre met en évidence l'importance du rôle de l'interface ferromagnétique/non-magnétique, montrant qu'elle est particulièrement importante dans le cas du système NiFe/Pt. Enfin, le dernier chapitre présente une nouvelle méthode permettant de détecter électriquement des parois de domaines magnétiques, et basée sur l'effet Hall de spin direct ou inverse.

TITLE: *Ferromagnetic/nonmagnetic nanostructures for the electrical measurement of the spin Hall effect and the detection of domain walls*

ABSTRACT: Spin−orbitronics is based on the ability of spin−orbit interactions to achieve the conversion between charge currents and pure spin currents. As the precise evaluation of the conversion efficiency becomes a crucial issue, the need for straightforward ways to observe this conversion has emerged as one of the main challenge in spintronics. This thesis focuses on the study of a new electrical device to characterize the spin Hall effect, and on the detection of magnetic domain walls in nanowires using the direct or the inverse spin Hall effect. The first chapter describes basic spintronic concepts and the state-of-the-art concerning the spin Hall effect detection. In the second chapter, a new ferromagnetic/nonmagnetic nanostructure is proposed, in which it is possible to realize the spin-charge interconversion. This nanostructure is used to quantify the spin Hall angle and the spin diffusion length of Pt. The same technique is then used in the third chapter to characterize the spin Hall effect in different metals and Au-based alloys. The fourth chapter focuses on the role of the ferromagnetic/nonmagnetic interface, which is in particular found to be very important in the NiFe/Pt system. In the last chapter of this thesis, a new method is presented to detect electrically magnetic domain walls by direct or the inverse spin Hall effect.

Contents

Page

Acronyms

AMR	:	Anisotropy magnetoresistance
DMI	:	Dzyaloshinskii-Moriya interaction
DW	:	Domain wall
EHE	:	Extraordinary Hall effect
FEM	:	Finite element method
FM	:	Ferromagnetic material
F/M	:	Ferromagnetic/Nonmagnetic
GMR	:	Giant magnetoresistance
ISHE	:	Inverse spin Hall effect
LLGS	:	Landau–Lifshitz–Gilbert–Slonczewski
LSV	:	Lateral spin valve
MMR	:	Magnon magnetoresistance
MR	:	Magnetoresistance
NM	:	Nonmagnetic material
PSC	:	Pure spin current
SHE	:	Spin Hall effect
SMR	:	Spin Hall magnetoresistance
SOC	:	Spin orbit coupling
SOT	:	Spin orbit torque
SP-FMR	:	Spin pumping - Ferromagnetic resonance
ST-FMR	:	Spin torque - Ferromagnetic resonance
STT	:	Spin transfer torque
TMR	:	Tunneling magnetoresistance

INTRODUCTION

Spintronics is a field of modern solid-state physics, focusing on the manipulation of the spin rather than the charge of carriers[1,2,3]. Spintronic devices are foreseen as candidates for new generations of the computational devices. Beyond hard disk drives, that have allowed the rise of the age of big data, spintronics can indeed provide new ways to store, carry and control information. The advantage of spintronics is to gather in a single device those multiple functionalities, while ensuring the non-volatility of information, a low heat consumption, or a high speed of data processing and information transfer[4].

Magneto-resistances

Up to now, the backbone of spintronics is based on magnetoresistance (MR) effects, a term widely used to refer to the change of resistance of materials under the presence of a magnetic field. The first MR was discovered in 1857 by W. Thomson (Lord Kelvin) in Nickel and Iron[5].This type of MR, the anisotropic MR (AMR), depends on the angle between the electric current and the direction of magnetization in a magnetic material. It has been explained much later, in 1975, by Mc Guire and Potter[6], who considered the combined actions of the magnetization direction and of the spin orbit interaction.

A decade afterwards, the discovery of giant magnetoresistance (GMR) by A. Fert and P. Grünberg (2007 Nobel Prize), has been a breakthrough to accelerate the development of applications based on magnetoresistance effects. The GMR, which corresponds to the large resistance dependence of a magnetic multilayer with the relative magnetization direction within the layers, is considered to be the birth point of spintronics.

Unlike the AMR, which relies on the sole properties of a magnetic material, the GMR appears only in heterostructures. Indeed, a structure composed of ferromagnetic layers separated by nonmagnetic layers is needed to observe the GMR. This has been achieved thanks to the development in the 80's of thin film deposition technologies, as the layers have to be around one nanometer thick.

To maximize the resistance change, one has to tailor the change from a parallel to an antiparallel magnetization state of the layers. At first, this was done using the anti-ferromagnetic coupling between the layers, but soon the concept of spin valves has been developed, using the exchange-bias coupling with anti-ferromagnetic materials, thus allowing the development of much efficient read-head for hard disk drives[7]. Using spin valves made from the stacking of advanced materials, the GMR can reach up to 1000%[8].

Besides GMR the tunnel magnetoresistance (TMR)[9] appears in magnetic tunnel junctions (MTJ)[10] made of an ultra-thin insulating layer, sandwiched by two ferromagnetic thin films. As for the GMR, but usually with a much higher MR ratio, the TMR relies on how spin polarized currents can flow in the magnetic heterostructure, and depends on the relative orientation of the magnetization. The TMR reaches 604% at room temperature (of the order of 1100% at 2K) in state-of-the art crystalline CoFeB/MgO/CoFeB structures[11], which can be compared to the 100% GMR of the best metallic tri-layer spin-valves.

GMR and TMR are at the basis of read-heads of hard disk drives, and of the first Magnetic Random Access Memeory (MRAM) concepts[12]. They remain at the basis of the second generation of spintronics devices based on the Spin Transfer Torque (STT) and Spin Orbit Torque (SOT) phenomena to achieve reading operations.

Proposed by Slonczewski in 1996[47], the STT can be seen as the reciprocal effect of the GMR/TMR. It is based on the possibility for the angular momentum carried by the electrons to exert a torque, by transfer of the angular momentum, on a ferromagnetic layer, and therefore to modify its magnetization orientation. It can lead to magnetic oscillations (as in STT Oscillators) or to magnetization switching. The STT phenomena can thus be used to write information in the soft layer of a spin valve or of a MTJ-based device. It can then be combined to the GMR or to the TMR, which allow reading the magnetization state. This has triggered the development of a new type of magnetic memory device, called the Spin Transfer Torque MRAM (STT-MRAM)[50-55]. The STT also allows acting on magnetic textures such as domain walls (DWs) or skyrmions, which is highly promising for storage devices such as the racetrack memory[164] or DW-MRAMs[62,63].

Recently appeared another way to exert a torque on the magnetization: the use of Spin Orbit Torques (SOT). The torque is based on the Spin-Orbit-Coupling (SOC) of nonmagnetic materials such as Pt. There are basically two main effects, the Spin Hall[75] and Rashba[25,26] effects, occurring in the bulk or at the interfaces of materials, respectively. Discovered in Pt/Co/AlOx layers[65], SOTs appears to be a very efficient way to manipulate the magnetization of nanoscale magnets, inducing switching, spin waves excitation, or DW motion. Together with the STTs, the SOTs are playing a very important role in spintronic research, allowing the development of new generation of devices such as SOT-RAMs[13].

The key of the SOT is the generations of pure spin currents (PSCs), in the bulk of nonmagnetic layers with strong SOC and/ or at interfaces. Recently, the SOTs, the SHE, the Rashba effect, the conversion in topological insulators and other SOC-based effects have been gathered into a new research area: the spinorbitronics[84].

One of the key spinorbitronic phenomenon is the SHE. Whereas in conventional spintronics the exchange interaction in ferromagnetic materials is used to spin-polarize the charge current, spin currents can be generated directly in the bulk of nonmagnetic materials using this effect. The SHE possesses a reciprocal effect, the inverse spin Hall effect (ISHE), which allows converting spin currents into charge currents. These effects could provide the possibility to develop spintronic devices without ferromagnetic materials. They are particularly interesting in the field of magnonics and spincaloritronics, for instance to generate and detect the magnonics currents. Moreover, they possess an advantage over the spin valves and tri-layers structures used for STT: in the SHE the source of the angular momentum is in contact with the ferromagnetic materials, and the polarization of the spin accumulation can be more easily made perpendicular to the magnetization, thus improving the efficiency of the torque.

Although the theory of SHE has been predicted by M. I. Dyakonov and V. I. Perel in 1971[27], the first experimental observation has been realized recently by Y. K. Kato *et al.* in 2004[79], in a semiconductor and using the magneto-optical Kerr effect. This work has triggered the development of SHE experiments in various materials, like metals and graphene[84.] One difficulty with the SHE is that the spin accumulation is generated without charge accumulation (contrarily, for instance, to the extraordinary Hall effect), which means that complex characterization techniques have to be developed.

Optical methods are proper to characterize the SHE in semiconductors possessing long spin diffusion lengths, but heavy metals having strong SOC[37] have short spin diffusion lengths. This is particularly important for using the SHE to create SOTs, since to obtain strong torques and robust devices it is necessary to obtain high conversion rates and high conductivities.

Since the first experiment in 2004, several characterization techniques have been developed. The spin-pumping ferromagnetic resonance technique (SP-FMR), proposed by Y. Tserkovnyak *et al.* in 2002[90] has been used for the first time by Saitoh *et al*. in 2006[91], and the Spin Transfer ferromagnetic resonance (ST-FMR), proposed by K. Ando *et al.* in 2008[92], has been used by Liu *et al* in 2011[93].

Non local measurement in lateral spin valves (LSV) have been developed by S. O. Valenzuela and M. Tinkham in 2006[76] to characterize the SHE in Aluminum. T. Kimura *et al.* in 2007[130] adapted this approach to characterize the SHE of materials with strong spin orbit coupling and thus short spin diffusion lengths.

More recently, other transport techniques such as the Spin Hall Magnetoresistance (SMR)[118] have also been used to measure the SHE. Large efforts have been devoted to develop purely electrical ways of detecting the conversion, primarily for the sake of simplicity and versatility, but also because the long-term objective is to implement SO effects into spintronic nano-devices. Nonetheless, there exist a large discrepancy in the data analysis, from technique to technique and from group to group, even for a reference material such as Pt.

The main aim of this thesis is to propose a new electrical detection technique of the SHE. This technique is applied to characterize the SHE in spin Hall materials of heavy metals, their alloys, and the influence of the F/N interfaces. This thesis also focuses on an electrical device which allows detecting electrically magnetic DWs using the SHE or the ISHE.

This manuscript is divided into five Chapters:

Chapter I: State-of-the-art of the charge current/spin current interconversion using the Spin Hall effect

This chapter will briefly describe the background and the state of the art concerning SHE measurements. In particular, some basic concepts related to the spin dependent transport will be presented, such as the two current model, spin currents, the SOC, and the SHE. The state-of-the-art concerning SHE detection will then been discussed.

Chapter II: Nanostructure for SHE detection on platinum

We will investigate a simple device for the SHE characterization, akin to the ferromagnetic/nonmagnetic bilayers used in most spin–orbit torques experiments, and consisting of a SHE wire connected to two transverse ferromagnetic electrodes. This system allows probing electrically the direct and inverse conversion in a SHE system, and measuring both the spin Hall angle and the spin diffusion length. Care will be taken to disentangle possible artifacts while aiming at characterizing the SHE of Pt.

Chapter III: Application of the spin-charge interconversion nanostructure to characterize the SHE/ISHE in different materials

We will apply the proposed measurement technique to several SHE materials (Pd, Au, Ta, W, AuW, and AuTa), showing that it represents a promising tool for the metrology of spin–orbit materials.

Chapter IV: Interface effects in spin-charge interconversion nanostructures

Exploiting the proposed measurement technique, we will compare the values of the effective spin Hall angle of Pt measured using CoFe, Co, and NiFe electrodes. The results show that interfaces play a significant role. We will then study the effect of a Cu layer insertion in-between the ferromagnetic and SHE layers.

Chapter V: Domain wall detection by direct and inverse SHE

We will demonstrate an electrical detection method, based on the ability for a ferromagnetic nanowire, in which a DW is pinned, to inject or detect pure spin currents. The detection is based on the SHE in a F/N nanostructure, and provides an electrical way to study the DW motion in a device here again akin to the ferromagnetic/SHE bilayers typically used for spin-orbit torques experiments.

CHAPTER I: STATE-OF-THE-ART OF THE CHARGE CURRENT/SPIN CURRENT INTERCONVERSION BY SPIN HALL EFFECT

This chapter will briefly describe the state-of-the-art concerning SHE measurements, and introduce a few spintronic concepts related to the spin-dependent transport. We will firstly introduce the two-current model, and the concepts of spin accumulation and spin currents. Secondly, we will present the origin and methodology of the SHE. Thirdly, we will briefly discuss the link between SOTs, SHE and Rashba effect. Finally, we will present the state-of-the-art concerning the measurement techniques of the spin/charge interconversion.

I. 1. Two-current model and spin accumulation at a F/N interface

Two-current model

The two-current conduction model proposed by Mott[14] is a major groundwork for the study spin transport, applied by Fert and Campbell[15,16] to investigate specific behaviors in the conductivity of the ferromagnetic metals Fe, Ni, Co, and of their alloys, it provides a simple explanation of most of the electrical properties of transition metals.

In this model, the electric transport in ferromagnetic materials is mostly due to *s* electrons, whereas the electric resistivity is produced by the scattering processes suffered by the electrons between the *s* and *d* states, and during which the spin is conserved. Thus, in this model, the high resistivity of transition metals with partial filled *d*-states is explained by the dominant scattering of *s* electrons on the available *d* states.

The electrical current is supposed to be carried in parallel by the spin up and down electrons, without mutual interaction. Therefore, electrical conductivities can be defined for each spin population. In the following, they will be denoted $\sigma_\uparrow$ and $\sigma_\downarrow$ for the majority and minority spin populations, respectively. As the currents flow in parallel, the total conductivity of the system is given by the sum of both conductivities ($\sigma = \sigma_\uparrow + \sigma_\downarrow$). Using Drude's model, the electrical conductivities for each channel can be written:

$$\sigma_\uparrow = \frac{n_\uparrow e^2 \tau_\uparrow}{m_e} = \alpha_F \sigma \tag{I. 1}$$

$$\sigma_\downarrow = \frac{n_\downarrow e^2 \tau_\downarrow}{m_e} = (1 - \alpha_F)\sigma \tag{I. 2}$$

where m_e, e and $n_{\uparrow/\downarrow}$ are the electron mass, the electron charge and the number of the majority/minority electrons, respectively. $\tau_{\uparrow/\downarrow}$ are relaxation-times (relevant to the mean free path of electrons) of the majority/minority electrons. Minority and majority electrons refer to the dominant up or down spins of the partially filled 3d electron band structure. If the minority electrons are more efficiently scattered, then $\tau_\uparrow > \tau_\downarrow$. The dimensionless factor $0 \leq \alpha_F \leq 1$ accounts for the asymmetrical conductivity carried by each channel.

In ferromagnets $\alpha_F \neq 0.5$, whereas $\alpha_F = 0.5$ stands for nonmagnetic materials where $\sigma_\uparrow = \sigma_\downarrow$. In a ferromagnetic material, the spin polarization of the electrical current p_F reflects the spin asymmetry of the conductivity in the material. It can be written:

$$p_F = \frac{\sigma_\uparrow - \sigma_\downarrow}{\sigma_\uparrow + \sigma_\downarrow} = 2\alpha_F - 1$$

(I. 3)

The current for each spin population can be written:

$$J_\uparrow = \frac{\sigma_\uparrow}{e}\frac{\partial \mu_\uparrow}{\partial x};\ J_\uparrow = \frac{\sigma_\downarrow}{e}\frac{\partial \mu_\downarrow}{\partial x}$$

(I. 4)

Where the *x* axis is along the current flow, and $J_{\uparrow/\downarrow}$ are the spin up/spin down current densities. When $J_\uparrow \neq J_\downarrow$, there is a spin current density $J_s = J_\uparrow - J_\uparrow$ flowing in the magnetic materials, whereas the charge current density is $J_C = J_\uparrow + J_\downarrow$ see *Fig. I. 1(a)*.

In non-ferromagnetic materials, $p_F = 0$, so that in principle, at equilibrium, the spin current is zero in non-magnetic materials. However, under spin current injection, or in a SHE paramagnetic material, this is not the case anymore. Eventually, the same amount of spin-up and spin-down electrons flow in opposite direction, $J_\uparrow = -J_\downarrow$, leading to the flow of a Pure Spin Current (PSC).

Valet-Fert model, spin accumulation and spin diffusion length

The quantity $\mu_{\uparrow/\downarrow}$ in (*I. 4*) is the electrochemical potentials for each spin population. The transport equations can be expressed in terms of macroscopic quantities, as long as the electron mean free path (l_s) remains smaller than the spin diffusion length (λ_s).

In the limit of $\lambda_s \gg l_s$ the equations of transport are[17]

Ohm's law:

$$\frac{\partial \mu_{\uparrow/\downarrow}}{\partial x} = \frac{e}{\sigma_{\uparrow/\downarrow}} j_{\uparrow/\downarrow}$$

(I. 5)

Diffusion equation:

$$\frac{\partial^2}{\partial x^2}\,(\mu_\uparrow - \mu_\downarrow) = \frac{(\mu_\uparrow - \mu_\downarrow)}{\lambda_s^2}$$

(I. 6)

Equation (I. 5) is Ohm's law for the two currents with different spin-direction. $\sigma_{\uparrow/\downarrow}$, $\partial\mu_{\uparrow/\downarrow}$, and $\lambda_{\uparrow/\downarrow}$ are the conductivities, electrochemical potentials and the spin diffusion lengths for each spin population, respectively.

The general solution of this differential equation can be written:

$$\mu_{\uparrow/\downarrow} = (1 - {p_F}^2)\rho^* J_c x + k_1 \pm (1 \pm p_F)\left[k_2 e^{\frac{x}{\lambda_s}} + k_3 e^{-\frac{x}{\lambda_s}}\right]$$

(I. 7)

Here, the constant coefficients k1/2/3 depend on the boundary conditions, which are given by the continuity of the electrochemical potentials and the conservation of the charge and spin currents. ρ^* is the effective resistivity defined as $\rho^* = \rho/(1 - p_F^2)$.

We define the spin accumulation as the difference between the electrochemical potentials of major- and minor-spin electrons, $\Delta\mu = \mu_\uparrow - \mu_\downarrow$. Then, a 1-dimension solution of the diffusion equation (I. 6) for the spin accumulation is:

$$\Delta\mu = Ae^{-x/\lambda_s} + Be^{x/\lambda_s}$$

(I. 8)

Where the constant coefficients A and B depend on the boundary conditions.

The charge current is the total of the spin flows, $J_C = J_\uparrow - J_\downarrow$, and combining equations (I. 5) and (I. 6) the diffusion can be written as:

$$\frac{\partial^2 \Delta\mu}{\partial x^2} = \frac{\mu_s}{\lambda_s^2} \;\; or \;\; \frac{\partial^2}{\partial x^2}\,(\mu_\uparrow - \mu_\downarrow) = \frac{(\mu_\uparrow - \mu_\downarrow)}{\lambda_s^2}$$

(I. 9)

Note that λ_s is the "average" spin diffusion length, *i.e.*, the average distance that electrons diffuse between spin-flipping collisions.

An example of application of the Valet-Fert-model

In order to present the main ingredients used to describe the spin transport in this manuscript, let us use the Valet-Fert model to calculate the spin accumulation and spin current at the vicinity of a simple ferromagnetic/non-magnetic interface. Let us now discuss the simple case of a current flowing through a F/N interface, as shown in *Fig. I. 1*(a).

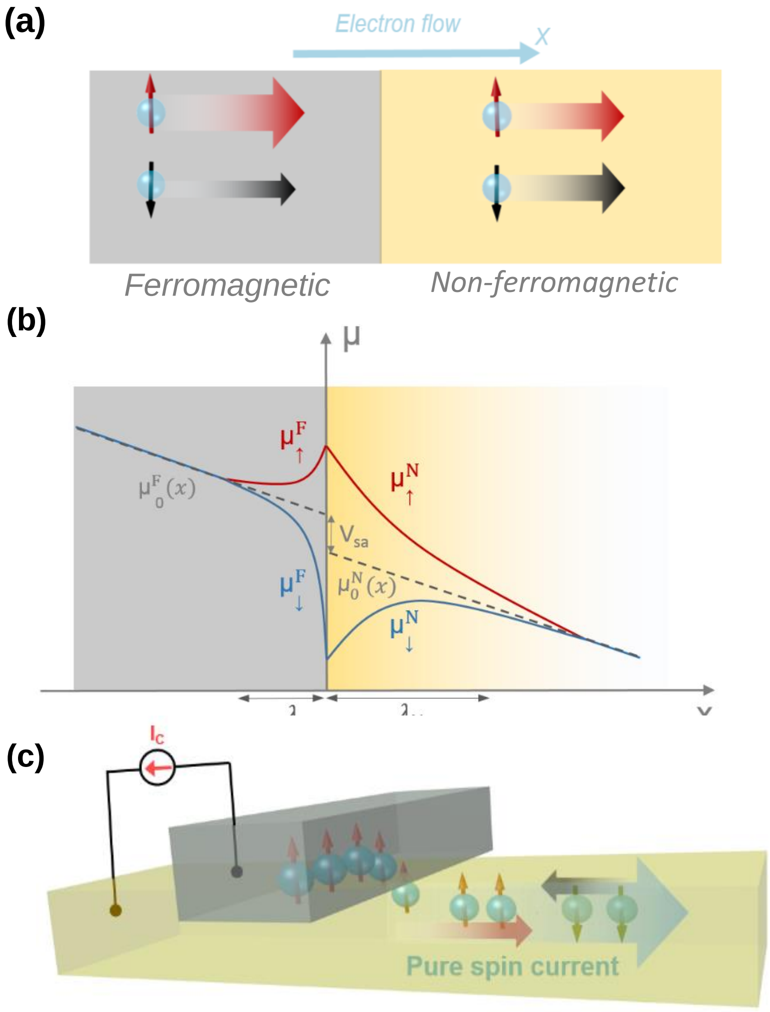

Fig. I. 1. ***F/N junctions with transparent interfaces***: *(a) Schematic representation of the F/N junction and of the current flow. In this case, the spin polarized current is* *injected from the ferromagnetic to the non-ferromagnetic materials. The red and black arrows denote the conductivities for up and down spin electrons, respectively. (b) Schematic representation of the electrochemical landscape along the F/N junction, for an electrical current along the x direction. Here, the red and blue lines represent the electrochemical potentials for the majority and minority spin populations. The transition from the ferromagnet to the non-magnet corresponds to a voltage drop at the interface, due to the spin accumulation, and denoted* V_{ac}*. (c) Example of PSC injection: PSC flowing in a nonmagnetic material, created by the nearby charge injection in a lateral spin valve*[18]*.*

The spin polarization of the current decreases during its propagation in the medium, so that far from the interface the equilibrium state of spin up and spin down electrons is reached, with a polarization equal to p_F in the ferromagnet and equal to zero in the nonmagnet. Because of the difference of polarization between the two materials, the vicinity of the F/N interface is occupied by a non-equilibrium accumulation of spin-up (and a deficit of spin-down), which is directly related to the difference of the electrochemical potentials, *i.e.*, the local spin accumulation at the interface[19].

I. 2. Origin and phenomenology of the SHE

I. 2. 1. Spin-orbit coupling

Relativistic origin of SOC

According to the Lorentz transformations of special relativity (or more precisely to the Joules-Bernoulli transformations), a change of frame can transform an electric field into a magnetic field, and vice-versa[20]. Thus, an electron moving in the laboratory frame at a velocity non-negligible with respect to the light velocity, and submitted to an electric field, will experience in his own frame, a magnetic field. The electric field therefore transforms into a relativistic magnetic field, due to the electron momentum and which can interact with the spin angular momentum of the electron (*Fig. I. 2*).

This physical phenomenon is the so-called spin-orbit coupling (SOC), and helps in particular explaining degeneracy lifts in atoms, molecules, and solids. Recently the interest towards the SOC has been increasing in solid-state physics, with a focus on several systems in which an electric field can appear, due to a non-centrosymmetric crystallographic phase, or to a symmetry breaking by a surface or an interface.

In electron band-structure calculations, the nonrelativistic equation of the electron is usually applied firstly, and then the relativistic correction, a spin-dependent term (an additional Hamiltonian), can be added in order to consider the band splitting of spin up and spin down states of electrons. In this approach the SOC can be considered as a relativistic correction. In other words, from the comparison between the nonrelativistic Schrodinger equation and the relativistic Schrodinger equation (Dirac equation) emerges an additional Hamiltonian due to the SOC.

Effect of SO in atoms

In order to approach the physics of SOC, let us first consider the problem of an electron moving in a potential in atom. Firstly, the Hamiltonian of a classical free particle moving, with the velocity $\mathbf{v}(t)$, in vacuum, is simply given by its kinetic energy, so that if

$$\boldsymbol{p} = m_e \mathbf{v}(t)$$

(I. 10)

then

$$H = \frac{\boldsymbol{p}^2}{2m_e}$$

(I. 11)

where m_e is the rest mass and $\mathbf{r}(\mathrm{t})$ is the orbit of the electron, with $\mathbf{v}(\mathrm{t}) = {}^{\partial \mathbf{r}(\mathrm{t})}/_{\partial \mathrm{t}}$.

Let us now consider an electron moving in the bound of an atom frame (*Fig. I. 2*), where there is actually no magnetic field. The relativistic Hamiltonian can be rewritten as:

$$H = \frac{\boldsymbol{p}^2}{2m_e} + \Delta H$$

(I. 12)

The relativistic correction can be deduced from the effective magnetic field given by Joules-Bernoulli equations and which acts on the electron spin.

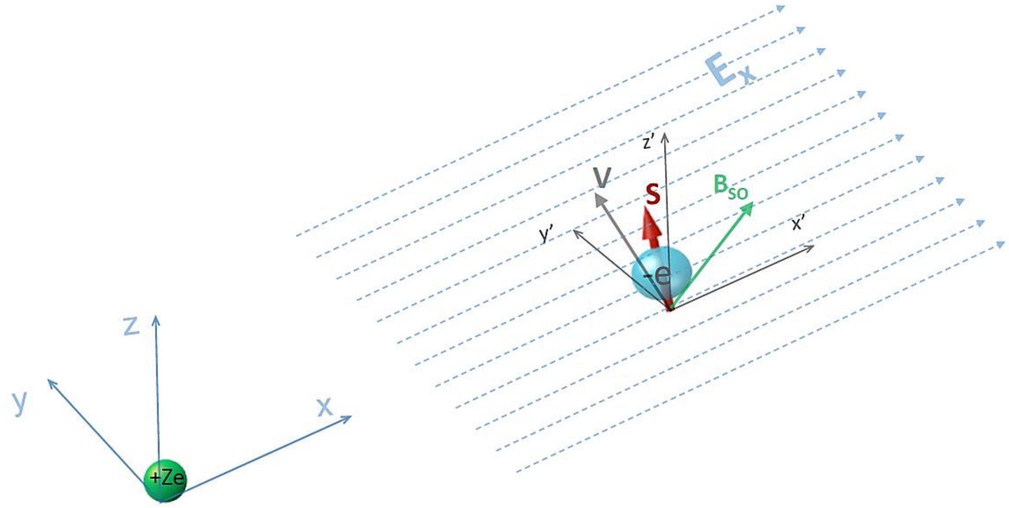

Fig. I. 2. *Spin orbit coupling: a moving electron in the electric field* ***E*** *of the nuclei experiences (or 'feel') a magnetic field* ***B_{SO}*** *in its frame, that arises from the Lorentz transformation of the static (external) electric field* ***E****, and that couples with the momentum* ***S*** *of the spin electron.*

From the Joules-Bernoulli equation, when considering the relativistic transformation of two inertial frames (the nuclear frame to the electron frame), the electron in its frame experiences the electric field **E** due to the nuclei as an effective magnetic field **B** in the perpendicular direction:

$$\boldsymbol{B} = \gamma(\mathbf{B_0} - \frac{1}{c^2}\mathbf{v}\times \mathbf{E}),$$

(I. 13)

Where $\gamma = \sqrt{1 + v^2/c^2}$ is the Lorentz factor and **B_0** = **0** is the actual magnetic field of the nuclei acts on the electron. The effective SO magnetic field is

$$\boldsymbol{B_{so}} = -\gamma\frac{1}{c^2}\mathbf{v}\times \mathbf{E}$$

(I. 14)

where $\mathbf{E} = -\frac{\mathbf{r}\,\partial \mathrm{V(r)}}{\mathrm{r}\,\partial \mathrm{r}} = -\frac{\mathbf{r}\,\partial \mathrm{U(r)}}{\mathrm{er}\,\partial \mathrm{r}}$, with $\mathrm{U(r)} = eV(r)$ the electron potential energy.

As $\mathbf{v} = \frac{\boldsymbol{p}}{m_e}$, the SO field can be written

$$\boldsymbol{B_{so}} = \gamma \frac{1}{m_e e c^2} \left(\frac{d\mathrm{U}(r)}{dr} \right) \frac{1}{r} \mathbf{r} \times \mathbf{p}$$

$$= \gamma \frac{1}{m_e e c^2} \frac{1}{r} \left(\frac{d\mathrm{U}(\mathbf{r})}{dr} \right) \boldsymbol{L}$$

(I. 15)

where **L** is the orbital momentum.

The electron possesses a magnetic moment due to its spin,

$$\boldsymbol{\mu_S} = -g_S \mu_B \frac{\boldsymbol{S}}{\hbar}$$

(I. 16)

where **S** is the spin angular momentum vector or spin, g_s is the electron spin g-factor, and μ_B is the Bohr magneton.

The correction is defined as the coupling of the effective value of relativistic B field and spin, SOC term, and can be simply seen as the Zeeman effect[22] due to the SO magnetic field

$$\Delta H = -\boldsymbol{\mu}.\boldsymbol{B_{so}}$$

(I. 17)

The correction is thus

$$\Delta H = \frac{\gamma \mu_B g_s}{\hbar m_e e c^2} \frac{1}{r} \left(\frac{d\mathrm{U}(r)}{dr} \right) \boldsymbol{L}.\boldsymbol{S}$$

(I. 18)

To sum up, another term appears, *the Thomas precession of the relativistic correction*[21], which takes into account that the spin precession frequency in the magnetic field changes when changing the frame of reference.

$$\Delta H_T = -\frac{\gamma g_s \mu_B}{2\hbar e m_e c^2} \frac{1}{r} \left(\frac{d\mathrm{U}(r)}{dr} \right) \boldsymbol{L}.\boldsymbol{S}$$

(I. 19)

Finally, the total spin–orbit Hamiltonian can be written

$$\Delta H_{SO} \equiv \Delta H + \Delta H_T = \frac{\gamma g_s \mu_B}{2\hbar e m_e c^2}\frac{1}{r}\left(\frac{dU(r)}{dr}\right)\boldsymbol{L}.\boldsymbol{S}$$

(I. 20)

If $\gamma \approx 1$ (at slow speed), $g_s \approx 2$, and $\mu_B = \frac{e\hbar}{2m_e}$. The SOC Hamiltonian is[22],

$$\Delta H_{SO} = \frac{1}{2m_e^2 c^2}\left(\frac{dU(r)}{rdr}\right)\boldsymbol{L}.\boldsymbol{S}$$

(I. 21)

This term can be interpreted as follows: when there is a gradient of potential, that is, an electric field, a coupling appears between the orbital momentum and the spin direction.

Existence of the SOC in different systems

A strong atomic SOC can appear in heavy metals (Pt, Ta, Pd…)[23]. The SOC in solids can appear in the bulk of heavy metals, or by symmetry breaking of the potential in the lattice or at interfaces/surfaces. The symmetries of a crystal can include the time-reversal symmetry (the wave function is unchanged in the t -> – t transformation) and the inversion symmetry (the Hamiltonian is unchanged in the **r** -> – **r** transformation). The presence of those symmetries implies that the eigenvalue satisfies the condition $E(\boldsymbol{k},\uparrow) = E(\boldsymbol{k},\downarrow)$, where **k** denotes the electron wave-vector, and ↑/↓ corresponds to the spin direction.

In materials lacking of the inversion symmetry, only the time-reversal symmetry is satisfied: $E(\boldsymbol{k},\uparrow) = E(-\boldsymbol{k},\downarrow)$ but $E(\boldsymbol{k},\uparrow) \neq E(-\boldsymbol{k},\uparrow)$ and $E(\boldsymbol{k},\downarrow) \neq E(-\boldsymbol{k},\downarrow)$, so that a **k**-dependent spin-splitting of the electron band can occur.

The SOC can thus be obtained in the bulk of solids, or at surfaces and interfaces of solid, providing that the inversion symmetry is broken. The inversion asymmetry in noncentrosymmetric crystals can for instance be obtained in bulk semiconductor compounds with cubic zinc blende structures[24]. Concerning interfaces, a structure inversion asymmetry can appear in multilayers. There appears a gradient of electric potential along the direction perpendicular to the interfaces, corresponding to an electric field that creates a Rashba effect on the conduction electrons[25,26].

I. 2. 2. Phenomenology of the SHE and EHE

Spin Hall Effect and Extraordinary Hall Effect

An interesting consequence of the SOC appears in the bulk of nonmagnetic materials: the SHE (cf. *Fig. I. 3* at the left-bottom). An applied charge current produces a transverse PSC, that is, up-spin and down-spin electrons moving oppositely in the transverse direction. The SHE has been theoretically predicted by M. I. Dyakonov and V. I. Perel in 1971[27], with a focus on semiconductors [28,29,30,31].

The appearance of a PSC will induce spin accumulations of opposite polarizations at the opposite edges of the samples, even in a non-magnetic material where the spin polarization is equal to zero.

There exists a reciprocal effect, the ISHE: when a pure spin current is injected in a non-magnetic sample, it is converted in a transverse charge current, orthogonal to both the spin direction and the electric current (cf. *Fig. I. 3* at the right-bottom). Note that no external magnetic field is required to observe the SHE or the ISHE.

The equivalent of the SHE in magnetic materials is the anomalous Hall effect (AHE) or extraordinary Hall effect (EHE)[32,33], which has been discovered earlier[34]. Since the magnetic materials are spin polarized, the imbalance of spin up and down electrons leads to a non-compensated charge accumulation at the edges of the sample, and thus to a transverse voltage that can be easily measured (*Fig. I. 3* at the top).

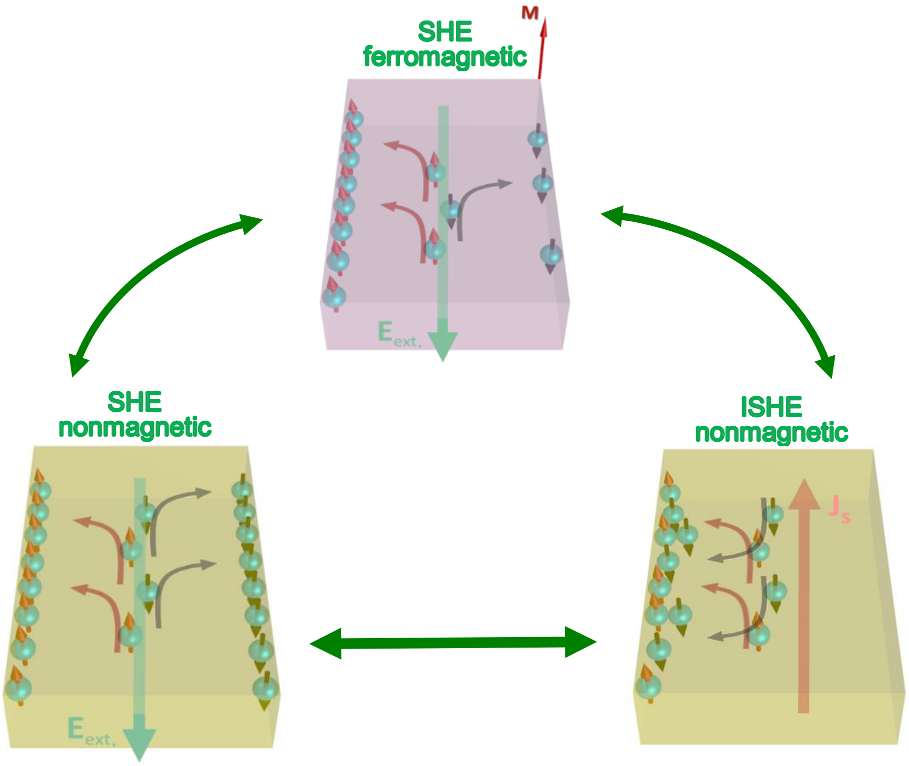

Fig. I. 3. *Illustration of spin-dependent effects (Replotted from ref. 84): anomalous (at the top), spin Hall (at the left-bottom), and inverse (at the right-bottom) spin Hall effects*

Spin-charge coupling in electrical diffusion equations

In order to give the phenomenological description of the charge-spin coupling, let us start by the drift-diffusion equation for charge currents given by Dyakonov *et al.* in *ref. 35*, under a charge current density $\boldsymbol{J_c}/e$:

$$\boldsymbol{J_c}/e = \mu n\boldsymbol{E} + D\boldsymbol{\nabla} n$$

(I. 22)

where μ, **E**, n, and D are the electron mobility (*i.e.*, the ratio of the particle's terminal drift velocity to an applied force), the electric field, the electron density, and the electron diffusion coefficient, respectively. μ and D satisfy the Einstein relation, *i. e., $D = \mu k_B T$*, where k_B and T are respectively Boltzmann's constant and the absolute temperature.

The drift-diffusion equation for the spin flow density $q_{s_{ij}}$, flowing in the i direction with a spin polarization in the j direction [27,35,36] is:

$$q_{S_{ij}} = -\mu n E_i P_j + D\frac{\partial P_j}{\partial x_i}$$

(I. 23)

Where P_j is the jth component of the polarization density vector **P,** related to the normal spin density as **S** = **P**/2.

In a collinear model, the spins are polarized along only one direction. Rather than using a tensor, it becomes possible to define a vector, the spin current density $\boldsymbol{J_S}$ (in A/m^2), so that $\boldsymbol{q_S} = \boldsymbol{J_S}/e$. This is the approach that will be used in this manuiscript.

It has to be noted that *eqs. (I. 22)* and *(I. 23)* are presented in absence of SOC. Let us now consider the inclusion of the spin-charge coupling with the SOC. In presence of SHE, the full drift diffusion equations can be written (see more detail in *refs. 35, 27* and *36*):

$$\boldsymbol{J_c}/e = \mu n\boldsymbol{E} + D\boldsymbol{\nabla} n + \Theta_{SHE}(\boldsymbol{E}\times\boldsymbol{P}) + \Theta_{SHE}D\nabla\times\boldsymbol{P}$$

(I. 24)

$$q_{S_{ij}} = -\mu n E_i P_j + D\frac{\partial P_j}{\partial x_i} - \Theta_{SHE}\varepsilon_{ijk}\left(\mu n E_k + D\frac{\partial n}{\partial x_k}\right)$$

(I. 25)

where ε_{ijk} is the unit anti-symmetric tensor, Θ_{SHE} is the spin Hall angle, *i.e.,* the conversion rate of between charge and spin currents.

The polarization density satisfies the continuity equation:

$$\frac{\partial P_j}{\partial t} + \frac{\partial q_{S_{ij}}}{\partial x_i} + \frac{P_j}{\tau_s} = 0$$

(I. 26)

where τ_s is the spin relaxation time.

The third term in *eq. (I. 24)* corresponds to the EHE in presence of a net spin polarization **P,** for instance in a ferromagnet. The fourth term in *eq. (I. 24)* corresponds to the production by ISHE of a contribution to the charge current $\boldsymbol{J_c}$ in response to a gradient of spin accumulation. The third term in *eq. (I. 25)* describes the SHE, where a P_j-polarized spin current in the i direction is produced by a perpendicular electrical field E_k.

The diffusion equation *(I. 25)* for the SHE induced by an applied current along the *y* direction, and in a collinear model with a spin polarization along the *x* direction, is:

$$\frac{J_{S_z}}{e} = -\Theta_{SHE}\varepsilon_x \mu n E_y \ \ or\, J_{S_z} = \ \Theta_{SHE}\varepsilon_x J_{c_y} \tag{I. 27}$$

where $E_y = -\nabla\mu$.

Hence we can write

$$J_{S_z} = \ \Theta_{SHE} J_{c_y} \times s_x$$

And in the general case,

$$\boldsymbol{J_S} \ \ = \Theta_{SHE} \boldsymbol{J_c} \ \ \times \boldsymbol{s} \tag{I. 28}$$

I. 2. 3. Microscopic mechanisms

As presented in the recent work of N. Nagaosa *et al.*[34] on the EHE in ferromagnetic materials, and in a synthesis by A. Hoffman on the SHE[37], the mechanisms of the spin-dependent Hall effects can be classified along two categories.

Extrinsic effects

A possible source of the SHE in bulk materials is the spin-dependent electron scattering on impurities, *i.e.*, the skew [38] and side jump scattering[39].

Skew-scattering events arise at an impurity location whose asymmetry can make a strong SOC. The impurity which forms a potential landscape acts differently on spin-up and spin-down electrons, so that the trajectories are bended in different directions see *Fig. I. 4(*a). The wave vector is not conserved during the scattering event.

The side-jump event also occurs at the impurity site, but the electron wave vector is conserved (cf. *Fig. I. 4b*).

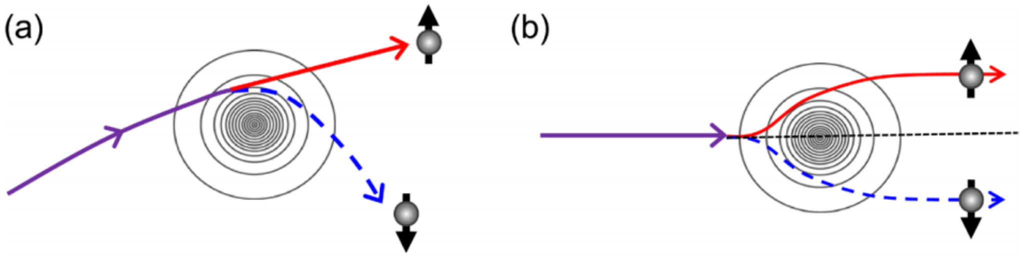

Fig. I. 4 *Illustrations of (a) skew scattering and (b) side jump near a potential center* [40]

The spin skew scattering also known as the Mott scattering[41], has been firstly proposed in 1958 by J. Smit[38] to give account of the existence of the EHE. This concept is based on the idea that at the vicinity of the impurity, due to the strong SOC there exists a gradient of the effective magnetic field in the scattering plane. The spin Hall resistivity is proportional to the longitudinal resistivity, which means that the strength of the SHE given by the ratio of them, the spin Hall angle, can be directly related to a quantity independent of the SOC impurity concentration[42].

In the side jump mechanism, the spin Hall resistivity is proportional to the square of the impurity resistivity, when the impurities are the only source of resistivity ($\rho_{SH} \alpha \rho_{imp}^{2}$)[43]. In most cases, the resistivity (ρ_{tot}) includes the impurity resistivity and an additional contribution from scattering potentials with weak SOCs.

The impurity spin Hall angle is influenced by the two mechanisms and can be written as: $\Theta_{SHE} \equiv \rho_{SH}/\rho_{imp} = a + b\rho_{tot}$[44], where a and b are the coefficients corresponding to the skew scattering and to the side jump.

Intrinsic effects

The intrinsic SHE corresponds to the mechanism where the spin dependent transverse velocities is due to the effect of the SOC acting on the electronic band structure, in absence of any impurity, or periodic but asymmetric potentials. Unlike extrinsic SHE, where the spin current is generated during the scattering events, the intrinsic SHE produces the spin current in between the scattering events. The contribution of the intrinsic SHE is related to the electric field due to the nonzero of the Berry's phase curvature[45,46]. The spin Hall conductivity is directly proportional to the spin-orbit polarization at the Fermi level, $\langle \boldsymbol{l} \cdot \boldsymbol{s} \rangle_{SF}$[46]. According to Hund's rules, the transition metals with more than half-filled *d*–bands possesses a positive spin Hall conductivity; the one with less than half-filled *d*–bands expected a negative spin Hall conductivity. *Fig. I. 5* reprints the results of the calculation of the intrinsic spin Hall conductivity in *4d* and *5d* metals based on a tight binding model [45,46].

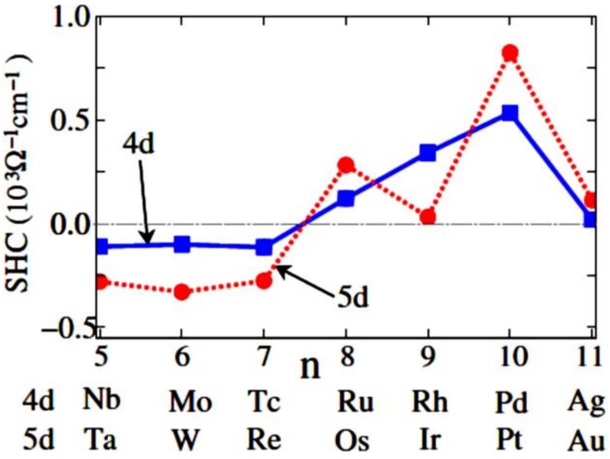

Fig. I. 5*. Intrinsic spin Hall conductivity calculated for different 4d and 5d transition metals reprint of* ref. *46*

I. 3. Spin orbit torque, SHE and Rashba effect

The interest towards SOC-based effects such as the spin Hall and Rashba effects has been largely increased by the discovery of the spin orbit torques (SOTs). These torques are based on the ability of SOC materials to generate spin currents, which carry a magnetic momentum that can be transferred to an adjacent magnetic layer [47].

Before discussing the main features of the SOTs, let us remind a few elements of the physics associated to the spin transfer torque.

Spin transfer torques

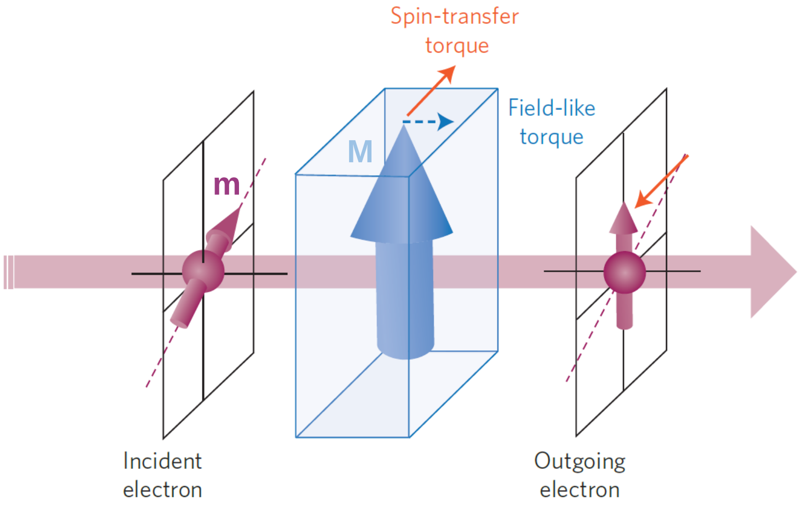

Fig. I. 6. *Illustration of the spin torque (replotted from A. Brataas et al. in ref.* [48]*): The polarization of the electron flow induces a transfer of angular momentum to the magnetization. The conservation of the angular momentum leads to the appearance of a torque acting on the magnetization.* ***M*** *and* ***m*** *are the magnetizations corresponding to local and itinerant electrons, respectively.*

The torque due to the spin current is the sum of two components, the in-plane torque (so-called Slonczewski torque or anti-damping torque or spin transfer torque) and the out-of-plane torque (so-called field-like torque, cf. *Fig. I. 6)* [54,49,47]:

$$\boldsymbol{\tau} \sim \ \boldsymbol{M}\times \delta\boldsymbol{m} = \boldsymbol{\tau}_{\boldsymbol{AD}} + \boldsymbol{\tau}_{\boldsymbol{FL}} = a_j\boldsymbol{M}\times(\boldsymbol{M}\times\boldsymbol{m}) + b_j\boldsymbol{M}\times\boldsymbol{m} \qquad (I.\ 29)$$

where $\delta\boldsymbol{m}$ is the additional magnetization given by the spin accumulation. AD and FL correspond to anti-damping and field-like, and the a_j and b_j parameters depend on the current, on the magnetization, and on the geometry and material properties. The magnetization dynamics is thus given by the Landau–Lifshitz–Gilbert–Slonczewski expression:

$$\frac{\partial \boldsymbol{M}}{\partial t} = \gamma \boldsymbol{M} \times \boldsymbol{H_{eff}} + \alpha \boldsymbol{M} \times \frac{\partial \boldsymbol{M}}{\partial t} + a_j \boldsymbol{M} \times (\boldsymbol{M} \times \boldsymbol{m}) + b_j \boldsymbol{M} \times \boldsymbol{m}$$

(I. 30)

where γ is the gyromagnetic ratio $\left(\gamma = {}^{g\mu_B}/_{\hbar}\right)$, **H_{eff}** is the effective magnetic field, which controls the magnetization precession described by the first term of the equation, α is the Gilbert damping constant. The four terms of this equation (the precession, damping, antidamping and field-like terms) are represented in Fig. I. 7.

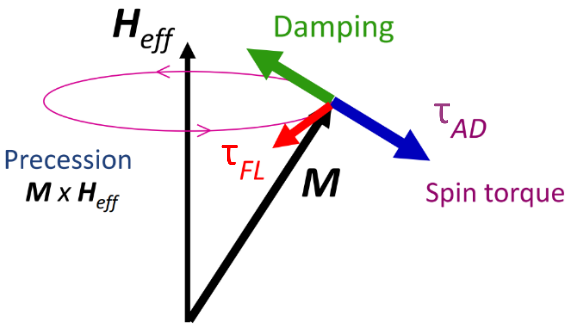

Fig. I. 7 *Illustration of the magnetization dynamics according to the Landau–Lifshitz–Gilbert–Slonczewski equation.*

In GMR and TMR stacks, the STT has been shown to be able to induce the precession of the magnetization and to induce the switching of the magnetization. This allowed the development of the STT-MRAM[50, 51, 52, 53, 54, 55]

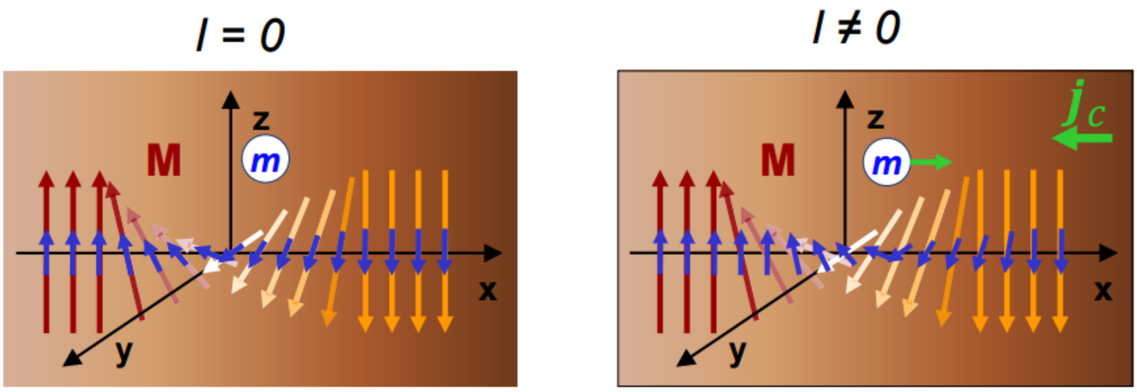

Fig. I. 8. *Spin torques on a magnetic domain wall.*

The STT can also act on textured magnetizations such as a magnetic domain walls. In *Fig. I. 8* a polarized current is applied to create a spin accumulation in the area of a Bloch DW. This spin accumulation creates a torque possessing here again two components, known as the adiabatic torque and the non-adiabatic torque[56], and that can lead to DW motion[57,58,59], DW depinning[60] or DW oscillations[61, 47, 61] The ability to induce the motion of DWs using currents allows developing memory applications, such as the racetrack memory[164] or the DW motion MRAM[62, 63, 64].

Spin-orbit torques

The discovery of spin-orbit torques[65] has allowed to extend our ability to control the magnetization using currents. Indeed, the efficiency of the classical spin-transfer torque is limited to the equivalent of one unit of ħ angular momentum transferred per unit charge in the applied current.

Fig. I. 9 describes a typical SOT experiment for DW motion, switching or second harmonic generation[66]. When an in-plane current is injected into a *N/FM/Oxyde* trilayer, a torque acts on the magnetization, possessing two components (field-like and antidamping). The origin of these torques are the SHE that is produced in the SOC material, and the Rashba effect at the interface. Both indeed convert the charge current into a spin current which can act on the magnetization (cf. *Fig. I. 9*). The switching of a perpendicularly magnetized element by spin-orbit torques has been demonstrated in the absence of any external magnetic fields[67]. The DMI[68,69,70] has been found to be a key element, and the study of spin-orbit torques is now extending towards new systems such as antiferromagnets[71], dichalcogenides[72,73] or topological insulators[74].

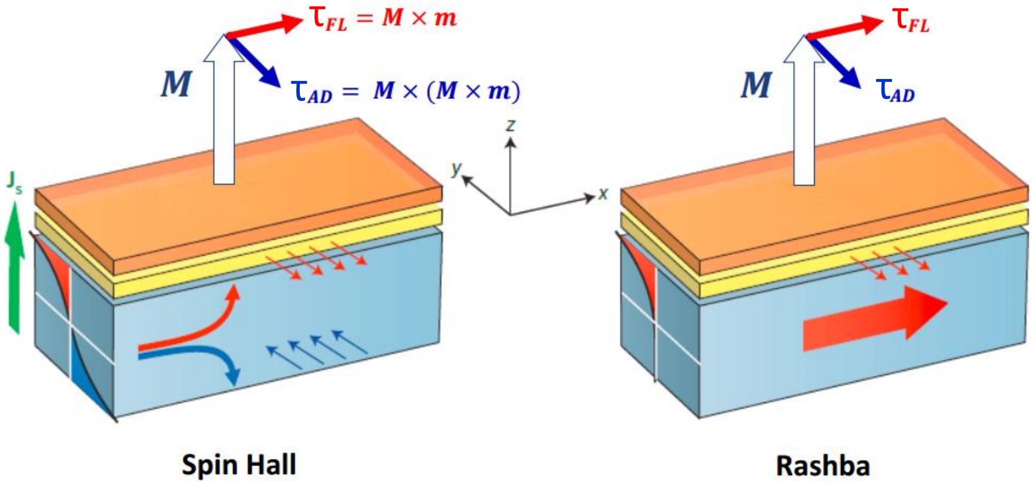

Fig. I. 9. *Scheme of a typical SOT experiment: an in-plane charge current is applied in a SOC-material/FM/Oxyde tri-layer.*

Whatever, the symmetry, magnitude and origin of spin–orbit torques remains a matter of debate, even in simple systems. This complexity pleads for measuring separately the charge/spin conversion by SOC, and the torque created by the spin current. Although this thesis does not deal with spin orbit torques, it shall be considered as a little step in that direction: indeed, one of its main objective is to propose a new technique, which allows quantifying the charge/spin conversion due to the SHE.

Let us discuss now of the state-of-the-art concerning the measurement of this conversion.

I. 4. Measurement techniques of the SHE

Lots of efforts have been recently made to develop techniques allowing to study the spin-charge interconversion, by SHE in the bulk of metals[75,76,77], semiconductors[78,79] or in superconductors[80], by Rashba effect in 2D electron gas [81,82], or at the surface of topological insulators[83]. In this part, we will give a glance at the measurement techniques used to characterize the SHE[84].

I. 4. 1. Optical techniques

Optical methods such as the magneto-optical Kerr effects[85] allow measuring magnetization in ferromagnets, through the rotation of the light polarization due to the Kerr effect. They can also be used to measure the current-induced spin accumulation at the edges of a non-magnetic SHE stripe, providing that the spin diffusion length is bigger than the optical wavelength. This method has thus for now been restricted to semiconductors. The first experimental optical observation of intrinsic SHE has been realized in GaAs-based samples at 30K[79]. Wunderlich *et al.*[86] has studied the extrinsic mechanisms of the SHE in semiconductors, using AlGaAs/GaAs spin-LED. Using the spin drift model (shown in *ref. 87* by *F. Zhang* in 2000), they reported a spin Hall angle of 10^{-4} and a spin diffusion length of 1-10 µm.

A polarized light can also be used to generate a spin accumulation, and consequently a spin current which can be then after transformed into an electric voltage by ISHE[88]. Both optical generation and detection of SHE have been shown in a recent work by H. Zhao *et al.*[89]. These optical tools have developed rapidly, to become a conventional technique for the characterization of SOC-based effects (including the Rashba effect) in semiconductors[123,124].

I. 4. 2. Techniques based on magnetization dynamics

The precession of the magnetization in a ferromagnetic layer can lead to the injection of a PSC in a neighboring SHE layer. This idea is at the basis of the spin pumping ferromagnetic resonance (SP-FMR) experiments[90,91]: the resonance induces a spin accumulation at the interface of a SHE material/ferromagnetic bilayer. The corresponding PSC is transformed by ISHE into a DC current or a voltage that can be measured as shown in *Fig. I. 10a*.

Reciprocally, when a charge current is applied in the plane of the SHE layer, a spin current generated by the direct SHE flows through the interface to the ferromagnetic layer, the corresponding angular momentum transfer altering the magnetization precession. This technique, known as Spin Transfer FMR or ST-FMR (*Fig. I. 10b)*, has been first studied by Ando *et al.*[92] and refined by Liu *et al.*[93].

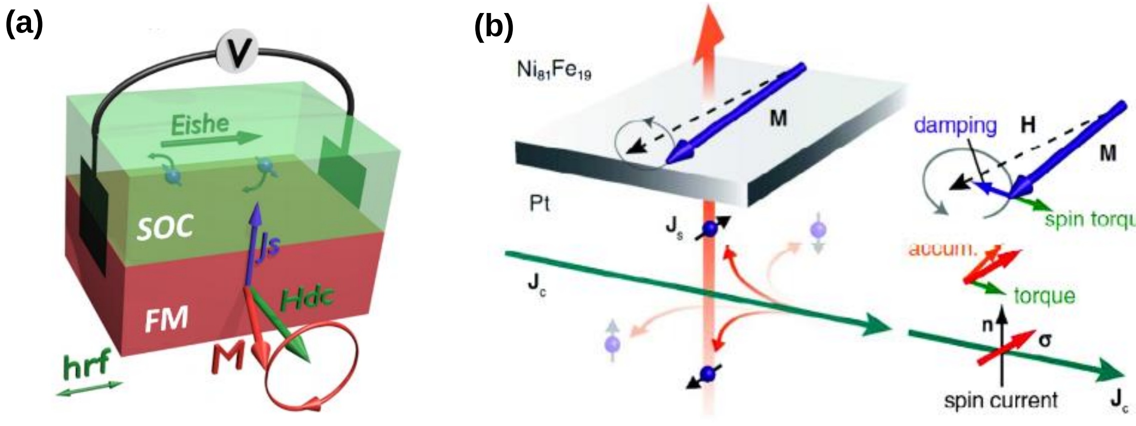

Fig. I. 10: *(a)* ***Principle of the SP-FMR (from ref. from ref. 135):*** *a spin current is injected from the ferromagnetic (FM) layer into the SOC layer, and converted into a transverse charge current by ISHE. This charge current is probed by measuring the voltage (V). (b)* ***Principle of the ST-FMR (from ref. 92):*** *a DC current* $\mathbf{J_c}$ *is applied in the SOC material (Pt), producing a spin current* $\mathbf{J_s}$ *by direct SHE. This spin current transfers a DC torque to the magnetization* ***M,*** *resulting in the alteration of the FMR spectrum.* $\boldsymbol{\sigma}$ *denotes the spin-polarization vector of the spin current.*

Since SP-FMR and ST-FMR experiments do not require nanofabrication and can be used for almost all materials, these techniques have become a basic tool for the SHE characterization. Large SHAs have been observed in heavy metals such as Pt (by SP-FMR [91, 94, 95, 96, 97, 98, 99, 100, 101, 102, 151, 130, 103, 134]; by ST-FMR [92, 93, 104,146, 158]), β-Ta[105, 151], β-W[150], Pd[94, 106, 107,] in AuW-alloys [108, 114], and even in p-type silicon film[109] with a very small intrinsic spin Hall angle of 0.01%.

The most important difficulty linked to these techniques is that the data can be polluted by parasitic effects, coming from the ferromagnetic layer such as AMR, and –as in all methods based on a bilayer-, by the difficulty to take into account the influence of the FM/NM interface[134,146].

I. 4. 3. Magneto-transport techniques

A- Techniques based on lateral spin-valves

Nonlocal measurements

Johnson and Silsbee demonstrated in 1985[110] the injection and non-local detection of a spin accumulation using a lateral spin-valve, which is a device consisting in a non-ferromagnetic bridge (NM) connecting two ferromagnetic electrodes (F). *Fig. I. 11* shows the set-up used for the nonlocal detection of the spin accumulation in a lateral spin valve. This technique has evolved to become a conventional way to characterize the spin dependent transport properties of materials such as conductor metals and semiconductors.

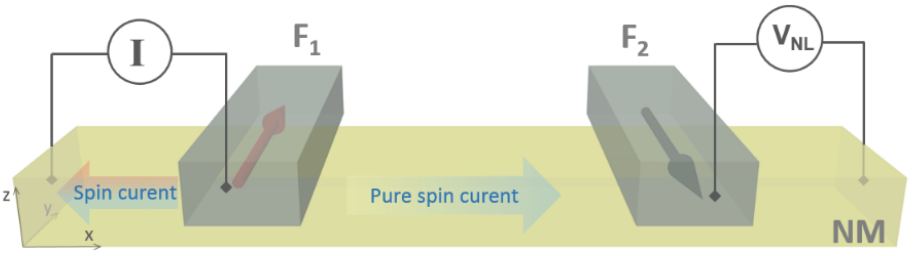

***Fig. I. 11**: **Nonlocal measurement in a lateral spin valve**: the charge current flows through the F_1/NM interface (along the –x direction), creating a spin accumulation at the vicinity of this interface. A PSC is injected into the NM wire along the +x direction. The ferromagnetic electrode F_2 plays the role of a spin detector. The electrochemical potentials in F_2 probes the spin accumulation produced by F_1 at the F_2/NM interface. When the magnetization states between F_1 and F_2 are parallel (↑↑ or ↓↓), F_2 probes the electrochemical potential of majority spins so that the voltage is positive. When the magnetizations of F_1 and F_2 are antiparallel (↑↓ or ↓↑), F_2 probes the electrochemical potential of the minority spins, so a negative voltage appears, due to the deficit of minority spins.*

Nonlocal spin transport in materials with long spin diffusion lengths

A LSV can be used to inject a PSC in the NM material, which can in turn be exploited to study the SHE in an adjacent SOC-nanowire. Valenzuela and Tinkham (2006, 2007)[76, 111] thus adapted a LSV to perform the non-local electrical detection of the ISHE in Al, using the experimental set-up shown in *Fig. I. 12(a)*. However, since the spin current needs to reach the Hall cross , this technique requires materials with long spin diffusion lengths , and is thus restricted to materials with low SO coupling. It has been for instance applied to GaAs using a Fe-spin-injector by K. Olejník *et al*.[112].

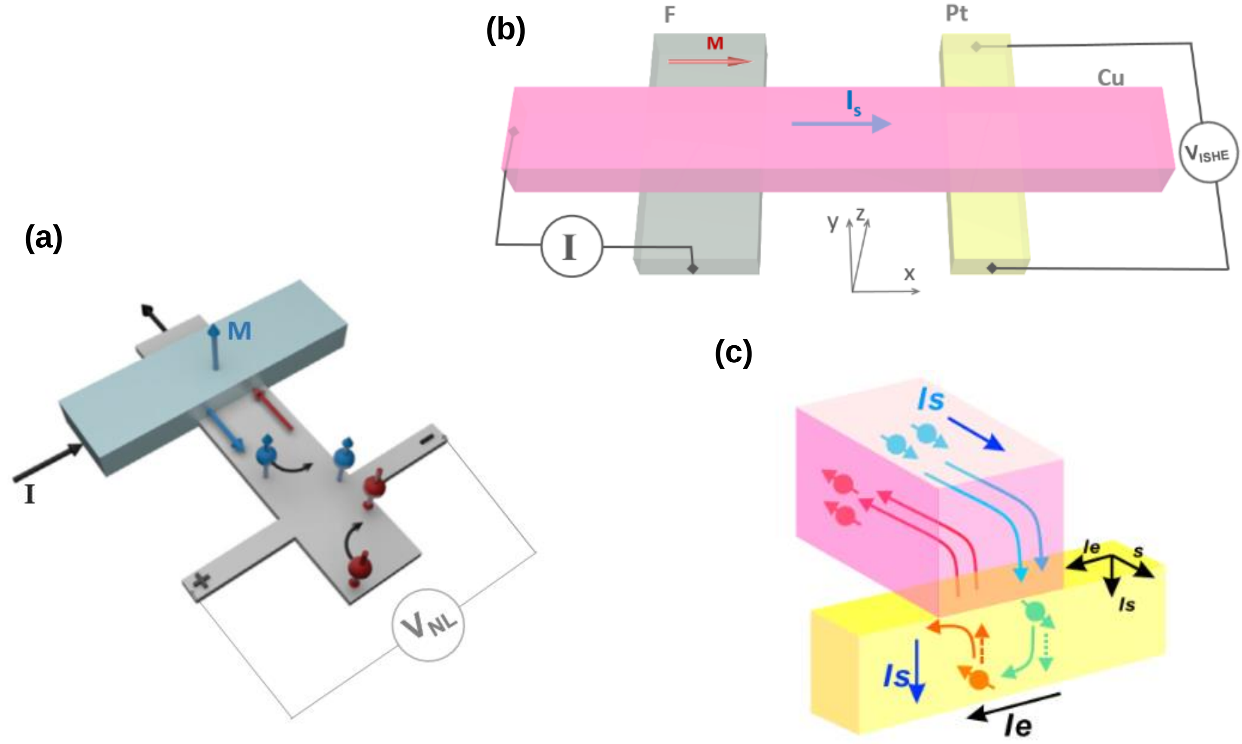

Fig. I. 12: *(a) Pure-spin-current-induced Hall effect in ref. 111: the spin current with perpendicular-polarized spins is converted into a transverse voltage by ISHE. (b) and (c) Nonlocal detection of the HE with vertical spins (adapted from ref. 130): the graph (b) depicts the measurement setup. The applied field orients the magnetization* ***M*** *in the x direction. The spin current is injected towards the Pt channel through the Cu-bridge. The spin current is absorbed in the z direction of the Pt, as shown in (c) creating a charge current by ISHE along the Pt wire (b).*

Nonlocal spin transport with planar magnetization

The limitation of nonlocal transport for materials with short spin-diffusion lengths, which are usually the materials of interest in terms of spin Hall angles, has been overcome by Kimura *et al.*[130] in 2007. The detection electrode of the LSV shown in *Fig. I. 12(b)* is replaced by a platinum nanowire (cf. *Fig. I. 11)*. The external field is applied in-plane along the x direction to induce the injections of spins with a polarization along x. The PSC flows along the Cu-channel and is absorbed at the Cu/Pt interface in the z direction, and then converted into a charge current in the y direction. The conversion rate is large in comparison with previous reports on Al and semiconductor (the spin Hall angle of Pt in this NiFe-Cu-Pt system was deduced of 0.37%). Shortly thereafter, the study of L. Vila *et al*.[113] showed that the spin Hall conductivity is nearly constant as a function of temperature, and evolves in a quadratic form with the charge conductivity, which means that the SHE in Pt is dominated by the side jump or intrinsic mechanisms. The method has also been applied to characterize other SOC-metals[132] such as Nb, Ta, Mo, Pd, and Pt, with obtained spin Hall angles of -0.87, -0.37, -0.80, 1.2, and 2.1%, respectively.

With the advantage of being able to measure the SHA in both systems with long or short SDL, the LSV-based method has been applied to detect SHE in many materials, such as in the heavy-metal-impurity-alloys of AuW[108,114], CuBi[129], and CuIr[115], in 5d iridium oxide[116], in ferromagnetic alloys of NiPd[117] and in the heavy-metal-based superconductor of NbN[80]. Additionally, and similarly to the spin pumping method, the LSV-based method can also be applied to detect the inverse Rashba-Edelstein effect in 2D electron gas, for instance at the Cu/Bi interface [128]. Nonetheless, finite element method are often required to take into account the shunt by the Cu wire at the vicinity of the SHE material especially when this last one has a much larger resistivity than Cu.

B- Spin Hall magnetoresistance

A new magnetoresistance, the spin Hall magnetoresistance (SMR), appears in FM-NM bilayers, and allows measuring SHA[118, 119, 120]. *Fig. I. 13* illustrates a simplified ballistic picture of the spin currents reflected at the YIG/Pt interfaces, which is the origin of the SMR. The SMR is a promising technique for the SHE detection in metals. In Pt/YIG , H. Nakayama *et al.* [118] report a spin Hall angle of 4 % and a spin diffusion length of 2.4 nm; whereas N. Vlietstra *et al.*[120] reported the values of 8% and 1.4 nmm respectively. One can note that despite the apparent discrepancy, they found a similar $\Theta_{SHE}\lambda_S$ product.

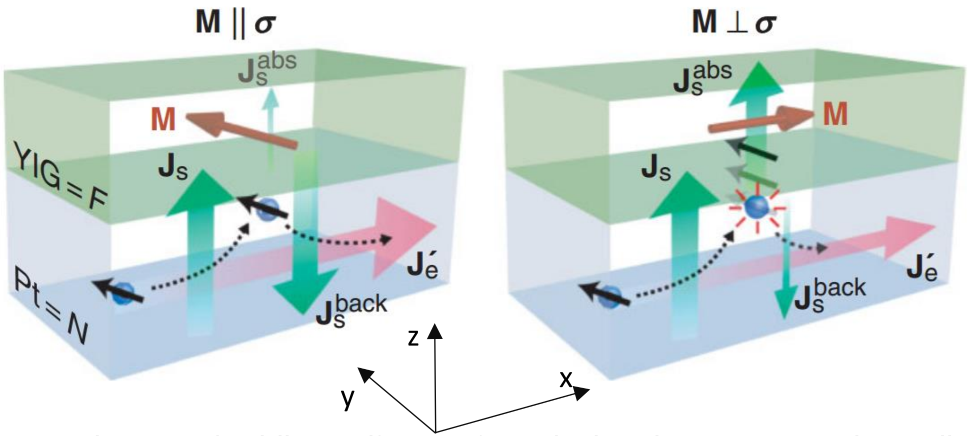

Fig. I. 13*: SMR in a YIG/Pt bilayer (from ref. 118): the charge current is applied along the x direction in the Pt, generating a spin current of y-polarization in the z direction ($\boldsymbol{J_s}$). The resistance of the stack is measured along the x direction, as a function of the orientation of the magnetization in the YIG, which is controlled by an external magnetic field. When the YIG magnetization aligns with the polarization of the SHE spin accumulation, the reflected spin current ($\boldsymbol{J_S^{back}}$) in the –z direction is maximal, consequently producing an additional negative charge current by ISHE, and thus increasing the apparent resistivity. This charge current is minimal when the magnetization is perpendicular to the polarization of the initial SHE spin current.*

C- Other electrical detection techniques

Hankiewicz et al. (2004)[126] considered the concept of Hirsch in 1999[75] but on a planar structure shaped as an H, simpler to fabricate. Brüne et al. (2010)[125] realized the planar H-shape structure to observed the SHE in HgTe. The principle of the device is shown in *Fig. I. 14a*. The device can measure the SHE without any applied field, nor ferromagnetic injection/detection. However, it is only applicable to materials with long spin diffusion lengths and to high spin Hall angles: since it needs two conversions, firstly by SHE and secondly by ISHE, the conversion rate is proportional the square of the spin Hall angle.

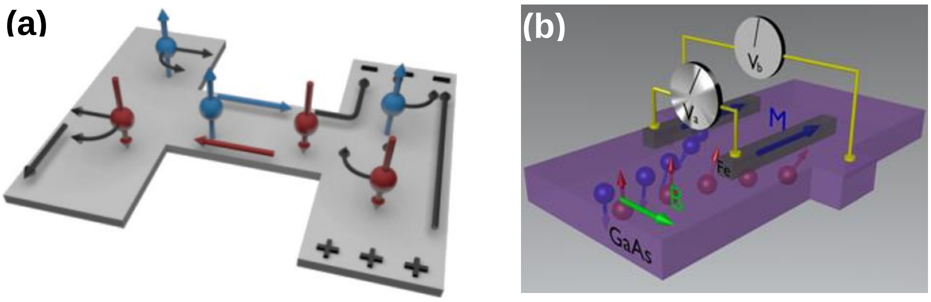

Fig. I. 14*: (a)* ***Principle of the H -based device (from ref. 84)****: A charge current is applied in the left hand wire (the black arrow), creating a spin current in the bridge. This spin current is then converted into a charge current by ISHE which can be measured by a voltmeter along the right hand wire (black arrow). (b)* ***Principle of the SHE detection device proposed by Garlid et al. in ref. 127****: Two thin Fe electrodes are laid along the (In)GaAs Hall cross. Firstly, the magnetizations in the Fe-electrodes is initialized in the anti-parallel or in the parallel states. The charge current is applied along the semiconductor wire to create the spin accumulations of the perpendicular-polarization by SHE in (In)GaAs. An in-plane field B is applied perpendicularly to the Fe-electrodes to induce the precession of the spin accumulation. The spin signal is the measured voltage* $V_a - V_b$*.* V_b *is used as a reference, to eliminate parasitic effects such as the normal Hall contribution due to the stray-field.*

A simple device, shown in *Fig. I. 14b*, has been originally proposed by F. Zhang[87] in 2000, and realized by Garlid et al. in 2010[127] to measure the direct SHE in GaAs and InGaAs semiconductors. This experiment showed that both the skew and side-jump scattering contribute to the spin Hall conductivity in these semiconductors. This technique was further developed by M. Ehlert *et al.*[121] in Fe/(Ga,Mn)As/GaAs samples. Finally, one shall mention the transport experiment proposed by L. Liu *et al*.[122] to realize the SHE tunneling spectroscopy in a CoFeB/(MgO,Al_2O_3)/Ta system.

For the strong SOC materials, possessing short spin diffusion lengths, the possible techniques of the detection remains limited. The spin Hall angles and spin diffusion lengths have been reported with very large uncertainty ranges, and strongly depend on the techniques of characterization. For example, the reported value of the spin Hall angle and spin diffusion length in Pt, which is the archetype SHE material, are in range of 0.3% to 36% and 0.5 to 12nm, respectively (see in Chapter II *Fig. II. 9* and *Table 1*).

This state of the art thus shows that the measurement of the SHA remains a major metrology problem in spintronics, especially concerning the techniques applicable to heavy metals, which possess large conversion rates but short spin diffusion lengths.

In this context, the next chapter will propose a new electrical technique to measure the SHE and the spin diffusion length in materials with high spin-orbit coupling.

CHAPTER II: NANOSTRUCTURES FOR THE DETECTION OF THE SHE IN PLATINUM

As seen in *Chapter I*, there exist several ways to detect the charge-to-spin conversion induced by SO effects, the most used being probably the optical methods[79,123,124], second harmonic and ferromagnetic resonance techniques[90, 91, 92, 93]. Large efforts have also been devoted to develop purely electrical ways of detecting the conversion, primarily for the sake of simplicity and versatility, but also because the long-term objective is to implement SO effects into spintronic nanodevices. Direct ways to probe the conversion electrically are the H-shaped double Hall cross[125,126] or the method proposed by Garlid *et al*.[127] (See more in *Section I. 4. 3. C-*), but they remain limited to materials with long spin-diffusion lengths (*e.g.*, semiconductors), which are generally associated to low conversion rates. The insertion of SO materials in lateral spin-valves also allows observing the conversion in systems with large SO coupling, such as SHE heavy metals or Rashba interfaces[82,128]. However, the nanodevice remains complex: a nonmagnetic channel is required to transfer the spins from the source to the detector[129,130,131,132], which multiplies interfaces and thus render delicate the quantitative extraction of the conversion rate.

In this chapter, we demonstrate a simple way to probe electrically the direct and inverse conversion in SHE systems, using a system akin to the ferromagnetic/nonmagnetic bilayers used in most spin-orbit torque experiments[105].

II. 1. Principle

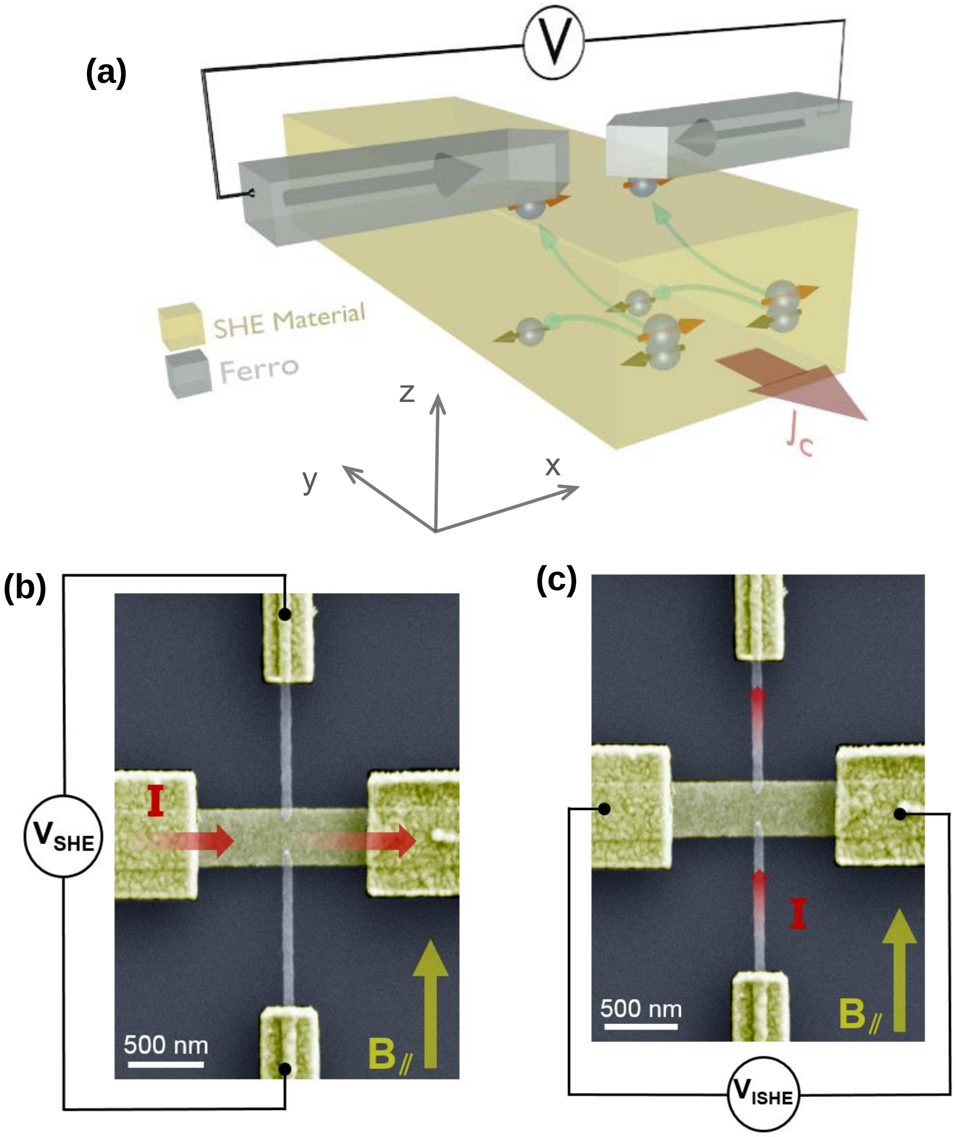

Fig. II. 1. *Measurement principle: (a) Scheme of the conversion device. Two ferromagnetic electrodes are connected on top of a SHE nanowire. The magnetization within the ferromagnetic electrodes, represented by black arrows, is along the x direction. A charge current J_C flows along SHE wire (in the Y direction), and generates a spin current J_S along the Z direction, as down-spin and up-spin electrons are deflected along the positive and negative Z direction, respectively. Consequently, a spin accumulation appears at the edges of the SHE wire, which can be probed by the* *ferromagnetic electrodes. (b) and (c) SEM images of the device, with schemes of the measurement setup for the SHE (b) and ISHE (c) detections.*

The spin-charge conversion device proposed here is illustrated in *Fig. II. 1a*, and consists simply of a SHE wire connected to two transverse ferromagnetic electrodes. The device is designed so that the easy axis of magnetization is parallel to the ferromagnetic electrodes. Two electrical measurement schemes can be used. The first one, shown in *Fig. II. 1a* and *1b*, corresponds to the measurement of the direct SHE. The charge current flowing in the SHE wire generates a spin accumulation at the top surface of the SHE material, which is probed using the ferromagnetic electrodes.

The second measurement scheme, shown in *Fig. II. 1c*, corresponds to the ISHE. The flow of a charge current along the ferromagnetic electrodes induces the injection of a spin current within the SHE wire. This spin current is then converted by ISHE in a charge current along the SHE wire, so that in the open circuit conditions used here this generates a voltage between the two ends of the SHE wire.

II. 2. Experimental spin signals

An example of spin signal obtained in the SHE configuration is given in *Fig. II. 2a,* using a device with a Pt wire and $Co_{60}Fe_{40}$ electrodes. The ratio R_{SHE} between the measured voltage and the constant applied current is measured as a function of the magnetic field applied along the X axis, which corresponds to the easy axis of the ferromagnets, and thus to the quantification axis. The CoFe electrodes are designed so that they possess different switching fields. The variations of the resistance in the loop are due to the magnetization switching of the electrodes. This can be understood as follows: at any point of the SHE material, the relationship between the local charge current and local PSC is as shown in eq. (I. 28),

$$\boldsymbol{J_S} = \theta_{SHE}\, \boldsymbol{J_C} \times \boldsymbol{s} \tag{II. 1}$$

where $\mathbf{J_C}$, $\mathbf{J_S}$ and **s** denote the charge and spin current density vectors, and the spin-polarization vector of the spin current, respectively. This leads to a spin accumulation at the surface, with majority spins along the *X* direction as illustrated in *Fig. II. 1a*. If the magnetization of a ferromagnetic electrode is along +*X* (or –*X*), the Fermi level of the electrode aligns with the electrochemical potential of the majority spins (or minority spins, respectively). When the magnetizations of the electrodes are parallel, there is no voltage difference between the electrodes, which are probing the same electrochemical potential. However, when they are antiparallel a voltage difference appears, corresponding to the difference between the spin up and spin down electrochemical potentials. This voltage is positive for positive fields, where the electrodes are in the head-to-head magnetic configuration. For negative fields, the antiparallel state is the tail-to-tail configuration, the electrodes now probe the opposite spins, and thus the measured difference of electrochemical potentials becomes negative. Note that in this CoFe/Pt device, the amplitude of the spin signal is 8.0 ± 0.5mΩ. This has to be compared to typical SHE signals measured in lateral spin valves, which are of the order of 0.1 mΩ or lower (*i.e.*, two order of magnitude smaller [130,132,131]) because of the spin relaxation in the channel and at the interfaces.

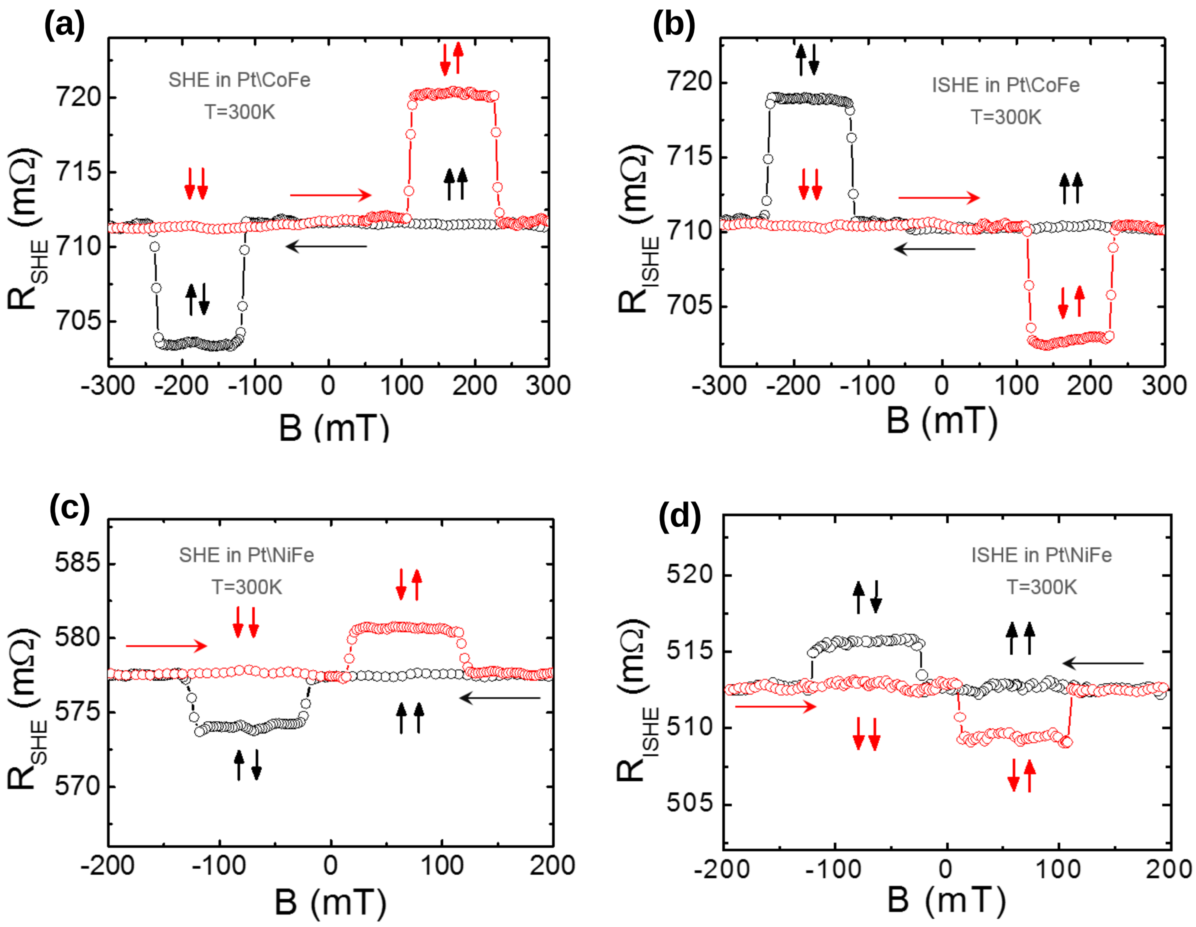

***Fig. II. 2.* Observation of SHE and ISHE:** *Examples of SHE and ISHE signals in a Pt-based device, probed using CoFe electrodes (a) and (b), and NiFe electrodes (c) and (d). The SHE and ISHE measurement configurations correspond to Fig. II. 1 (b) and Fig. II. 1(c), respectively. The Pt wire is 7 nm thick, and 400 nm wide (a) and (b) or 300 nm wide (c) and (d). The ferromagnetic electrodes are 15 nm thick and 50 nm wide. The electrodes are deposited on top of the SHE wire. The vertical arrows depict the magnetic state of the two ferromagnetic electrodes. The horizontal arrows indicate the field sweep direction.*

The spin signal obtained in the ISHE configuration is shown in *Fig. II. 2(b)*. Apart from the sign, which depends only on how the voltmeter is set up, it is similar to what is obtained in the SHE measurement, with exactly the same spin signal amplitude. The equivalence of the SHE and ISHE measurements, predicted by the Onsager reciprocal relations, has been verified in all our samples. The case of the ISHE configuration can be understood by considering that when the magnetizations of the electrodes are antiparallel, a spin current is injected in the SHE material. This spin current is then converted into a voltage by ISHE. For negative fields, and in the antiparallel configuration, the spin current is still injected, but its spin direction is reversed, which leads to a change of sign of the ISHE voltage. *Fig. II.* 2*c* and *Fig*. **II. 2***d* correspond to the SHE and ISHE signals when using $Ni_{81}Fe_{19}$ electrodes instead of CoFe. The observed behavior is identical, although with a lower spin signal amplitude that we attribute to the fact that the effective spin polarization of CoFe is higher[133].

II. 3. FEM simulations of the conversion

Lots of efforts have been recently devoted to develop an accurate measurement method of the spin transport parameters of SHE materials, *i.e.*, the spin diffusion length λ and the spin Hall angle Θ_{SHE}. To extract these parameters from our experiments, numerical finite elements method (FEM) simulations have been performed, using a 2-current drift diffusion model (see *Annexes B*), and taking into account the presence of the EHE in the ferromagnetic electrodes.

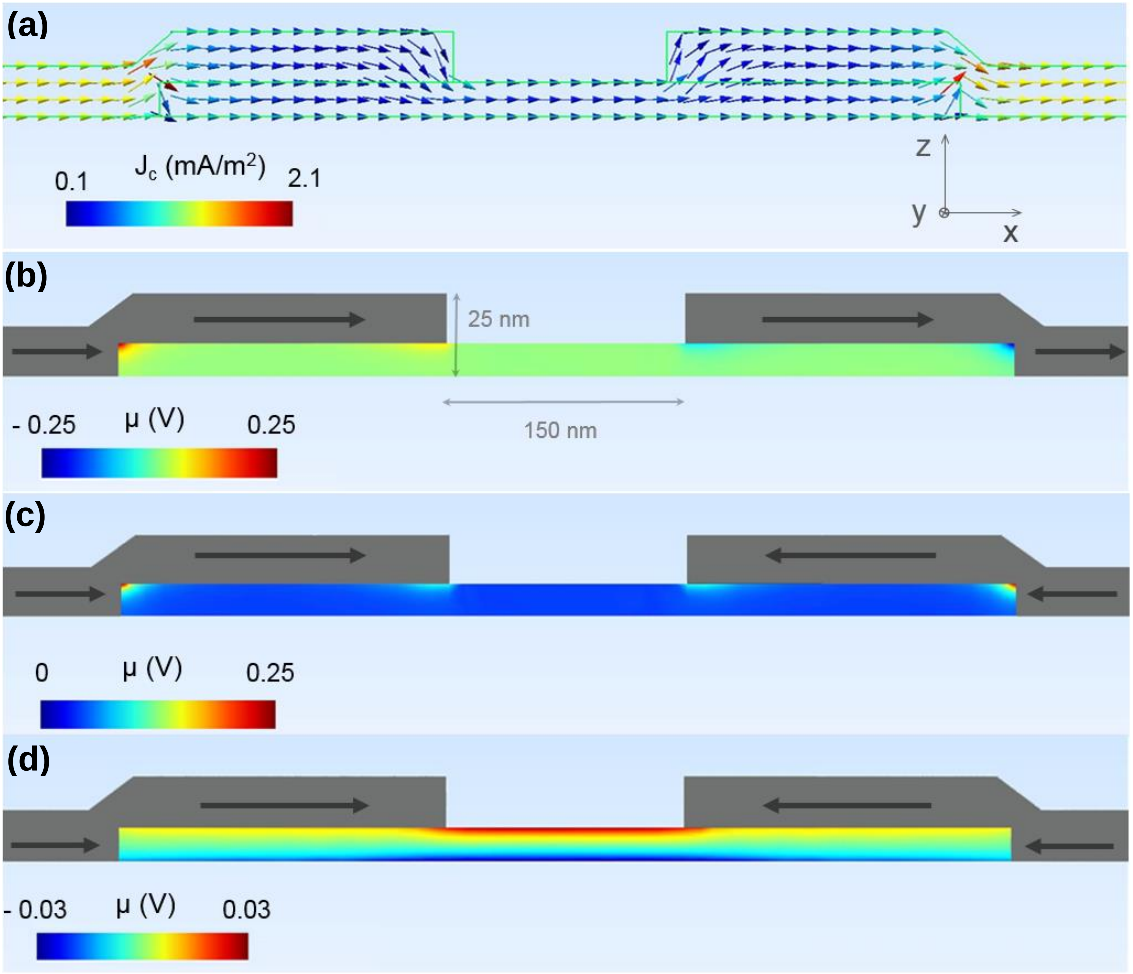

Fig. II. 3. Results of 3D FEM simulations: *For ISHE calculations (a, b and c), a 1A current is applied along the ferromagnetic electrodes. Fig. (a) is a cross section of the device along the XZ plane, showing the geometry of the current lines. The current flows from the ferromagnetic electrode to the SHE material, and then to the second electrode. Note that the current circumvents the lateral edges of the SHE wire, which are supposed to be insulating (previous transport experiments indeed showed that the interfaces that are not etched during our nanofabrication process remain insulating). (b) and (c) Cross-sections showing the spin accumulation (i.e., half the difference between electrochemical potentials). The spin current is proportional to the gradient of this spin accumulation. In our ISHE measurement setup we are measuring only the Z component of the spin current. In the parallel case (b), the spin accumulation pattern is antisymmetric, and the Z component of the spin current is in average equal to zero. In the antiparallel case (c), the spin accumulation pattern is symmetric, the Z component of the spin current is non-zero, which leads to the appearance of an ISHE* *signal. For the SHE measurement configuration (d), a 1A current is applied along the SHE wire. There is a large PSC along the Z direction due to the SHE. The spin accumulation at the top surface of the SHE material is probed by the ferromagnetic electrodes.*

Fig. II. 3 presents the main results of these simulations. *Fig. II. 3a* shows that in the ISHE configuration the current lines are deflected into the SHE material. The corresponding spin accumulation µ for the parallel and anti-parallel states are shown in *Fig. II. 3b* and *Fig***. II. 3***c*, respectively. In both cases, a gradient of the electrochemical potential appears where the current gets into or out of the SHE wire. This gradient, which corresponds to a spin current, possesses a component along the Z direction. As the magnetization is along *X*, the ISHE generates a charge current density along the *Y* direction that will be detected by the voltmeter. In the parallel magnetization state *Fig. II. 3b*, the spin accumulations are of opposite signs, so that the generated current densities cancel out. In the antiparallel state *Fig. II. 3c*, the spin accumulations are symmetric, the ISHE generated current densities add up, and as seen in the experiments a voltage difference appears between the ends of the SHE wire.

*Fig. II. 3*d shows the spin accumulation in the SHE configuration, when the charge current flows along the SHE wire. The ferromagnetic electrodes are in contact with the spin accumulation that takes place at the top surface of the SHE wire. In the antiparallel state of magnetization, a voltage difference appears between the two ferromagnetic electrodes, which probe different electrochemical potentials.

II. 4. Thickness dependence and spin diffusion length of Pt

In order to improve the physics involved, we derived an analytical expression, obtained in the framework of a 1D spin diffusion model. The amplitude of the spin signal varies according to equation (see more details in *Annex C*):

$$\Delta R_{SHE/ISHE} = \frac{\Delta V}{I} = \frac{2p_F \Theta_{SHE} \lambda_N}{\left(\frac{h_N}{\rho_N} + \frac{h_F}{\rho_F}\right) w_N - \frac{h_F}{\rho_F} g} \frac{\frac{1}{\rho_N \lambda_N}\left(1 - \frac{1}{cosh\left({}^{h_N}/_{\lambda_N}\right)}\right)}{\frac{1}{\rho_N \lambda_N} tanh\left({}^{h_N}/_{\lambda_N}\right) + \frac{1}{\rho_F^* \lambda_F} tanh\left({}^{h_F}/_{\lambda_F}\right)}$$

(II. 2)

where $w_{N/F}$, $h_{N/F}$, and g are the widths, the thicknesses of the nanowires and the gap between the electrodes, and p_F, λ and ρ are the spin polarization, spin diffusion length and resistivity, respectively. Subscripts F and N correspond to the ferromagnetic and non-ferromagnetic layers, respectively. Note that it is also possible to add to this 1D model the contribution of the EHE in the electrodes (see more details in *Section II. 4.*), even though comparison with 3D simulations show that the 1D model overestimate the EHE contribution for SHE materials with high resistivity.

In *eq. (II. 2)*, the spin signal amplitude is found to be linear in Θ_{SHE}. If the spin diffusion length λ_N is also unknown, it is possible to extract it by studying the dependence of the spin signal with the thickness of the SHE layer h_N. This study has been done for the Pt\CoFe system. *Fig. II. 4* shows the experimental dependence of the spin signal amplitude on the Pt thickness. According to *eq. (II. 2)*, a maximum of the spin signal amplitude appears for $h_N{\sim}2\lambda_N$, which leads to $\lambda_{Pt} = 3.0 \pm 0.6$ nm (note that as the spin diffusion length values of Pt are spread in the literature between 1.2 and 12.0 nm, it is difficult to claim good agreement with previously reported values [104, 130, 132,134, 135, 136]). Note however that the value of $\rho_{Pt}\lambda_{Pt} = 0.84 \pm 0.17$ fΩ.m^2 is close to what has been measured in several recent studies, for example the values of 0.77, 0.63, 0.61, and 0.80 fΩ.m^2 are shown in *refs. 104, 134, 135,* and *136,* respectively.

Fig. II. 4 also exhibits the expected variations of spin signal according to the 3D numerical simulations. Simulations were realized with varying Pt thicknesses. If we assume that $\lambda_{Pt} = 3.0$ nm, the calculated curves reproduce the experimentally observed behavior for a value of the spin Hall angle of Θ_{SHE} = 19%. For the 1D model, if we assume again that λ_{Pt} = 3.0 nm, the best Θ_{SHE} value to reproduce the experimentally observed behavior is around 13%.

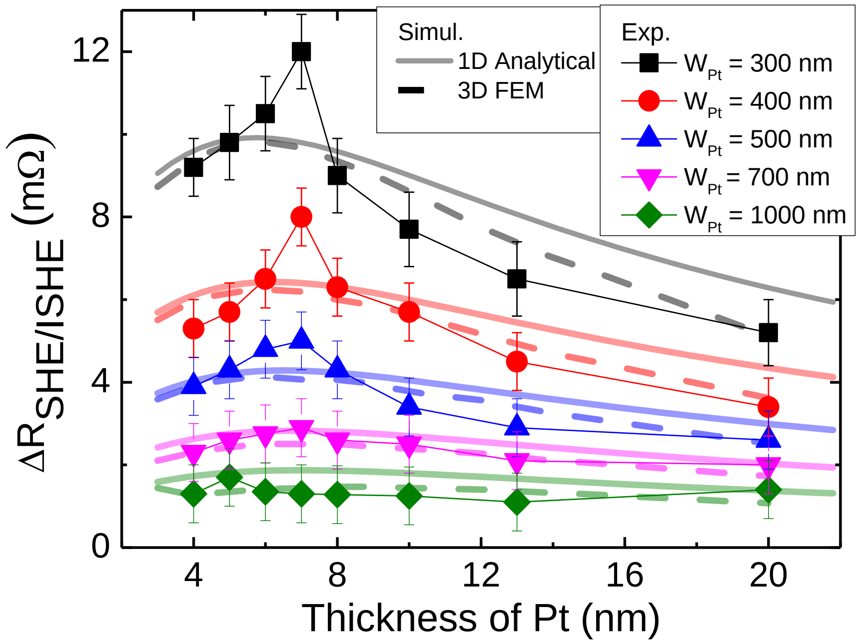

Fig. II. 4. *Spin signal amplitude vs. Pt thickness in devices with CoFe electrodes: experimental results (symbols), 3D FEM simulations (dashed lines, calculated with λ_{Pt} = 3.0 nm and Θ_{SHE} = 20%), and 1D analytical model (solid lines, calculated with λ_{Pt} = 3.0 nm and Θ_{SHE} = 13%). The dependence is plotted for various channel width. The maximum of the spin signal amplitude is theoretically expected for a Pt thickness equal to two times the spin diffusion length.*

As expected from *eq. (II. 2)*, at large thicknesses the amplitude of the spin signal decreases roughly as $1/w_{Pt}$. This can be understood by the fact that in the SHE experiments the signal is proportional to the current density, which decreases with w_{Pt}.

II. 5. Parasitic effects

The contribution of the EHE to the signal can be calculated, as well as the contribution from the thermal and normal Hall effects to the measured signals.

II. 5. 1. EHE contribution to the signal

AMR, planar Hall effect (PHE), and spincaloritronic effects have been considered as possible artifacts leading to the same kind of signal. They can be ruled out for symmetry reasons and/or because their amplitudes in this geometry are small. However, for systems with small spin Hall angles we found out that the contribution of EHE has to be taken into account to estimate properly the spin Hall angle. Indeed, the contribution of EHE to the signal has the same symmetry as that of the SHE. Its amplitude depends on the resistivities and on the device geometry as well *Fig. **II. 5**.*

A crude 1D model has been developed to calculate the EHE contribution to the signal. The more exact way to calculate the EHE contribution remains the use of 3D simulations. In the simulations, we took into account the EHE by measuring experimentally the Hall angle in Hall crosses, and by computing both the effect of the SHE and the EHE. These calculations showed that the ratio between the EHE and SHE contributions is of the order of 12% for Pt, 11% for Pd, 19% for W, 35% for Au, and can go up to -100% for Ta. The high ratio for Ta is due to the very high resistivity of Ta (200 µΩ.cm) in comparison with Pt (18-32 µΩ.cm depending on the thickness), which forces the current to flow in the ferromagnet and thus increases the EHE signal. *W* is also resistive, but its SHE angle is higher than the spin Hall angle in Ta, so that the ratio remains lower.

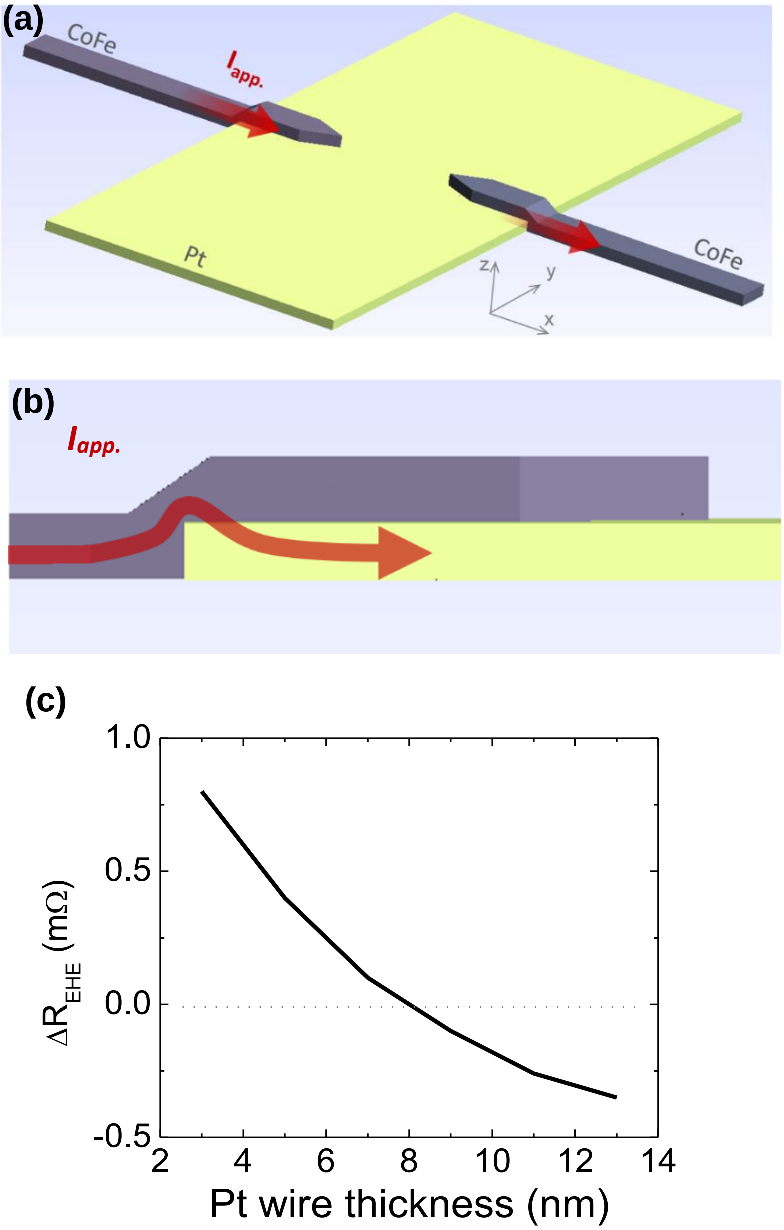

Fig. II. 5. ***Geometry effect on the EHE:*** *Design used in the FEM simulations of Section II. 3, with a spin Hall angle equal to zero, used to estimate the EHE contribution to the signal due to the CoFe. (b) Zoom on the current line in the contact area with the Pt wire: it climbs and drop down because of the shunting effect by Pt. Note that we assume that the current circumvent the lateral side of the Pt wire because this interface is not cleaned during the nanofabrication. (c) Simulated EHE contribution to the signal vs. Pt thickness, in the CoFe(15)/Pt(3-13) system. The EHE contribution depends on the thickness of Pt because it leads to a change of the current line distribution in the CoFe wire.*

II. 5. 2. Thermal effect

Concerning spincaloritronic effects, we checked the dependence of the spin signal amplitude with respect to the applied current. It is found to vary linearly *(Fig. II. 6*) up to large current densities.

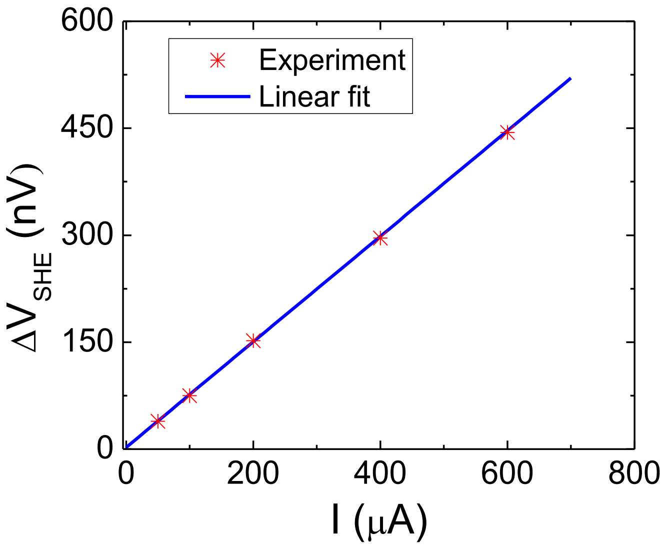

Fig. *II.* 6. *Amplitude of the spin signal vs. applied current, in a Py(20)/Pt(20) device with a 500 nm wide channel, and fit by a linear law. Most measurements are done using 100 or 200 µA so with current densities much smaller than 10^{11} A/m^2.*

Also, we performed tried to observe the contribution of spincaloritronic effects in the spin signals as shown in *Fig*. II. 7*.* There is no signal in the second harmonic measurement of the SHE, and it remains very small in the ISHE second harmonic measurement (in comparison to the ISHE signal of *Fig. II. 2b)*. The signal could be explained by the magnonic current produced by the heat gradient at the two interfaces, leading to the injection of a spin current through the Pt. Whatever, the linearity of the signal with the applied current and the absence of significant second harmonic signal seems to indicate that spincaloritronic effects do not play any role in our experiments.

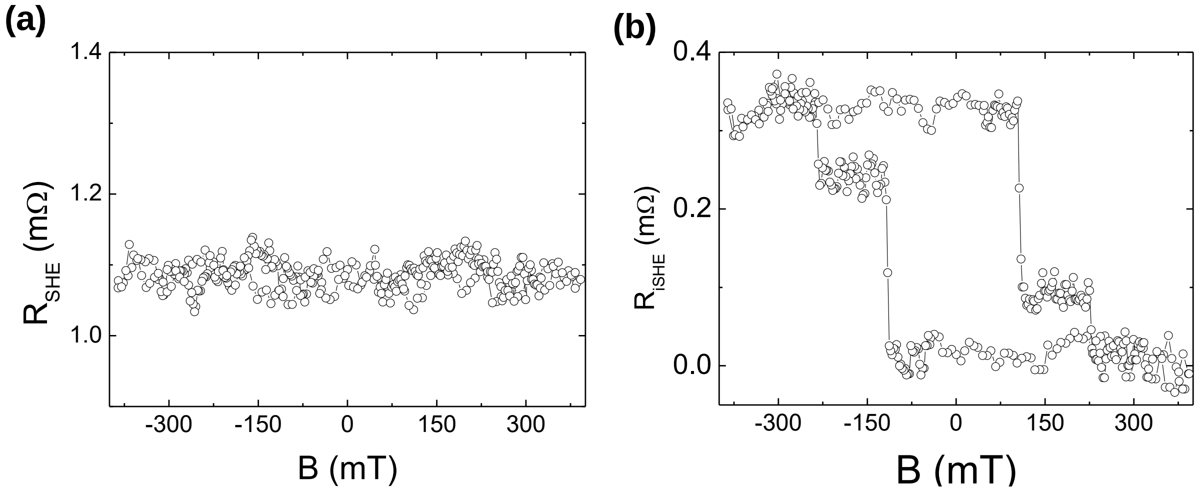

Fig. II. 7. *Second harmonic measurements in the* (a) *direct SHE and inverse SHE configurations. The signals were obtained in the sample of Fig. II. 2 (b) and (c): CoFe(15)/Pt(7) with 400 nm of Pt wire width.*

II. 5. 3. Normal Hall effect

The normal Hall effect could lead to the appearance of a signal with the same symmetry: in the antiparallel configuration the stray field produced in the SHE material by the ferromagnetic electrodes possess a component along Z, thus possibly generating a Hall voltage. This Hall voltage changes sign when going from a head-to-head to a tail-to-tail magnetic configuration, and would disappear in the parallel state.

Micro-magnetic simulations of the stray field generated by the electrode[137] shows that in the antiparallel configuration, the stray field is localized at the vicinity of the electrodes tips (*Fig. II. 8*).

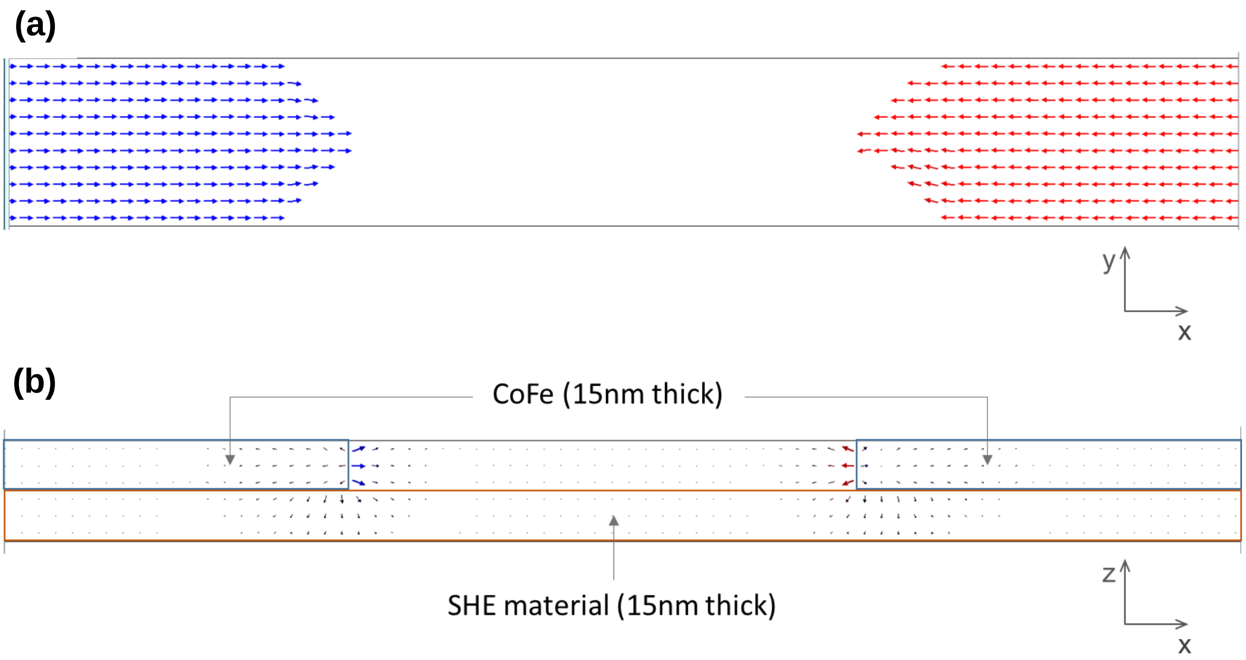

Fig. II. 8. *(a) Top view of the magnetic configuration inside the CoFe electrodes. b) Side view of the demagnetizing/stray field map arising from the CoFe electrodes. The arrows represent the stray field, which is strong only at the vicinity of the tips of the electrodes.*

For a 7 nm thick Pt layer with 15 nm thick CoFe electrodes, the average B_z component in the Pt volume is -70mT. Taking the normal Hall coefficient[138] of Pt, $R_H = -0.23\times10^{-10}m^3/C$, this leads for a 300 nm wide Pt wire to a signal of $R = \frac{R_H B_Z}{t} = 0.2\,m\Omega$, smaller than the measured spin signal (typically 12 mΩ) by two orders of magnitude. Note that this is a worst case estimation of the effect (small thickness, no deviation of the current in the cross branches).

From all the materials used here, tungsten has the largest normal Hall contribution, but for the used geometry the Hall contribution remains small, around 0.4 mΩ.

II. 5. Comparison with recent results

In order to determine the spin Hall angle in materials with short spin diffusion lengths, techniques based on lateral spin valve[130], SP-FMR, ST-FMR[92,93] and second harmonic measurements are the most used. Additionally, a new technique, the SMR is also being now used to investigate the SHE.

The results we obtained on Pt can be compared with what can be found in the literature. *Table 1* reports material parameters of Pt obtained using different methods.

Table 1: *Experimental spin Hall angle and related parameters of Pt*

Ferro	**ρ_N (μΩ.cm)**	**λ_s (nm)**	**Θ_{SHE} (%)**	**Technique**	**Reference**
NiFe	15.6	-	0.34	NL-LSV	Kimura *et al.* 2007[130]
NiFe	18.0	7	0.9	NL-LSV	Vila *et al.* 2007[113]
NiFe	7- 70	0.59 – 10.1	2 - 14	NL-LSV	Sagasta 2016[139]
NiFe	15.6	7	8	SP-FMR	Ando *et al.* 2008[92]
NiFe	41.7	10 ±2	1.3	SP-FMR	Mosendz *et al.* 2010[94]
NiFe	50	10	4	SP-FMR	Ando *et al.* 2011[95]
NiFe	41.3	3.7	8	SP-FMR	Azevedo *et al. 2011*[96]
NiFe	23.3	8.3	1.2	SP-FMR	Feng *et al. 2012*[140]
NiFe	76.9	7.7	1.3	SP-FMR	Nakayama *et al.* 2012[97]
YIG	40.8	1.5-10	3	SP-FMR	Hahn *et al.* 2013[151]
NiFe	25	4	2.7	SP-FMR	Vlaminck *et al.* 2013[98]
NiFe	98	8	2.01	SP-FMR	Hung *et al.* 2013[141]
NiFe	41.7	1.3	2.1	SP-FMR	Bai *et al.* 2013[99]
NiFe	-	1.2	8.6	SP-FMR	Zhang *et. al.* 2013[142]
NiFe	-	1.2	12	SP-FMR	Obstbaum *et al.* 2014[102]
Co	17	3.4	5.6	SP-FMR	Rojas-Sánchez *et al.* 2014[135]
-	47.6	7.3	10	SP-FMR	Manchon *et al.* 2014[143]
NiFe	27.8	1.2	2.2	ST-FMR	Kondou *et al.* 2012[103]
NiFe	20	3	7.6	ST-FMR	Liu *et. al.* 2011[93]
CoFe	27.8	2.1	4 – 15	ST-FMR	Ganguly *et al.* 2014[144]
CoFe	20	1.4	33	ST-FMR$^+$	Pai *et al.* 2015[145]
NiFe	27.8	2.1	3 - 7.5	ST-FMR	Ganguly *et al.* 2014[144]
Co	15	1.4	11	ST-FMR	Parkin *et al.* 2015[146]
NiFe	15	1.4	5	ST-FMR	Parkin *et al.* 2015[146]
NiFe	15	1.4	19	ST-FMR	Parkin *et al.* 2015[146]

YIG	83	2.4	4	SMR	Nakayama et al. 2013[118]
YIG	33 - 200	1.5	11 ± 8	SMR	Althammer *et al.* 2013[147]
CoFe	28	3	19	F/N nano-structure	*This work*
NiFe	28	3	7.5	F/N nano-structure	*This work*

For the NiFe/Pt samples, the spin Hall angle value is in good agreement with other results recently obtained using NiFe as a ferromagnetic material. The value of the spin Hall angle of CoFe/Pt samples seems pretty large, but it is close to the intrinsic value reported by Zhang *et al.*[146] in 2015, when the CoFe/Pt interface is taken into account (cf. *Chapters III* and *IV*), and it remains lower than the report of C.-F. Pai *et al.* 2015[145] in CoFe/Pt.

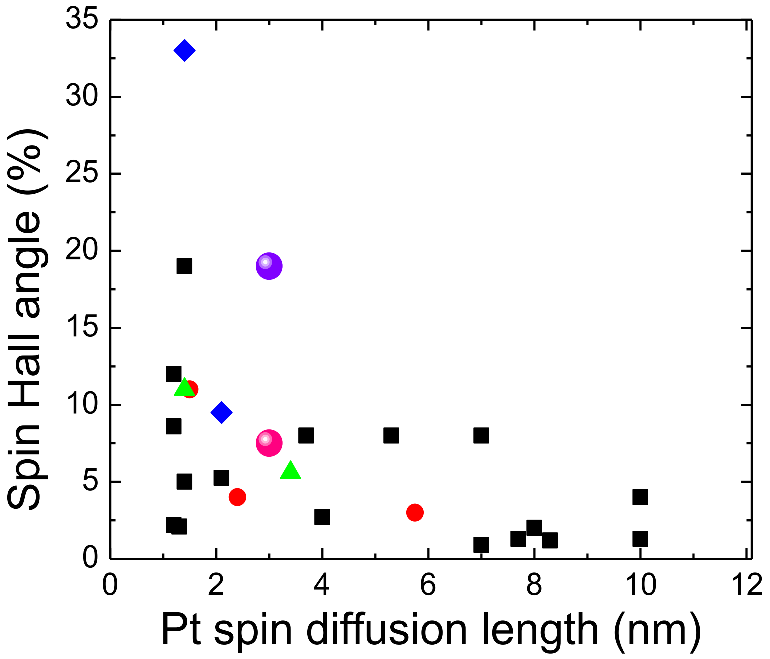

Fig. II. 9. *Spin Hall angle and spin diffusion length of Pt, obtained using SP-FMR/ST-FMR, LSV transport and SMR techniques and with different ferromagnetic materials: NiFe (black squares), CoFe (blue diamond), YIG (red circles), and Co (green triangles). Our results are represented by spheres in pink (for the NiFe/Pt system) and purple (for the CoFe/Pt system).*

To conclude, we have proposed a simple electrical device in which it is possible to realize the interconversion between charge and spin currents by SHE and ISHE. The observed behavior can be reproduced roughly using a 1D-analytical model, and more precisely using 3D-FEM simulations. We showed that it allows to extract the spin-dependent transport properties of the SHE material.

Beyond its relative simplicity, the main interest of the proposed method is that the interconversion between spin and charge currents is done using a device akin to the ferromagnetic/nonmagnetic bilayers on which most spin-orbit torques experiments rely. In standard spin-orbit torque experiments the produced spin current is observed indirectly, through its effect on magnetization. The proposed technique should thus help shedding light in the role of the SHE in spin-orbit torques.

Finally, the same design could in principle be adapted to study the conversion by SOC of other materials such as semiconductors, alloys, oxides, 2DEG[81,128], or topological insulators[148,149].

CHAPTER III: APPLICATION OF THE PROPOSED TECHNIQUE TO DIFFERENT METALS

In the previous chapter, we proposed to use a new transport technique to characterize the SHE properties of Pt, showing that it gives access to both the spin Hall angle and the spin diffusion length. In the following, we will use the same technique to measure the spin Hall angle of various materials: heavy metals like Pt, Pd, Au W and Ta, and Ti, a light metal, as a reference. The spin Hall angles of Au-based alloys: AuW and AuTa, have also been determined, and compared to the results obtained using Spin pumping techniques and lateral spin-valves.

III. 1. Application to pure metals

The proposed method for studying the spin to charge conversion has been applied to several SHE systems: Pd, Au, Ta and W. The main results are summarized in Table 2 and in *Fig. III. 1*. The observed spin signals in those systems are similar to those observed in the NiFe/Pt and CoFe/Pt systems. In particular, we observe a decrease of the spin signal amplitude with the width of the SHE wire w_N (*Fig. III. 1*).

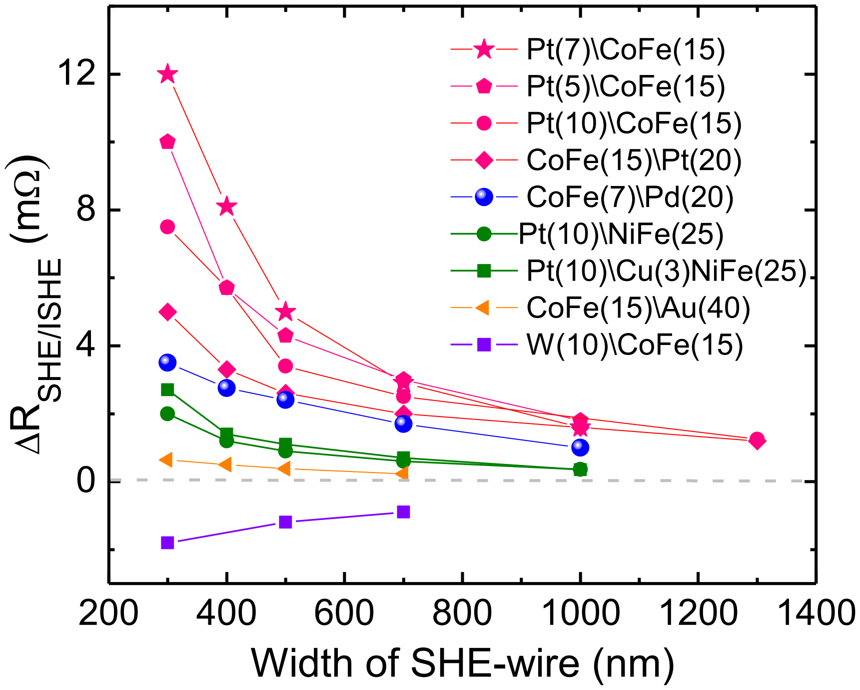

Fig. III. 1*: Measured spin signal amplitude vs. channel width, for different systems. The sign of the reported signal corresponds to the sign of the spin Hall angle of the SHE material (experimentally, the sign of the measured voltage actually depends on the stacking order, F\N or N\F).*

This can be understood by considering the SHE configuration: the spin accumulation at the top surface depends on the current density. For a given applied current, the current density and thus the signal will decrease when increasing the channel width. Note that this can also be seen in the w_N dependence of equation (II. 2).

The extracted values of the spin Hall angle are given in *Table 2.*

Table 2. Extracted material parameters*. The polarization and the spin diffusion length of the ferromagnetic materials have been taken from the literature on electrical transport in lateral spin-valves. The error bars on* Θ_{SHE} *do not take into account the uncertainty on the values of* λ_F*,* λ_N *and* P_F*, and are only related to the experimental uncertainty of the proposed technique (noise level and reproducibility from device to device).*

System	**λ_F (nm)**	**λ_N (nm)**	**ρ_F (μΩ.cm)**	**ρ_N (μΩ.cm)**	**p_F**	**Θ_{EHE} (%)**	**Θ_{SHE} (1D-Analytical) (%)**	**Θ_{SHE} (3D-FEM) (%)**
NiFe/Pt	3.5 ± 0.5	3.0 ± 0.6	30	28	0.28	0.32	4.0 ± 0.5	7.5 ± 0.5
CoFe/Pt	3.5 ± 0.5	3.0 ± 0.6	20.5	28	0.58	0.63	10.0 ± 0.5	19 ± 0.5
CoFe/Pd	3.5 ± 0.5	13 [132]	20.5	21	0.58	0.63	4.0 ± 0.5	4.5 ± 0.5
CoFe/Au	3.5 ± 0.5	35 [136]	20.5	4.2	0.58	0.63	2.5 ± 0.3	1.5 ± 0.3
CoFe/Ta	3.5 ± 0.5	1.8 [151]	20.5	200	0.58	0.63	-	-2.7 ± 3.0
CoFe/W	3.5 ± 0.5	1.4[150]	20.5	135	0.58	0.63	-	-6.5 ± 1.0
CoFe/Ti	3.5 ± 0.5	13[152]	20.5	52	0.58	0.63	-	≈ 0

As expected from previous studies, the spin Hall angle is lower for Pd than for Pt[132], and it is small in Au[136]. The values of λ_N for Ta and W have been taken from studies where the materials possess similar resistivities[151,150] (and similar growth conditions for W).

For Ta samples, and despite trials with numerous nanofabrication processes and geometries, the obtained magnetoresistances were flat. Indeed, a relatively high noise level has always been observed with the devices made with this material (+/- 2.0 mΩ). Several methods have been used including one where the F and Ta materials are deposited by shadow evaporation, in such a way that the wires and the F/NM interface are built in a single evaporation sequence in vacuum and so that the interface is expected to be clean. Our interpretation of this flat but noisy signal is that the EHE and SHE contributions roughly cancel out, so that the signal remains lower than the noise level. The error bar for Ta is thus large, because the spin signal is supposed to lie within the noise level, or that it is exactly cancel out by the EHE.

Although reports have been made of a large negative spin Hall angle in Ta [105], we find here a negative but relatively small SHE angle (-2.7%), in agreement with recent measurements using lateral spin-valves, spin pumping or spin Hall magnetoresistance[132,151.]

The spin Hall angle in the W sample (-6.5%) is clearly negative, and larger than that of Ta. Note that for those two materials, the 1D model is inaccurate and has to be considered as not applicable: the comparison between 1D and 3D calculations shows that when ρ_N is too large the 1D model overestimates the EHE contribution.

Let us now briefly discuss the results obtained using different ferromagnetic electrodes to connect the Pt stripe. Even for Pt, which is considered to be the reference SHE material, the measurement of spin Hall angles remains an important metrology problem[104,134], which underlines the need for new measurement tools such as the method proposed here.

As can be seen on *Fig. III. 1*, and the *Table 3*, different spin Hall angles are estimated when using CoFe or Py as ferromagnetic electrodes (19 % and 7.5 %, respectively). This points out the importance of interfacial effects. In this chapter, as interface effects are not taken into account in our data analysis, the calculated values of SHE angles have to be understood as effective values, *i.e.*, taken as lower bounds of the intrinsic values. A study of those interface effects will be presented in more details in *Chapter IV*.

Reference experiment with Ti

In order to estimate the contribution of the EHE in our method, we have performed a reference experiment on a CoFe(15)/Ti(20) sample. Ti is indeed a light metal (its electronic configuration is Ar $3d^2$ $4s^2$), known to have a very small spin Hall angle (*e.g.*, 0.036% measured by C. Du *et al.*[152]). The expected signal amplitudes have been calculated by FEM-simulation, assuming that $\Theta_{SHE} \approx 0$, and that all the signal comes from the EHE in the CoFe layer (*Fig. III. 2*). We observe a very nice agreement with the experimental results. This agreement between experiences and simulations can be regarded as a validation of the method used to calculate the EHE contribution.

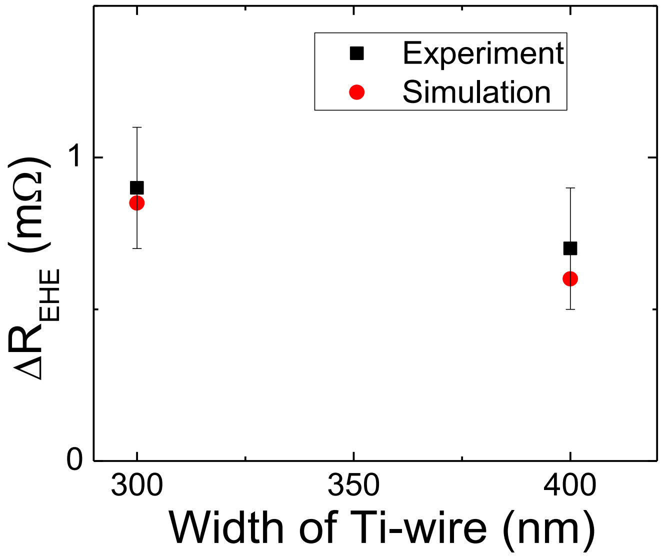

Fig. III. 2. *Experimental signal amplitudes obtained in CoFe(15)/Ti(20) samples, and signal amplitudes calculated by the 3D FEM-simulation assuming that* $\Theta_{SHE} \approx 0$*, and that all the signal comes from the EHE.*

III. 3. Application to Au-based alloys

Most of the recent reports on strong SHE focused on single heavy-elements, the main materials of interest being Pt, Ta and W. As discussed in *Chapter I*, the extrinsic mechanisms associated to the spin dependent scattering on impurities or defects are an alternative way to generate efficiently transverse spin currents[43].

We studied the SHE in AuW and AuTa alloys using the proposed spin-charge interconversion device, and compared the obtained results to those obtained in our group by spin-pumping and using lateral spin valves. These materials have been developed during the PhD of Piotr Laczkowski[153] and the post-doctoral stay of Yu Fu, in collaboration with the unité Mixte de physique CNRS/Thales Palaiseau.

The samples have been fabricated by conventional e-beam lithography, e-gun or sputtering deposition, followed by a lift-off process on thermally oxidized SiO_2 substrates. The alloy layers were deposited by co-sputtering, and are placed underneath the ferromagnetic electrodes, which are deposited using e-gun evaporation (as in *Chapter II*). A gentle ion beam etching was used before the deposition of the FM electrodes, to clean the top interface of the SHE material.

III. 2. 1. Spin Hall effect in AuW alloy

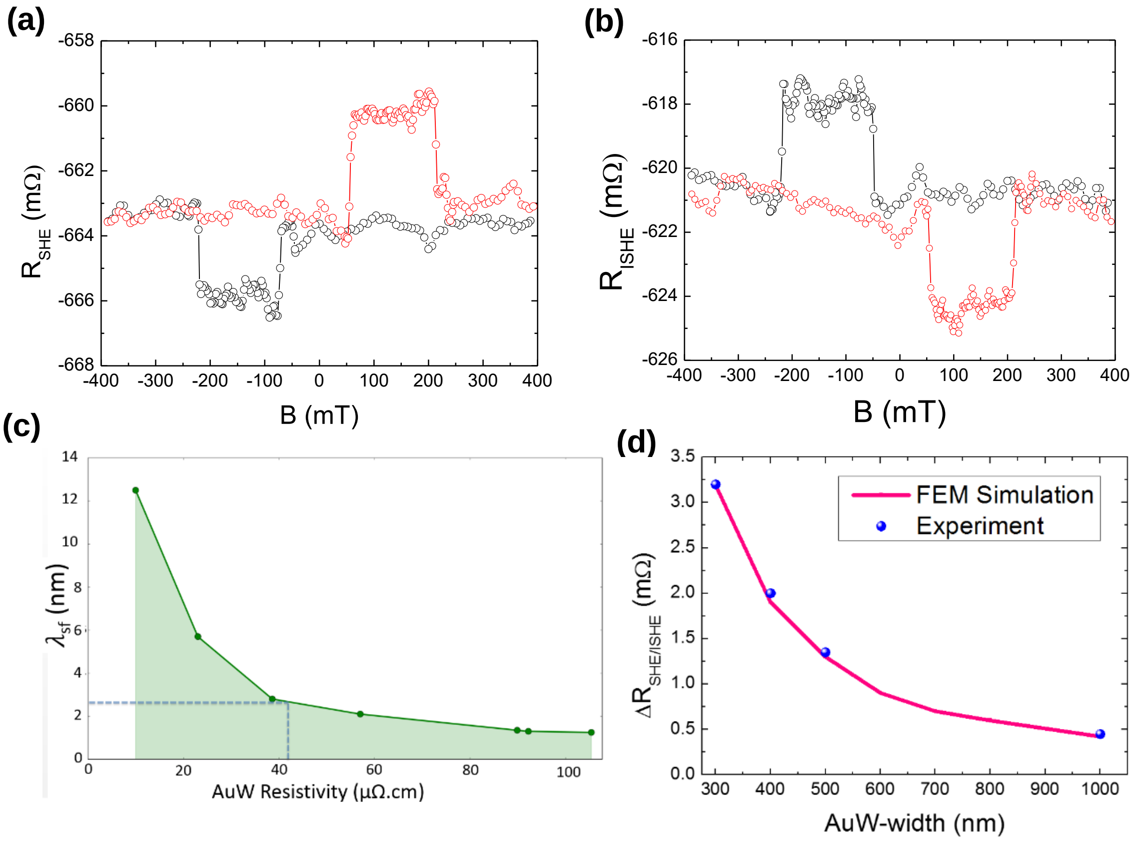

Fig. III. 3 *Experimental spin signals of (a) SHE and (b) ISHE in a CoFe/AuW sample. The schemes of the measurement setup have the same as those used previously cf. Fig. II. 1(b) and I. 1(c) (c) Variations of the spin diffusion length of AuW alloys of different stoechiometries as a function of the alloy resistivity, extracted from*[153,154]*. The values of Lsf have been measured using spin-sink experiments in lateral spin valves. (d) Amplitude of the spin signal using the new technique, and results of the finite element method simulations with a spin Hall angle of 6.5 % (the spin diffusion length of AuW is taken to be 2.8 based on the AuW resistivity of 41 μΩ.cm).*

Fig. III. 3 illustrates the spin signals of the direct and inverse SHE measured in a CoFe(15)/AuW(10) sample. The amplitude of the signals is 3.2 mΩ, for a 300 nm wide AuW-wire. The SHE and ISHE measurements reciprocate as expected. The absolute signal amplitude is about two times smaller than that of a CoFe/Pt sample with the same geometry.

The spin diffusion length of AuW alloys has been measured using a spin-sink technique in lateral spin-valves during the PhD of P. Laczkowski. The decrease of the spin diffusion length with the resistivity (and thus with the concentration in W) can be observed in

Fig. III. 3(c). From the measured resistivity of the alloy used in our experiment (41 µΩ.cm) we can infer its spin diffusion length to be 2.8 nm.

Comparison with results from lateral spin valves and SP-FMRtechniques

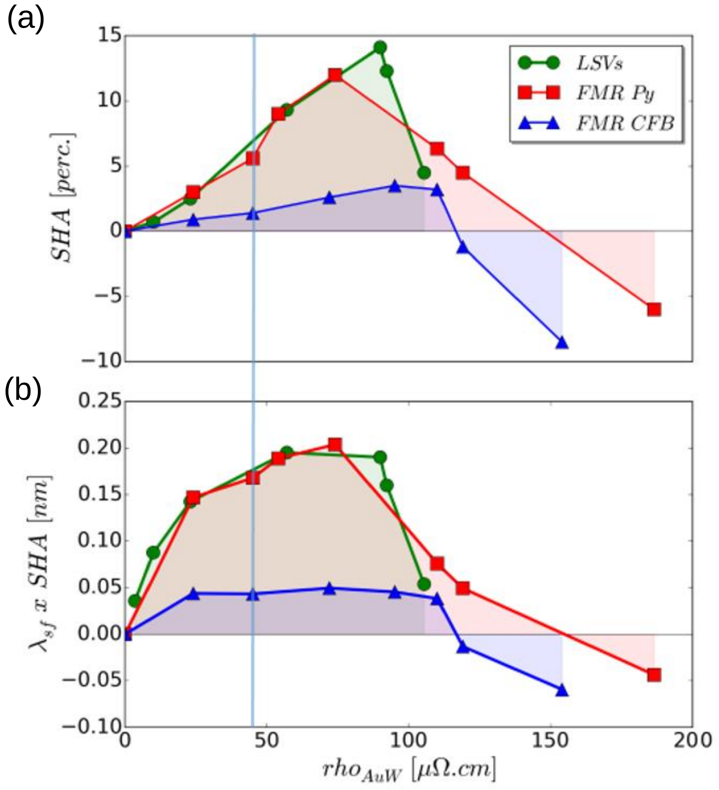

Fig. III. 4. ***Results from SP-FMR and LSV-based techniques*** [153, 154]: *Spin Hall angle (a) and product* $\lambda_{sf}\Theta_{SHE}$ *(b) as a function of the alloy resistivity. The spin Hall angles* *have been measured using LSVs (green), or SP-FMR with either NiFe - red or CoFeB electrodes*[81,155]*.*

Our experimental data are well fitted using this spin diffusion length and a spin Hall angle of 6.5%

Fig. III. 3*(*d). This value can be compared to what has been obtained prior to my PhD using SP-FMR and LSV-transport techniques. *Fig. III. 4* shows the evolution of the Spin Hall angle, and of the product $\lambda_{sf}\Theta_{SHE}$, as functions of the alloy resistivity.

The measured value is similar to which has been obtained both by spin pumping and using a LSV, when NiFe is used as ferromagnetic electrode. As said before, this value of the spin Hall angle has to be considered as an effective value, calculated by assuming the transparency of the interfaces, and therefore as a lower bound of the real value. Note also that, similarly to what was observed with the Pt system, different ferromagnetic electrodes can give different effective values: with a CoFeB electrode, spin-pumping experiments give a lower effective spin Hall angle value (6.5%).

III. 2. 2. Spin Hall effect in AuTa alloys

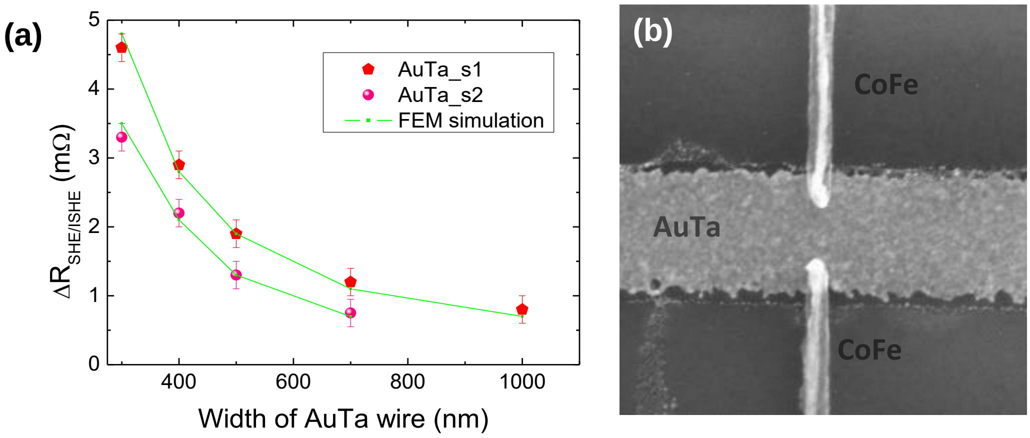

Fig. III. 5. (a) *Amplitudes of the spin signal using the proposed measurement technique, and results of FEM simulations. A good fit of the experimental data is obtained using a SDL of 2.6 nm and a spin Hall angle of 7.4% for the sample s1, and*

1.6 nm and 11% for the sample s2. (b) SEM image of a sample which was heated at 180C during the fabrication process.

The technique proposed in this manuscript has also been used to characterize $AuTa_{7.5\%}$, a new Au-based alloy which can produce a very high conversion rate (around 35% according to recent SP-FMR experiments[154] done in our laboratory).

The analysis of the experimental results of *Fig. III. 5(a)* show that the amplitude of the spin signals is not as high as expected. Two series of CoFe(15)/AuTa(10) samples have been studied, with the same nominal concentration (7.5%). The resitivities were found to depend on the fabrication process. The first sample, s1, was heated at 180°C, resulting in a resistivity ρ= 52 μΩ.cm, and thus, if one assumes that the results of ref. 154 can be applied, to a SDL of 2.6 nm. The second sample, s2 was heated only at 60°C ρ = 60 μΩ.cm, leading to a SDL of 2 nm.

The spin Hall angles corresponding to these samples using the FEM model are 7.4% and 11%, for s1 and s2, respectively. These values are much lower than what was obtained in the SP-FMR experiments (35%, cf. ref. 154) with a NiFe electrode.

The difference between the two samples could be due to the nanofabrication process. For the s1 sample, the resistivity of the AuTa alloy was around 52 μΩ.cm, and appeared to be much lower (7.5%) after the nanofabrication process. This could be due to a clustering of the Ta atoms, leading to an inhomogeneous alloy. The SEM image in *Fig. III. 5(b)* shows that indeed the AuTa wire is very rough after processing, and that there might be a problem of stability in this alloy. The origin of the difference observed with the SP-FMR experiment is not clear for now, it might also be related to the fact that the nanofabrication process could damage the alloy.

III. 3. Conclusion

In this chapter we have shown the applications of the proposed spin-to-charge interconversion device to several materials. This technique has been applied to characterize the SHE in various heavy metals. Both positive (Pt, Pd, and Au) and negative spin Hall angles (W) have been measured, which is consistent with what can be found in the literature. In a control experiment using a light metal Ti, a negligible spin Hall angle was obtained.

This technique has then be applied to newly developed alloys. The results with AuW show a good agreement with previous results obtained using SP-FMR and LSV devices with a NiFe electrode. Preliminary results on the AuTa alloy show that for alloys there might an issue concerning the stability linked to the nanofabrication process.

CHAPTER IV: PRESENCE OF INTERFACE EFFECTS

As mentioned in *Chapter II* and *Chapter III*, the effective values of the spin Hall angle measured in Pt are found to depend on the nature of the ferromagnetic layer: a smaller spin Hall angle was in particular measured in the NiFe/Pt system (7.5%) than in the CoFe/Pt system (19%).

This chapter focuses on the origin of this effect. After determining the transport parameters of Co, using the gap dependence of LSVs, we will compare the values of the effective spin Hall angle in Pt measured using CoFe, Co, and NiFe electrodes. We will show that interfaces play a significant role on the spin signal, notably by studying the insertion of a Cu layer in-between the ferromagnetic and Pt layers. By comparing the effective spin Hall angle obtained on all those systems, we show that the NiFe/Pt interface is clearly not transparent, and we provide a lower bound for the value of the spin Hall angle in Pt.

IV. 1. Evaluation of the transport parameters of Co

The extraordinary Hall angle of Co(15nm) has been measured using four probes measurements in Hall crosses, as shown in *Fig. IV. 1*.

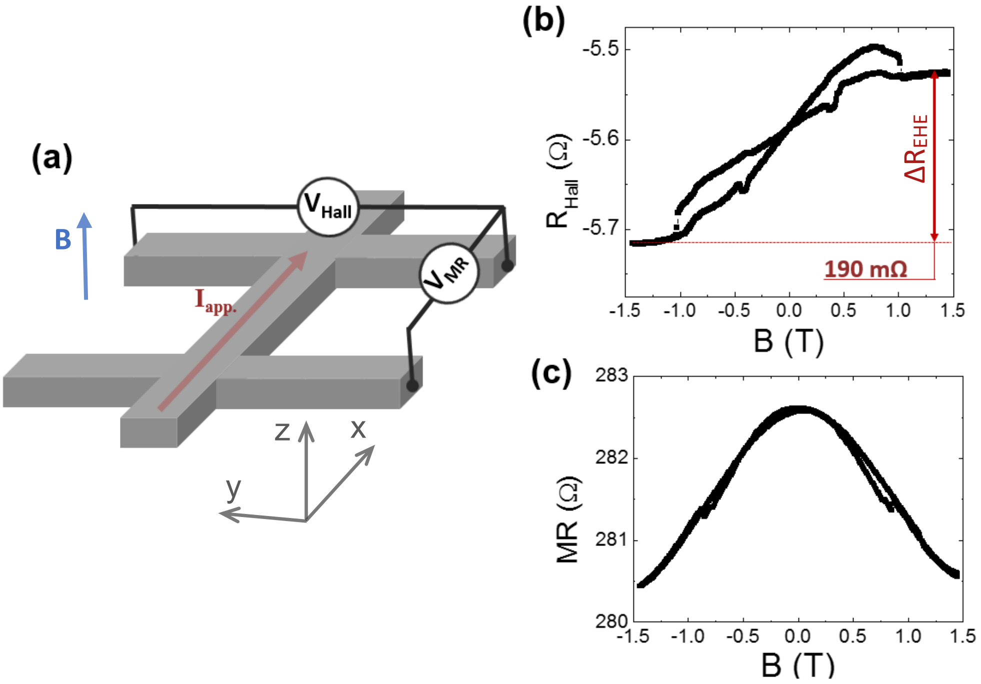

Fig. IV. 1. *(a) Schematic of the measurement setup in Hall crosses: The in-plane current is applied along the x direction and the out-plane magnetic field is applied along the z direction. 4-probe MR and Hall measurements were simultaneously performed. The resulting signals are expressed in Ohms, by dividing the measured voltage by the applied current.: (b) EHE loop and (c) MR loop.*

The resistivity of the Co layer has been measured both by using the Van der Pauw method in the single Hall cross, and by using a 4-probe resistance measurement along the Co wire. Both methods give ρ_{Co} = 25.2 µΩ.cm at room temperature.

The extraordinary Hall angle can be extracted from the extraordinary Hall resistance: $\Theta_{EHE} = \frac{h_{Co}\Delta R_{EHE}}{\rho_{Co}}$ = 1.13%, where h_{Co} = *15 nm* is the thickness of the cross and ΔR_{EHE} = 190 mΩ is the extraordinary Hall resistance shown in *Fig. IV. 1b.* Additionally, the MR loop in *Fig. IV. 1c* demonstrates that the AMR of Co is around 0.7 %[156].

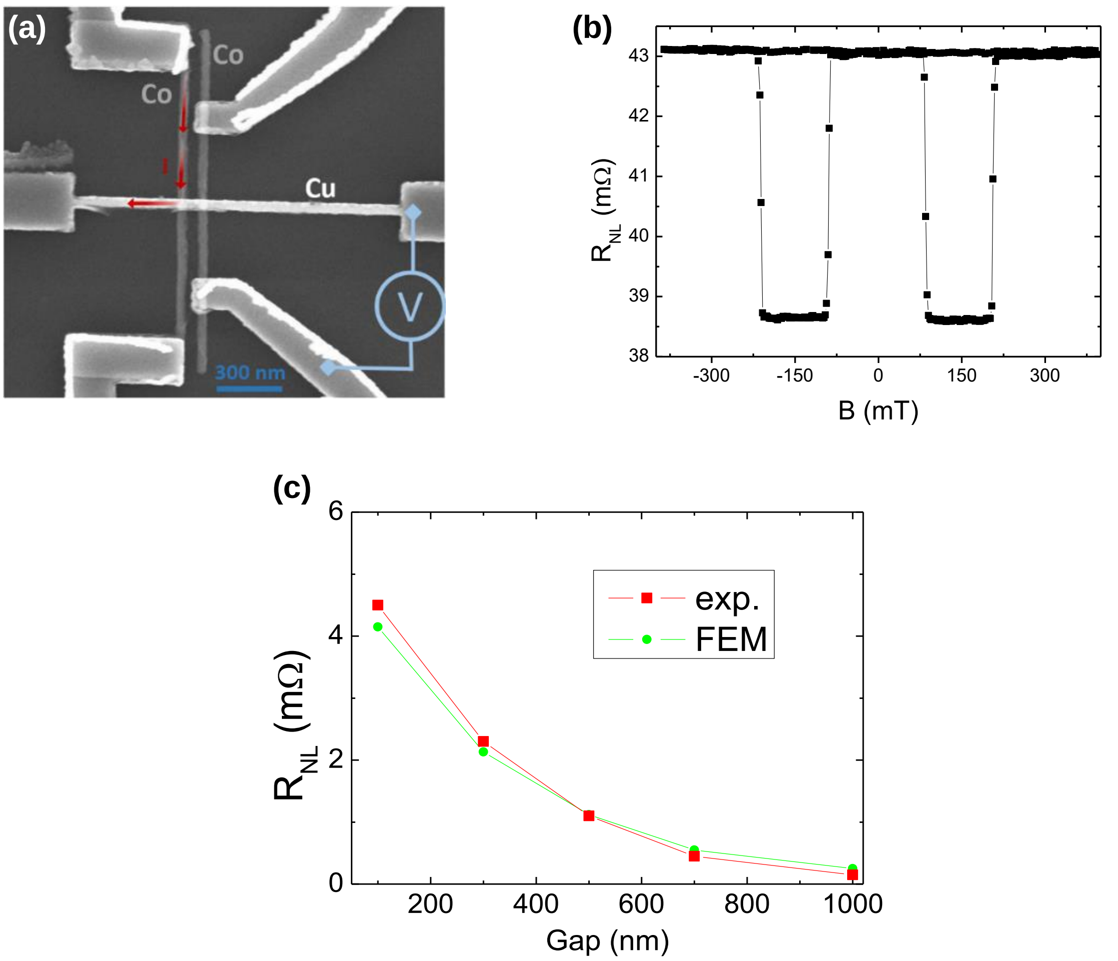

Fig. *IV. 2.* *SEM image of the LSV, and schematic of the NL measurement setup. (b) NL spin signal for a gap of 100 nm. (c) Amplitude of the spin signal and results obtained by FEM simulations.*

We performed transport experiments on LSVs made of Co-Cu-Co to extract the polarization and the spin diffusion length of Co (*cf. Fig. IV. 2*). The schematic non-local measurement setup is shown on *Fig. IV. 2a*. The charge current is applied from one Co electrode to the Cu channel leading to a spin accumulation at the Co/Cu interface. The PSC is injected into the channel and diffuses up to the second Co electrode where the spin accumulation is probed by measuring the voltage drop at this interface.

The non-local signal is shown in *Fig. IV. 2b*. The value of the voltage drops down when the magnetizations in the Co wires are antiparallel. By using FEM simulation we can reproduce the amplitude evolution of the spin signals with the gap(see more in r*ef. 133*), using as transport parameter of Cu and Co λ_{Cu} = 320 nm, λ_{Co} = 38 nm, ρ_{Cu} = 5.2

μΩ.cm, ρ_{Co} = 25.2 μΩ.cm and p_F = 0.1. The free parameters used to fit the experimental data are λ_{Co} and p_F. The obtained values are in agreement with a previous work by Villamor *et al.*[157].

IV. 2. Nature of the ferromagnetic electrodes and effective spin Hall angle

In order to study the influence of the F/N interfaces, we firstly performed measurements using CoFe, Co, and NiFe electrodes deposited on the top of a Pt wire similarly to what was shown in *Fig. II. 1(a)* and *Fig. II. 1(c).*

The dependence of the spin signal on the type of electrode is shown in *Fig. IV. 3*. The amplitude of the spin signal probed by NiFe is the lowest. The signal from the CoFe/Pt system is stronger than that of the Co/Pt sample, for the same geometrical parameters.

The comparison of the spin signals can be considered as meaningful, because the resistivities of the different ferromagnets, measured using a four probe configuration, are similar (30.5 μΩcm for NiFe, 25.2 μΩcm for Co, 20.0 for CoFe). Note also that the differences of polarization of the ferromagnets cannot explain the change of spin signal. Indeed, even though the polarization of Co (0.1%) is lower than that of NiFe (0.26%[133]), the spin signal amplitude of the Co/Pt system is stronger than that of NiFe/Pt.

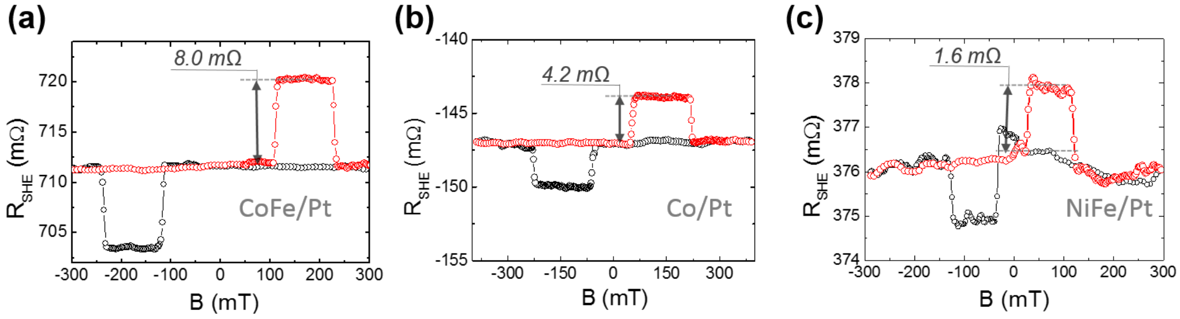

Fig. IV. 3. *Comparison of the spin signals using different ferromagnetic layers. (a) CoFe(15)/Pt(7), (b) Co(15)/Pt(7) and NiFe(15)/Pt(7) with the Pt wide of 400 nm show the spin signals of 8.0, 4.2, and 1.6 mΩ, respectively.*

This problem also appears when calculating the effective spin Hall angle.

Fig. IV. 4 shows the Pt-width dependences of the spin signal amplitudes in different systems. The spin signal amplitudes decrease in accordance with the increase of the Pt wire width, which leads to the reduction of the resistances of the systems.

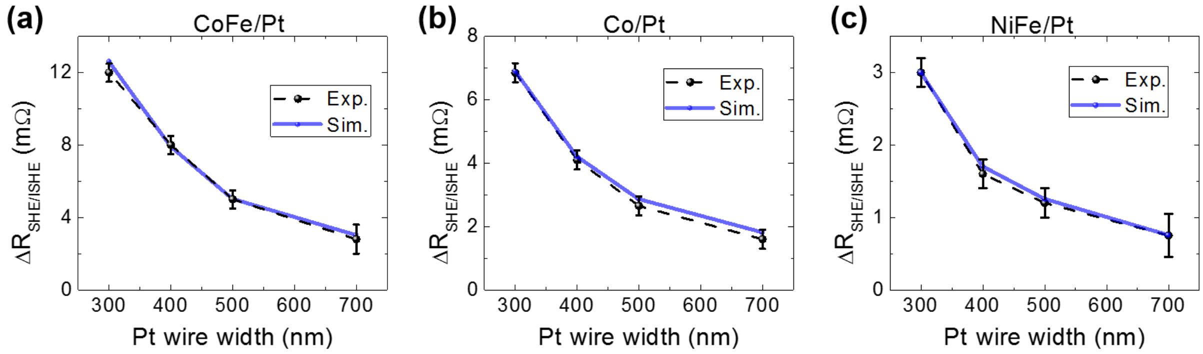

Fig. IV. 4. *Simulated and experimental amplitudes of the spin signals as a function of the Pt-wire width in systems of (a) CoFe/Pt, (b) Co/Pt, (c) NiFe/Pt.*

FEM simulation were performed to extract the effective spin Hall angles. As was done previously, the interfaces in the simulations were assumed to be transparent to the spin currents, as well as perfectly conductive to the charge currents. The parameters for the simulations were taken from *Section IV. 1* for the Co electrode and from *Chapters II* and *III* for the CoFe and NiFe electrodes. The experimental curves are well fitted in *Fig. IV. 4* using the effective spin Hall angle shown in *Table 3.*

Table 3 *Effective values of the Pt spin Hall angles extracted using FEM simulations*

System	**Θ_{EHE} (%)**	**$\lambda_s\Theta_{SHE}$ (nm)**	**Θ_{SHE} (%)**
CoFe/Pt	0.63	0.56	24.5
Co/Pt	1.13	0.62	27
NiFe/Pt	0.32	0.25	11

Measurements made in a Hall cross patterned in the 7 nm thick Pt wire give a resistivity of *36 μΩ.cm*. If one assumes that both the spin and momentum scattering rates increase similarly when the resistivity increases, the product of the spin Hall angle by the spin diffusion length of Pt is preserved [104]. The effective value *of* $\rho_{Pt}\lambda_{Pt}$ measured in *Chapter II* and averaged over several Pt thicknesses is $0.84 \pm 0.17\ f\Omega.m^2$ for the system of CoFe/Pt (see *Section II. 3*). The spin diffusion length of the 7nm thick Pt layer can then be inferred to be $\lambda_{Pt} = 2.3\ nm$. The simulations are performed using this values.

Table 3 shows that the high values of effective spin Hall angles are obtained with CoFe and Co electrodes, with a value of $\Theta_{Pt}\lambda_{Pt}$ close to what was measured in *Chapter II*. ($\Theta_{Pt}\lambda_{Pt} = 0.56$ nm for CoFe in *Table 3,* $\Theta_{Pt}\lambda_{Pt} = 0.57$ nm for CoFe in *Table 2*). The value of $\Theta_{Pt}\lambda_{Pt}$ for NiFe/Pt is also close to the value obtained in *Chapter III* on this system (0.23 nm instead of 0.25 nm*)*.

The discrepancy between the values obtained using Co (or CoFe) or NiFe show that the measured spin Hall angles have to be considered as effective. Our interpretation is that the origin of this discrepancy is that interface effects are neglected in our analysis.

The importance of such effects has been indeed found to be relatively great. For instance, using a SP-FMR technique J. C. Rojas Sanchez *et al.* [135] attributed a significant role of the spin memory loss at the Co/Pt interface. This mechanism takes into account the probability of spin relaxation at a resistive interface, leading to a depolarization of the current. The spin reflection at the ferromagnet/Pt interface has also been proposed by W. Zhang *et al.*[146] to explain results obtained using the ST-FMR technique.

The central idea is that part of the spin current is lost at the interface, thus lowering the apparent conversion rate between charge and spin current. In that sense, the effective spin Hall angles which are extracted while considering that all interfaces are transparent are lower bound of the real values.

Thus, the differences observed for the spin signal amplitudes of the Co/Pt, NiFe/Pt and CoFe/Pt systems could be due to the different transparencies of their interface relatively to the spin current.

The similar values of the effective spin Hall angles of Pt in the systems with Co and CoFe reveals that the Co/Pt and CoFe/Pt interfaces play a similar role to the spin currents. The highest value of Θ_{SHE} probed by Co shows that Co/Pt interface is very transparent. The smallest value of Θ_{SHE} in the NiFe/Pt samples however demonstrates the bad quality (exhibiting very high spin losses) of the NiFe/Pt.

Concerning this poor quality of the NiFe/Pt interface, our results are in line with a recent work performed by the group of Kelly *et al.*[158], where a very large depolarization due to Rashba field was found by ab initio calculation at the NiFe/Pt interface.

IV. 3. Insertion of a nonmagnetic material

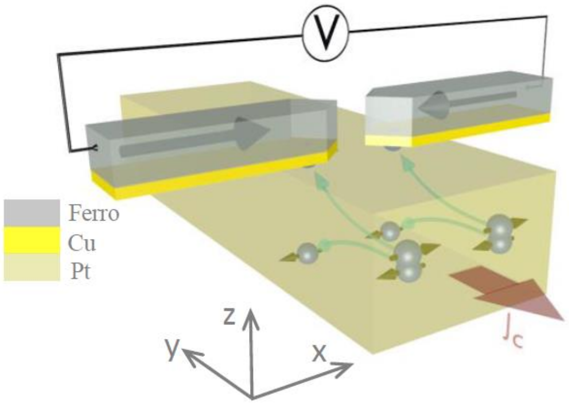

Fig. IV. 5. *Scheme of the SHE device with inserting the Cu-layer.*

A simple way to study the effect of the interface is to add, in-between the ferromagnetic and SHE layer, a nonmagnetic layer such as Cu, possessing a long spin diffusion length. As such, this non-magnetic layer can be considered as passively transmitting the PSC in-between the ferromagnetic and SHE layers.

Fig. IV. 5 shows how the device proposed in this manuscript can be adapted by inserting a Cu layer. Note that there is also a Ti(3nm) buffer layer, not shown in this Fig., which is not active (except for its electrical shunting effect) *cf. Fig. III. 2*. The Ti and Pt layers were deposited during a single evaporation step. The 3nm-Cu layer is deposited with the pattern of the ferromagnetic electrodes.

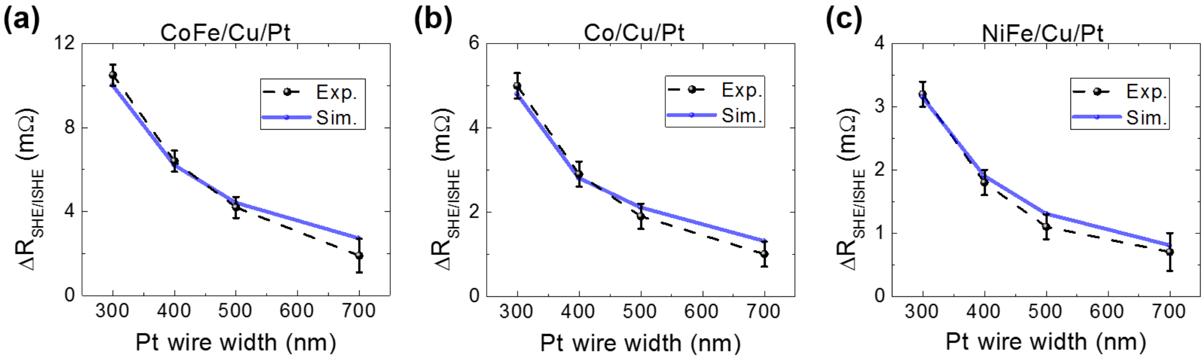

Fig. IV. 6. *Simulated and experimental amplitudes of the spin signal as a function of the Pt wire width, in (a) CoFe/Cu/Pt, (b) Co/Cu/Pt, and (c) NiFe/Cu/Pt, and using the design of Fig. IV. 5.*

The results obtained when inserting Cu are shown in *Fig. IV. 6,* which plots for the different ferromagnetic materials the simulated and experimental amplitudes of the spin signals. By fitting the experimental data *Fig. IV. 6* , the effective spin Hall angles of Pt (still calculated with the assumption of perfectly transparent interfaces) are given in *Table 4.*

Table 4 *Effective values of the Pt spin Hall angles, extracted using the FEM simulation shown in Fig. IV. 6 with a resistivity of the Cu insertion of 5.2 µΩ.cm.*

System	**Θ_{EHE} (%)**	**$\lambda_s\Theta_{SHE}$ (nm)**	**Θ_{SHE} (%)**
CoFe/Cu/Pt	0.63	*0.62*	27
Co/Cu/Pt	1.13	*0.62*	27
NiFe/Cu/Pt	0.32	*0.36*	15.5

These results can be analyzed as follows:

- Concerning the CoFe/Pt and Co/Pt systems, the insertion of Cu does not modify strongly the value of the effective spin Hall angle, which is found in both case to be 27%. It suggests that the transparency is very high in those systems.
- The value of 27% for the effective spin Hall angle in Pt is very large, but according to our analysis it remains a lower bound of the exact spin Hall angle.

- Concerning the NiFe/Pt system, the insertion of Cu improves the value of the effective spin Hall angle (from 11% to 15%), which shows that the combined transparency of the NiFe/Cu and Cu/Pt interfaces is better than that of the NiFe/Pt interface.
- The NiFe/Cu/Pt system exhibits a spin Hall angle of 15.5%, much lower than that of the Co and CoFe-based systems. It is surprising that by inserting the Cu layer, we did not retrieve the high values observed with Co and CoFe. As the Cu/Pt interface is also probed in the Co/Cu/Pt and CoFe/Cu/Pt stacks, this low value of the spin Hall angle might be the result of a lower transparency at the NiFe/Cu interface. It could also be due to the fact that the electrical resistance of the interface must actually be taken into account.
- The use of a NiFe electrode is found to be an awful way to probe the SHE in Pt, or to do spin-orbit torques experiments. Co and CoFe seems to be two good candidates, with a slight preference for CoFe.

IV. 4. Conclusion

The value of the spin Hall angle measured with the technique proposed in *Chapter II* is found to be an effective value, varying with the nature of the ferromagnetic electrode, in particular leading to a low effective spin Hall angle for the NiFe/Pt system. Our interpretation of these variations is that it is due to interface effects, which are already pointed at in the literature for their importance[135,146,145]. The neglecting of these interface effects when extracting the spin Hall angle values implies that the obtained effective spin Hall angle angles have to be considered as lower bound of the exact spin Hall angle.

The insertion of Cu layers lead to an important improvement of the transparency in the NiFe/Pt system, but does not modify strongly the value of the spin Hall angle in the CoFe/Pt and Co/Pt systems. This comforts previous studies (*cf. Table 1* and *Fig. II. 9*) showing that the NiFe/Pt system might not be a very good candidate to study spin-charge conversion effects or spin-orbit torques.

If several questions, such as the microscopic origin of the non-transparency, or the low effective spin Hall angle of the NiFe/Cu/Pt, remain unanswered, our results show that the proposed technique is a promising tool to study the role of interfaces.

CHAPTER V: DOMAIN WALL DETECTION BY DIRECT AND INVERSE SHE

Domain wall (DW) manipulation in spintronic nanostructures has become a very active field of research during the two last decades, as nanofabrication techniques allowed to isolate a single domain wall in a nanowire, and because of the discovery of spin transfer torques acting on DWs[159,160]. Recently, the interest towards current-induced DW motion increased, when it appeared that the angular momentum carried by PSC can be used to manipulate DWs. This can be done in lateral nanostructures, using non-local measurements[161,162], but the most exciting way to produce PSCs is obviously the use of spin orbit effects such as the spin Hall effect (SHE)[75,84] and the Rashba effects[82], which can generate SOTs in a ferromagnetic layer[65,105,163]. Beyond the fundamental questions concerning the physics of spin transfer and spin-orbit torques, this field of research has been driven by possible spintronic applications such as magnetic memories[164] and logic devices[165].

In this chapter, we will show that if the SHE can generate SOTs, it is also possible to use the SHE or the ISHE to detect the presence of a DW. A DW in a ferromagnetic wire can indeed be used to inject or detect a PSC in an adjacent SHE nanowire. The injected PSC can then be transformed by ISHE into a voltage, thus allowing the electrical detection of the DW. Conversely, in the reciprocal measurement scheme, the spin accumulation produced by SHE can be used to probe the presence of a DW.

After explaining the measurement principle, we will give the main results, and show that the use of simulations allows extracting the spin Hall angle.

V. 1. Principle

Fig. V. 1 illustrates the principle of the detection method by ISHE. W. Savero Torres *et al.* have recently shown that a DW in a ferromagnetic nanowire can be used to inject or detect a PSC in an adjacent non-magnetic nanowire[166]. The same kind of nanostructure, with a different electrical setup, also allowed to perform non-local measurements with high spin signal amplitudes[167.]

Here, the principle is to inject the PSC from a ferromagnetic wire into a SHE wire. A constriction is thus patterned in the ferromagnetic wire on top of the SHE material, in order to pin a DW (cf. *Fig. V. 1*). When a current is applied along the ferromagnetic wire, part of the charge current is deflected in the SHE material, thus creating a spin accumulation. When a DW is pinned at the constriction, the spin accumulation profile leads to the appearance of a PSC along the Z direction. This charge current is then converted into a charge current by ISHE[75], according to the equation $\boldsymbol{J_C} = \Theta_{SHE}\, \boldsymbol{J_S} \times \boldsymbol{s}$. In the open circuit conditions used here, it will create a voltage along the SHE wire. When there is no DW, we will show below that there is no injected PSC, and thus no voltage. Also, we will see that tail-to-tail and head-to-head DWs leads to spin accumulations of opposite signs, and thus to opposite voltages.

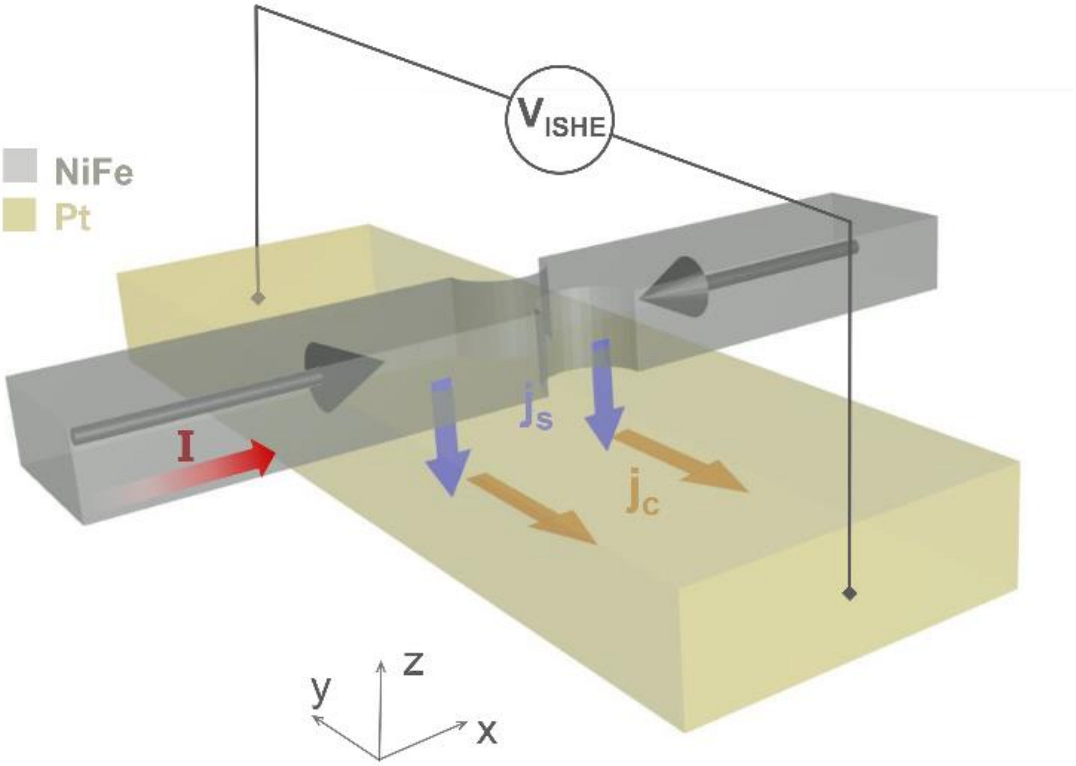

Fig. V. 1. *Scheme of the DW detection device. The ferromagnetic nanowire is connected to the SHE nanowire, made of Pt. The black arrows represent the magnetization direction when a DW is pinned. Magnetic fields are applied along the X direction. An applied charge current* J_c *flows along the ferromagnetic wire, and when a DW is pinned it leads to the injection of a spin current* J_S *along the Z direction, into the SHE wire. This spin current is then converted in a charge current along Y by ISHE.*

V. 2. Nanofabrication and experimental results

Similarly to the nanostructures of the previous chapters, the samples have been fabricated by conventional e-beam lithography, e-gun deposition, and lift-off processes on thermally oxidized SiO_2 substrate. The chosen materials are $Ni_{81}Fe_{19}$ and Pt, as they are archetypal ferromagnetic and SHE materials, and because their magnetic behavior and spin transport properties have been previously precisely characterized[168,169]. The top surface of the Pt nanowire is cleaned by Ar ion etching prior to the deposition of the $Ni_{81}Fe_{19}$ nanowire. The last step consist in adding Au electrical contacts.

Fig. V. 2(a) and *Fig. V. 2(b)* exhibit the SEM image of the resulting nanostructure, together with the measurement set-up in the SHE and ISHE configurations. The thicknesses of both layers is 20 nm. The widths of the $Ni_{81}Fe_{19}$ and Pt nanowires are 100 and 500 nm, respectively. The constriction is patterned by e-beam using a dose modulation. Efforts have been made during the mark detection process in order to precisely overlay the constriction on the middle of the SHE stripe. This was ensured by using quite long and averaged detection scans on the alignment mark, prior to the patterning of both the SHE and ferromagnetic wires.

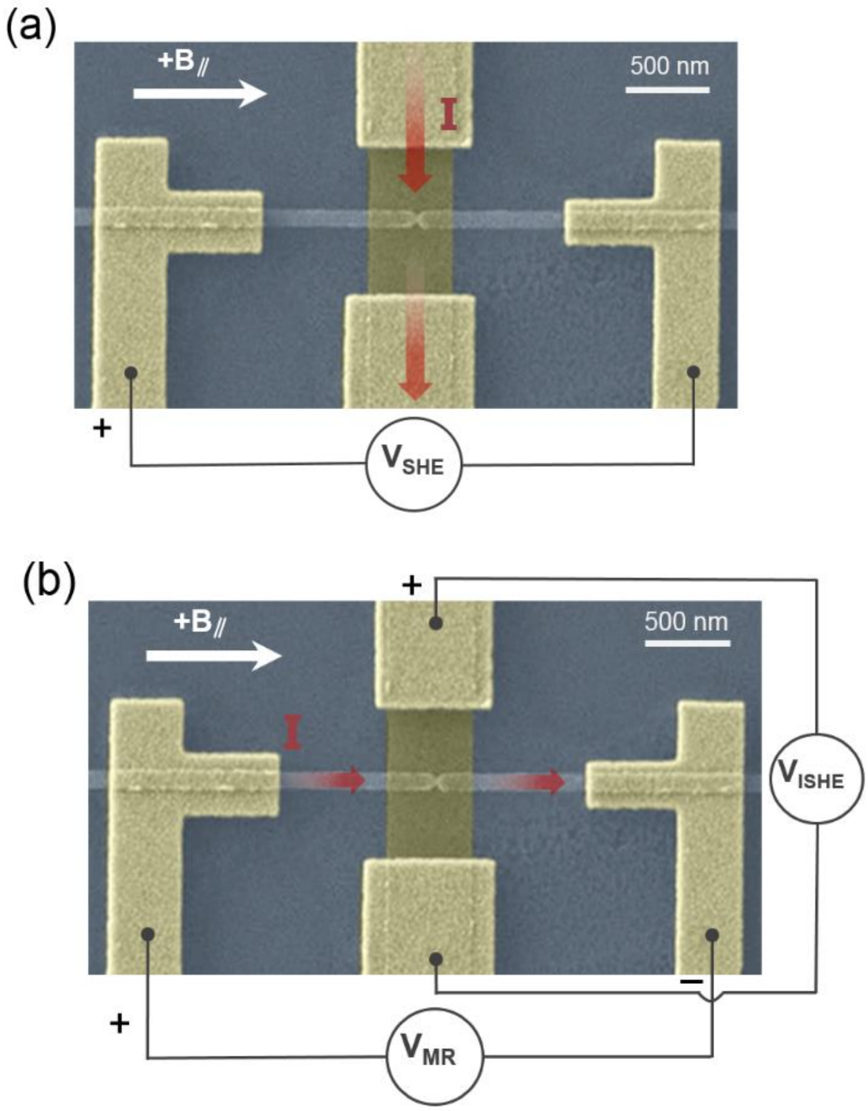

Fig. V. 2. *(a) and (b): SEM images of the device (with artificial colors), representing the measurement configurations for the domain wall detection by the SHE (a) and by ISHE (b).*

The transport measurements were performed using a lock-in amplifier working at 732 Hz, with an applied current of 100 or 200 µA. The spin signal R is, as usual, defined as the ratio between the detected voltage and the applied current.

In all experiments, the field is applied along the ferromagnetic wire. A nucleation pad (unseen in the *Fig. V. 2*) is patterned at one end of the ferromagnetic nanowire, so that the switching occurs by nucleation in the pad, followed by DW propagation along the wire, DW pinning on the constriction, DW depinning at higher field, and finally magnetic saturation by DW propagation towards the end of the nanowire[169].

In *Fig. V. 2(b)*, we added a simultaneous two-probe measurement of the nanowire magnetoresistance, in order to detect the magnetization switching by Magnon magneto-resistance[169].

The main result of this chapter is shown in *Fig. V. 3.*

The sharp spin signal variations correspond to the pinning and depinning of the DW on the constriction. As already discussed, when the DW gets pinned, the injected spin current is converted by ISHE into a charge current in the Pt wire (*Fig. V. 3. a)*. Also, the signs of these variations are opposite for head-to-head (positive fields) and tail to tail (negative fields) DWs.

As expected from Onsager relations, the obtained signal is similar in the ISHE configuration *Fig. V. 3. b*. The amplitude of the signal is of 1.0 mΩ in both the SHE and ISHE configurations.

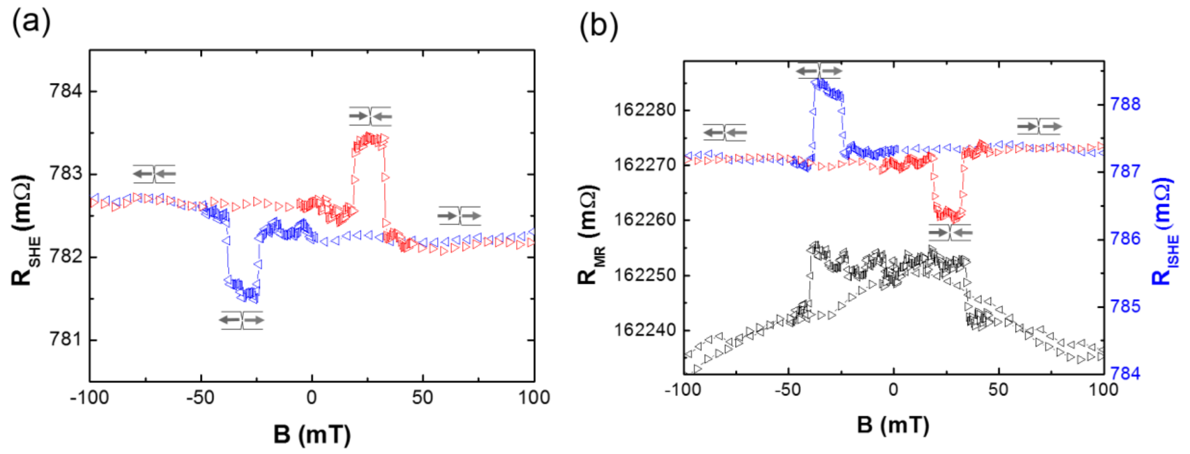

Fig. V. 3 *Spin signals obtained by applying a magnetic field along the ferromagnetic nanowire direction. (a) Spin signal in the SHE configuration. The arrows represent the magnetic configuration along the ferromagnetic wire. The spin signal variations correspond to the introduction and to the depinning of a DW from the constriction. (b) Spin signal in the ISHE configuration (in blue-red), and two-probe magnetoresistance measurement along the ferromagnetic wire (in black). Both curves have been obtained simultaneously.*

As explained in *Chapter II*, magnetoresistance effects, such as anisotropic, magnon or giant magnetoresistances, could not lead to the observed signal, which is odd in field. A planar Hall effect contribution would also be even in field, and spincaloritronic effects can be ruled out, as for these small applied current densities the signal is found to vary linearly with the current.

However, the normal and the extraordinary Hall effects possess the right symmetry in field, and could contribute to the observed signal. Simulations of the normal Hall effect in Pt, which is due to the stray field of the electrodes, show that its contribution is insignificant[168]. The extraordinary Hall angle of NiFe has been measured in patterned Hall crosses, and found to be of 0.32%. FEM simulations (described below) show that the EHE plays a significant role, with a contribution of around 28% of the observed spin signal. This contribution could be reduced by using thinner NiFe wires, but in any case it was taken into account carefully for the evaluation of the spin Hall angle of Pt.

If the signal is mostly due to the SHE, two features of the obtained loops differs from what is expected from a simple analysis. The first one is that the overall offset is expected to be zero. The unexpected offset of the transverse voltages varies from device to device. We attribute it to imperfections of the nanofabrication, which can slightly break the symmetry of the device. For instance, let us assume that in the SHE configuration the two sides of the ferromagnetic nanowire are slightly misaligned. There would appear a voltage drop between the two sides, due to the charge current along the SHE wire. Small misalignments (typically 10-20 nm) could explain the appearance, the magnitude, and the random sign of the offset resistances.

The second feature is the small variation of the spin signal between saturated states in positive and negative fields (around 0.16 mΩ). This offset between the two saturated has necessarily another origin than the overall offset discussed previously, because it is dependent on the magnetization orientation. It implies that when there is no pinned domain wall the spin currents do not cancel out. Its existence pleads here again for an asymmetry, but relevant to the spin current injection: simulations show that a geometric asymmetry, such as a not well centered notch, or a misalignment, cannot lead to such an effect. The origin of this offset might be for instance due to an asymmetry of the spin transport properties (*e.g.*, the interface transparency), leading to an asymmetry of the spin accumulations. Such asymmetries can also be observed in LSVs[170,171].

The pinning and depinning fields are similar to those observed previously in similar nanowires[166,172]. Also, the MR curve of *Fig. V. 2b* is mostly due to the MMR, with possibly a small AMR contribution[169]. The depinning field measured in the MR curve is consistent with the value observed in the simultaneous ISHE measurement. Note that the pinning field is difficult to measure in the MR curve, because of the shunting effect of the SHE wire below the pinned DW.

V. 3. Simulations and extraction of the SHE parameters

In order to estimate the EHE contribution and the spin Hall angle of Pt, a finite element method (FEM) simulation was performed within the framework of a 2 spin-current drift diffusion model[173], with collinear magnetization of the ferromagnetic wire along the easy axis. The results are shown in *Fig. V. 4*. As for *Chapters II* and *III*, the simulations were performed using the free softwares GMSH[174] for geometry construction and mesh generation and post-processing, and the associated solver GETDP[175]. Further details concerning the FEM model can be found in *Annexes B* or in *ref.* 168.

Fig. 3 illustrates the results of the FEM simulations. In the ISHE configuration, as all the equations are linear, a unit current of 1A is applied along the ferromagnetic wire so the voltage values are in unit of Volts. As seen in *Fig. V. 4*a, the current is deflected to the Pt wire because of the resistivity difference between Pt and $Ni_{81}Fe_{19}$ (ρ_{Pt} = 28.0 μΩcm and ρ_{NiFe} = 30.5 μΩcm), and because of the device geometry. This leads to the appearance of hot spots of the spin accumulation where the current gets in and out of the SHE material, as seen in *Fig. V. 4*b and V. 4c.

When there is no DW pinned at the constriction, the spin accumulation profile is antisymmetric *cf. Fig. V. 4b*, so that the average Z component of the PSC is equal to zero. In that case there is spin injection from one of the ferromagnetic wire, and spin extraction from the other ferromagnetic wire.

When a DW is pinned, however, the spin accumulation pattern is symmetric *Fig. V. 4c*, the total Z component of the PSC is non-zero, which leads to the appearance of the ISHE signal experimentally observed. Also, in *Fig. V. 4*b we can see at the vicinity of the DW a slight spin accumulation, around 10 times weaker than that of the hot spots, due to the small current density in the ferromagnetic wire. Nonetheless, the contribution of this spin accumulation to the transverse voltage remains relatively small.

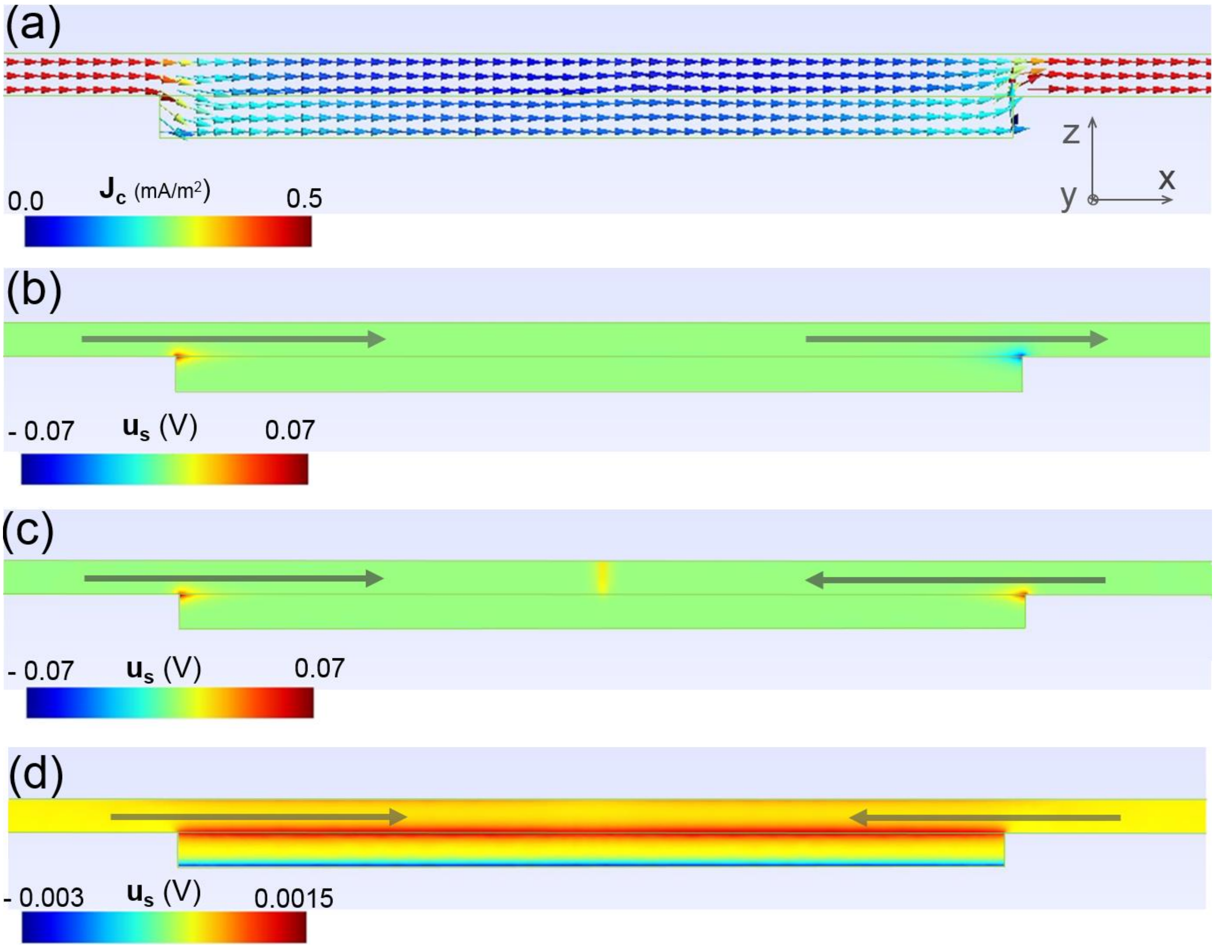

Fig. V. 4. *Results of 3D finite element method simulations. (a) Cross section perpendicular to the SHE wire, showing the current lines in the ISHE configuration. The upper part is the ferromagnetic wire, the lower part is the SHE wire. (b) and (c) Cross-sections showing the spin accumulation* u_S *(i.e., the difference between electrochemical potentials). In (b) the wire magnetization is saturated, in (c) a head-to-head DW is pinned on the constriction. (d) Spin accumulation in the SHE configuration.*

For the simulation of the SHE configuration, the current is applied along the SHE wire. A large PSC appears along the Z direction, due to the SHE. The spin accumulation at the top surface *Fig. V. 4(d*) of the SHE material is probed by the ferromagnetic wire: the fermi level tends to align with the electrochemical potential corresponding to the magnetization direction. When a DW is pinned, the two parts of the ferromagnetic wire separated by the constriction detect opposite electrochemical potentials, thus leading to the observed spin signal.

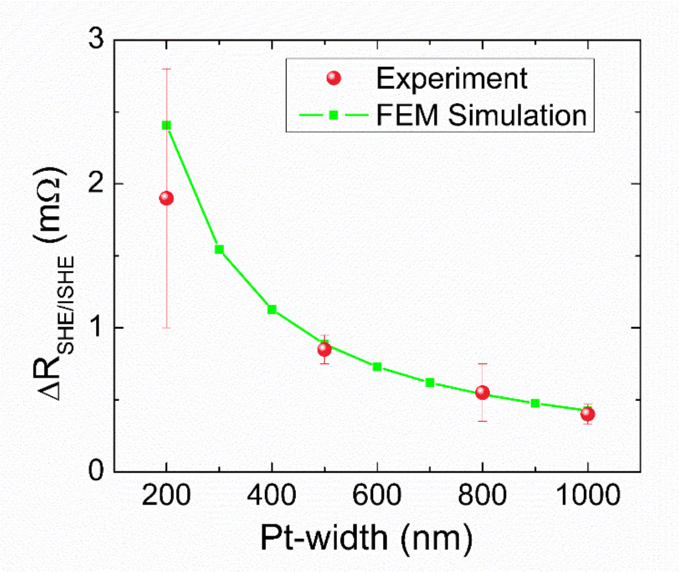

Fig. V. 5. *Simulation and experimental amplitudes of the of the spin signal vs. width of the Pt wire.*

Fig. V. 5 shows the experimental data and results of FEM simulations, with a plot of the variations of the spin signal amplitude as a function of the Pt width. The decrease of the spin signal amplitude according to the increase of the Pt width can be understood as the reduction of the resistance of the intersection volume as given in *eq. (B. 9)* with the gap $g = 0$ in the ISHE configuration, or the decrease of the spin current density in the case of the SHE configuration.

The parameters used for the simulations were either measured on patterned Hall crosses (ρ_{Pt} = 28.0 μΩcm, ρ_{NiFe} = 30.5 μΩcm, Θ_{EHE} (NiFe) = 0.32%), extracted from previous studies on lateral spin-valves (p_F = 0.26, λ_{NiFe} = 3.5 nm, and λ_{Pt} = 3.0 nm)[168,172]. The only free parameter is the spin Hall angle of Pt, Θ_{SHE}, so that by fitting the experimental data it is possible to extract its value (see in *Fig. V. 5*).

As in most experiments, the extracted value of Θ_{SHE} is strongly dependent on the supposed value of λ and the relevant parameter is rather $\Theta_{SHE}\ \lambda$.The obtained spin Hall angle is $\Theta_{SHE} = 7.5\%$, which gives a $\Theta_{SHE}\ \lambda$ value of 0.225 nm, in good agreement with recent works on Pt[135,168]. This value of the spin Hall angle is in good agreement with the results discuss in *Chapter II* and *Chapter III* for the case of NiFe/Pt (7.5%).

The device therefore provides an electrical way to detect the DWs, and can be employed as a conversion rate measurement technique, which can be useful for SOTs experiments. Let us note however that the nanofabrication process is more difficult than that of the devices shown in *Chapter II* and *Chapter III*.

V. 4. Conclusion

This device forms a new DW detection method, based on the ability for a domain wall to inject or detect a PSC in or from an adjacent SHE wire. It allows distinguishing between the head-to-head and the tail-to-tail configurations, and can be used to estimate the spin Hall angle of SHE materials but remains a complication in comparison to the SHE device shown in in *Chapters II, III,* and *IV*. This technique provides a new electrical way to study the DW motion, in a device akin to the Ferromagnetic/SHE bilayers typically used for spin-orbit torques experiments.

Spin orbit torque experiments could be performed by applying a current along the SHE wire, so that a PSC can be injected through the NiFe/Pt interface to the ferromagnetic nanowire[176,177,178,179]. For instance, a DC current or pulses could be applied, together with a small AC current to detect the DW motion.

GENERAL CONCLUSION AND PERSPECTIVES

General conclusion

This thesis focuses on the study of new electrical devices to characterize the SHE, and on the detection of magnetic DWs in nanowires using the direct and inverse SHE.

Chapter I: A general introduction to the physics presented in this manuscript has been given by describing basic concepts of spin dependent transport, and the state-of-the-art concerning SHE measurements.

Chapter II: This chapter presented a simple electrical device allowing the measurement of the spin-charge interconversion. The device was applied to study the bulk SHE/ISHE in Pt, with different materials of the ferromagnetic electrodes. The spin Hall angle and the spin diffusion length of Pt were extracted using FEM simulations.

Chapter III: The proposed nanostructure has been applied to characterize the SHE in different metals (Pd, Au, Ta, W, Ti) and Au-based alloys. The results are in relatively good agreement with what can be found in the literature, with in particular a negative spin Hall angle for W and a small spin Hall angle for Ta.

Chapter IV: The effective spin Hall angle of Pt, measured with the proposed technique and assuming that the interfaces are transparent, is found to depend on the nature of the ferromagnetic electrodes. Nanostructures using Co, CoFe and NiFe electrodes have been studied, as well as the influence of an additional Cu layer in-between the ferromagnetic and the Pt layers. The results seems to indicate that the Co/Pt and CoFe/Pt interfaces are rather transparent, but that the strong decrease of the conversion efficiency in NiFe/Pt could be due to the NiFe/Pt interface. In any case, this reminds that the measured effective spin Hall angle is a lower bound of the exact spin Hall angle.

Chapter V: A new DW detection method has been proposed, based on the ability for a ferromagnetic nanowire, in which a DW is pinned, to inject or detect pure spin currents.

The detection is based on the SHE in a F/N nanostructure, and provides an electrical way to study the DW motion, in a device here again akin to the ferromagnetic/SHE bilayers typically used for spin-orbit torques experiments.

During this thesis, I realized most of the clean room work, using the nanofabrication facilities of the PTA/CEA Grenoble (Plateforme Technologique Amont). I did almost all the fabrication steps, including the chemical process (resist test), SEM microscopy, e-beam evaporation, ion milling and the lift-off process. The e-beam lithography has been done by Laurent Vila.

I performed all the transport measurements, and analyzed the data with the help of Laurent Vila, Jean-Phillipe Attané, and Alain Marty. Concerning the simulation parts, I performed the FEM calculations, using the code developed by Alain Marty.

The work on the ferromagnetic/nonmagnetic nanostructures for the electrical measurement of the SHE which is presented in *Chapter II* and in part of *Chapter III* has been published in Nano Letters[168].

The work shown in *Chapter V* and concerning the electrical detection of magnetic domain walls by inverse and direct spin Hall effect has been published in *Appl. Phys. Lett.* **109**, 192401 (2016).

Several results have yet to be published:

- The results on interface effects shown in *Chapters IV*
- The results obtained on Au-based alloys
- Additional results on the probing of SHE using a single ferromagnetic electrode, which are not discussed in this manuscript

I also used the experimental skills developed during this PhD to contribute, as co-author, to several works which are not discussed in this manuscript:

- The comparison of the use of NiFe and CoFe as electrodes for metallic lateral spin-valves (G. Zahnd *et al. Nanotech.* **27**, 035201 (2015)*)*

- A study on the introduction and pinning of domain walls in 50 nm NiFe constrictions using local and external magnetic fields (G. Zahnd *et al. J. Magn. Magn. Matter.* **406**, 166-170 (2016))
- Another study on the use of domain walls to perform non-local measurements with high spin signal amplitudes (Savero Torres *et al.*, *Appl. Phys. Lett.* **109**, 042405 (2016))
- The demonstration of the control of the extrinsic SHE in Au-based alloys (P. Laczkowski *et al.*[154]).
- A study of the Hanle effect in GMR lateral structures (to be published)
- A study of the shift from CPP structures to lateral structures (to be published)
- A study of the measurement of spin diffusion lengths of CoFe, Co, NiFe, Pt and Ta using spin absorption in LSVs (to be published)
- A comparison of the transverse and longitudinal absorption in NiFe, Co and CoFe (to be published)

Perspectives

The detection technique of the spin-charge interconversion nanostructures presented in this thesis in *Chapters II, III, and IV* is a promising tool, that could be applied not only to the study of SHE and interface effects, but more generally to the spin-charge interconversion by SOC. It could be in particular adapted to the study of the Rashba effect in two dimension electron gas[81,128] or to the conversion at the surface states of topological insulators[148,149].

The physics involved at the F/N interface is also a promising field of application of this technique, the work presented in *Chapter IV* being only a preliminary work demonstrating the usefulness of the method.

The DW detection device proposed in *Chapter V* could be used to perform SOT experiments, while controlling the direction of the injected spins[65, 105, 163,180].

Annexes

A. Nanofabrication

The fabrication of the samples has been performed at the Plateforme Technologique Amont (PTA) in Grenoble, using the following process.

Resist deposition

The resist has been deposited on SiO_2 substrates and spin-coated at 4000 rpm, with an acceleration of 2000 rpm. After that, the sample with the resist is heated in order to remove the solvent. In the case of the polymethyl methacrylate (PMMR) resist, the sample has been heated at 180° Celsius for 2 minutes.

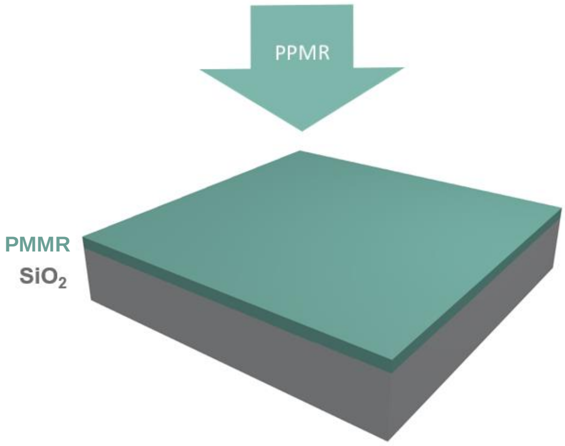

Fig. B 1 *Scheme of the PMMR resist deposition*

E-beam lithography

The electron-beam lithography has been performed in a Jeol 6300FS e-beam nano-writer using an acceleration voltage of 100 keV. In this nano-writer the exposure can be made using two modes: high speed, EOS3 (4th lens, with beam step size of 1nm and field size of 500 µm) and high resolution EOS6 (5th lens, with beam step size of 0.125 nm and field size of 62.5 nm). In this work, we mainly use the high speed mode with currents of 1 nA.

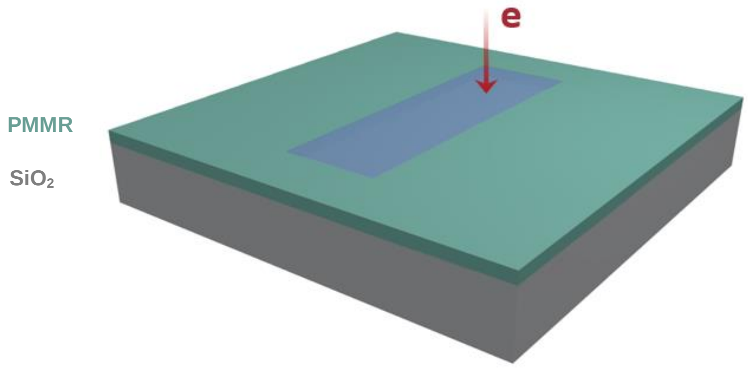

Fig. B 2 *E-beam lithography: the e-beam only acts on the PMMR area of the design.*

Developing process

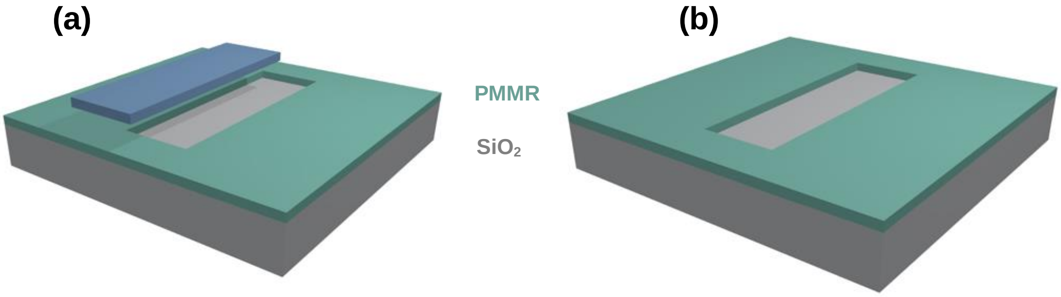

Fig. ***B*** **3** *Developing process: (a) the sample is developed in the MIBK solvent, to remove the PMMR resist in the irradiated area (b).*

Materials deposition

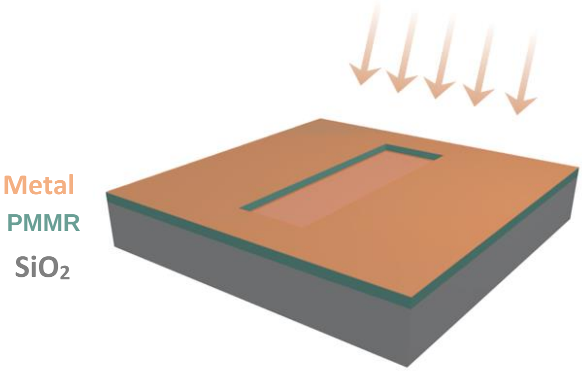

Fig. ***B*** **4** *Metal deposition on the sample surface.*

The deposition of the different materials has been done using a PLASSYS e-beam evaporator. In this machine the material deposition is performed at a pressure of around 0.5 x 10^{-7} mbar. The rate of material deposition is controlled using a quartz detector, within the range of 0.1 to 1 nm/s.

Lift-off process

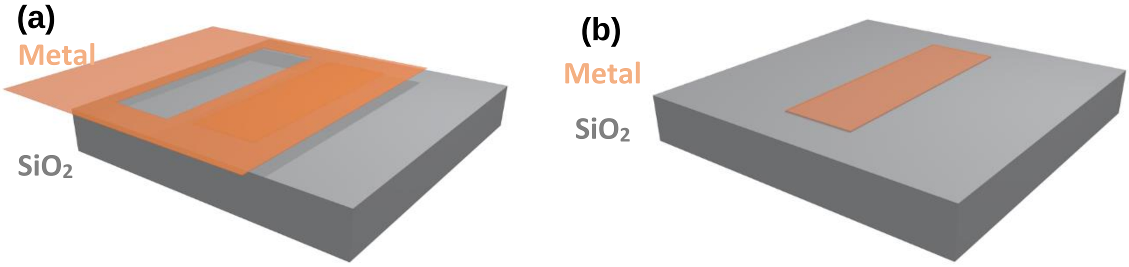

Fig. ***B*** **5** *Lift-off process: (a) the PMMR resist is removed by the acetone solvent and the metallic film above it is lifted off. Then (b), there remains the patterned nanowire.*

The lift-off process has been performed to remove the resist that was not insulated during the e-beam lithography, keeping only the metal in the zone that were insolated. It was done by inserting the deposited sample into the acetone and keeping it inside usually the whole night in order to assure the chemical reaction.

Ion-gun etching

The process was done in order to clean the surface prior to metal deposition. An Ar plasma etching has been used, with an acceleration voltage of 400V.

B. Analytical modelling and FEM simulations

1D model of the SHE contribution

An approach based on the diffusive model exposed in *Section I. 1* can be used to express the voltage obtained at the ends of the transversal SHE-wire, when a current flow through the magnetic wire. We assume that the vertical current density J_{cz} flowing locally through the ferromagnet/SHE interface gives rise locally to a spin accumulation profile in the ferromagnetic and normal sides. If one takes *z = 0* at the interface, the spin accumulation profile from (I. 6) is

$$\mu(z) = \frac{cosh\left(\frac{h_N+z}{\lambda_N}\right)}{cosh\left(\frac{h_N}{\lambda_N}\right)}\mu(0) \qquad \textit{in the SHE material (z<0)}$$

(B. 1)

$$\mu(z) = \frac{cosh\left(\frac{h_F-z}{\lambda_F}\right)}{cosh\left(\frac{h_F}{\lambda_F}\right)}\mu(0) \qquad \textit{in the ferromagnet (z>0)}$$

(B. 2)

Where μ, $h_{F/N}$, $\lambda_{F/N}$ are the spin accumulation, the thicknesses and the spin diffusion lengths, respectively. Subscripts F and N denote the ferromagnetic and SHE materials.

At the interface, which we assume to be transparent, the spin current is conserved so we can write:

$$-\frac{1}{\rho_F^*}\partial_Z\mu + p_F j_{cz} = -\frac{1}{\rho_N}\partial_z\mu$$

(B. 3)

where p_F is the polarization of the ferromagnet, j_{cz} is the charge current density flowing from the ferromagnetic material to the normal one along the Z direction, ρ is the resistivity of the material, and $\rho_F^* = \frac{\rho_F}{(1-p_F^2)}$ is the effective resistivity of the ferromagnetic materials.

Combining expressions (B. 1), (B. 2) and (B. 3) leads to the local spin accumulation at the interface.

$$\mu(0) = \frac{p_F j_{cz}}{\frac{1}{\rho_N \lambda_N} tanh\left({}^{h_N}/_{\lambda_N}\right) + \frac{1}{\rho_F^* \lambda_F} tanh\left({}^{h_F}/_{\lambda_F}\right)}$$

(B. 4)

Locally the transverse current density j_{cy}, generated through the SHE effect by the vertical spin current density is

$$j_{cy} \ = \ \Theta_{SHE} j_{sz} \ = \ -\Theta_{SHE} \frac{\partial_z \mu}{\rho_N}$$

(B. 5)

The integration of this current density over the section of the SHE wire gives the transverse current generated by ISHE:

$$I_{cy} \ = \iint_{-h_N}^{0} J_{cy} dxdz = \Theta_{SHE} \frac{1}{\rho_N} \int \big(\mu(0) - \mu(-h_N)\big)\, dx$$

(B. 6)

Using (B. 5) and (B. 4), we obtain:

$$I_{cy} = \Theta_{SHE} p_F \frac{\frac{1}{\rho_N}\left(1 - \frac{1}{cosh\left({}^{h_N}/_{\lambda_N}\right)}\right)}{\frac{1}{\rho_N \lambda_N} tanh\left({}^{h_N}/_{\lambda_N}\right) \ + \ \frac{1}{\rho_F^* \lambda_F} tanh\left({}^{h_F}/_{\lambda_F}\right)} \int j_{cz} dx$$

(B. 7)

The integral can be written$\int j_{cz} dx = 2I/w_F$. The factor 2 appears here because the current gets out from one electrode, and gets into the other one.

$$I_{cy} = 2\Theta_{SHE} p_F \frac{\lambda_N}{w_F} \frac{\frac{1}{\rho_N \lambda_N}\left(1-\frac{1}{cosh\left({}^{h_N}/_{\lambda_N}\right)}\right)}{\frac{1}{\rho_N \lambda_N} tanh\left({}^{h_N}/_{\lambda_N}\right)+\frac{1}{\rho_F^* \lambda_F} tanh\left({}^{h_F}/_{\lambda_F}\right)} I$$

(B. 8)

Within the open circuit condition for the channel, and with the approximation of the backflow resistance R_{backflow} being due that of the parallel F and N materials, the transverse induced voltage can be written as:

$$\Delta V_y = R_{backflow} I_{cy} = \frac{I_{cy} w_F}{\left(\frac{h_N}{\rho_N} + \frac{h_F}{\rho_F}\right) w_N - \frac{h_F}{\rho_F} g}$$

(B. 9)

Finally,

$$\Delta R_{SHE/ISHE} = \frac{\Delta V_y}{I} = \frac{2 p_F \Theta_{SHE} \lambda_N}{\left(\left(\frac{h_N}{\rho_N} + \frac{h_F}{\rho_F}\right) w_N - \frac{h_F}{\rho_F} g\right)} \frac{\frac{1}{\rho_N \lambda_N}\left(1 - \frac{1}{cosh\left({}^{h_N}/_{\lambda_N}\right)}\right)}{\frac{1}{\rho_N \lambda_N} tanh\left({}^{h_N}/_{\lambda_N}\right) + \frac{1}{\rho_F^* \lambda_F} tanh\left({}^{h_F}/_{\lambda_F}\right)}$$

(B. 10)

This is the results presented in equation (II. 2) in *Chapter II* .

1D analytical model of the EHE contribution

In the following, we show that is also possible to develop a crude 1D analytical model to calculate the EHE contribution. The origin of this contribution is illustrated in *Fig. B. 1.* Basically, the charge current within the ferromagnetic electrodes possesses a component along the z direction. The EHE leads to the appearance of electrical fields along the Y axis. These electrical fields somehow add up in the antiparallel configuration *Fig. B. 1a*, and cancel out when the magnetizations are parallel *Fig. B. 1b*. The charge current density due to the EHE is given by

$$\boldsymbol{j}_{EHE} = \Theta_{EHE} \boldsymbol{j_c} \times \boldsymbol{m}$$

(B. 11)

where **m**, θ_{EHE}, $\mathbf{j_c}$, and $\mathbf{j_{EHE}}$ are the magnetization unit vector, the EHE angle, the applied charge current density and the EHE charge current density, respectively.

Far away in the ferromagnetic wire, the current lines are homogeneously spread and parallel to the Y axis. Above the interface, the current lines dive from the ferromagnet to the SHE material, leading to a component of the current density along the z direction j_{Cz}. The magnetization is along the X direction, so only j_{Cz} contributes to the EHE. This current density component is equal to zero at the top surface, and varies approximately linearly with z. For the left electrode, for instance, it can be written

$$j_{Cz} = \frac{I}{w_F L_F}\left(\frac{z - h_F}{h_F}\right)$$

(B. 12)

where $L_F = (w_N - g)/2$, and with

$$j_{EHE,y} = \Theta_{EHE} j_{Cz}$$

(B. 13)

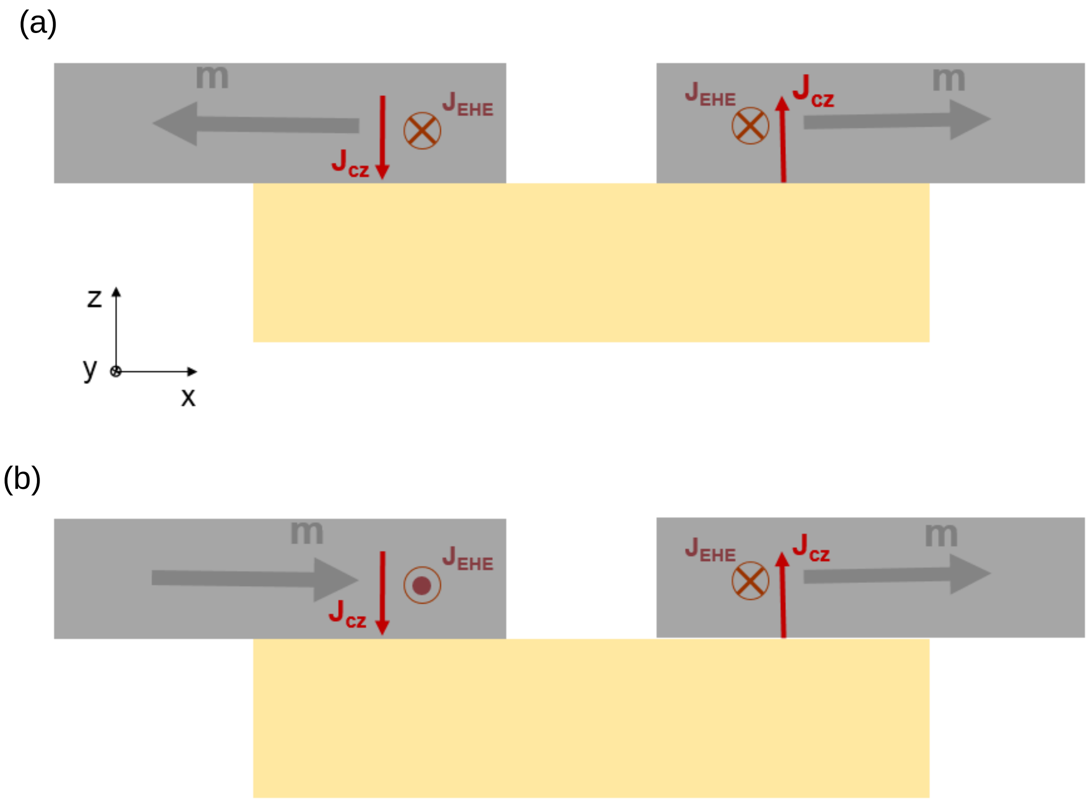

Fig. B. 1. *Origin of the EHE contribution in the ISHE measuring configuration. The EHE contributions of the electrodes add up in the antiparallel magnetization configuration (a) and cancel out in the parallel magnetization configuration (b).*

$$I_{EHE} = 2\int_{0}^{h_F} j_{EHE}(z)\, L_F dz \; = \Theta_{EHE} I \,\frac{h_F}{w_F}$$

(B. 14)

Finally, the detected voltage is:

$$V_{EHE} = R_{backflow} I_{EHE} = \Theta_{EHE} I \,\frac{h_F}{\left(\frac{h_N}{\rho_N} + \frac{h_F}{\rho_F}\right) w_N - \frac{h_F}{\rho_F}\, g}$$

(B. 15)

where $R_{backflow}$ is given by eq. (B. 9).

Note that the comparison with 3D simulations shows that this rough 1D model tends to overestimate the EHE contribution when the resistivity of the SHE channel is large, and has therefore to be used cautiously. Indeed, this 1D modeling does not take into account the lateral spread of the current lines in the part of the channel not covered by the ferromagnetic wire.

FEM simulation

The FEM simulations were carried out within the framework of a 2 spin-current drift diffusion model[173], with collinear magnetization of the electrodes along the easy axis of the ferromagnetic wires. For a magnetization axis along X, the current densities for spin up and spin down electrons can be written:

$$\vec{J}_{\uparrow/\downarrow} = -\begin{pmatrix} 1 & 0 & 0 \\ 0 & 1 & \pm\Theta_{SHE} \\ 0 & \mp\Theta_{SHE} & 1 \end{pmatrix} \frac{1 \pm p}{2\rho_N} \vec{\nabla}\mu_{\uparrow/\downarrow}$$

(B. 16)

$$\vec{J}_c = \vec{J}_\uparrow + \vec{J}_\downarrow$$

(B. 17)

where $\vec{J}_{\uparrow/\downarrow}$ and $\mu_{\uparrow/\downarrow}$ are the current densities and electrochemical potentials of spin up and down electrons, respectively. Equations *(B. 16)* and *(B. 17*) imply that in the ferromagnet the extraordinary Hall angle is $\Theta_{EHE} = p_F \Theta_{\mathrm{SHE}}^{\mathrm{F}}$, where $\Theta_{\mathrm{SHE}}^{\mathrm{F}}$ is the spin Hall angle of the ferromagnetic materials. In the SHE material, the polarization in *eq. (B. 16)* is zero.

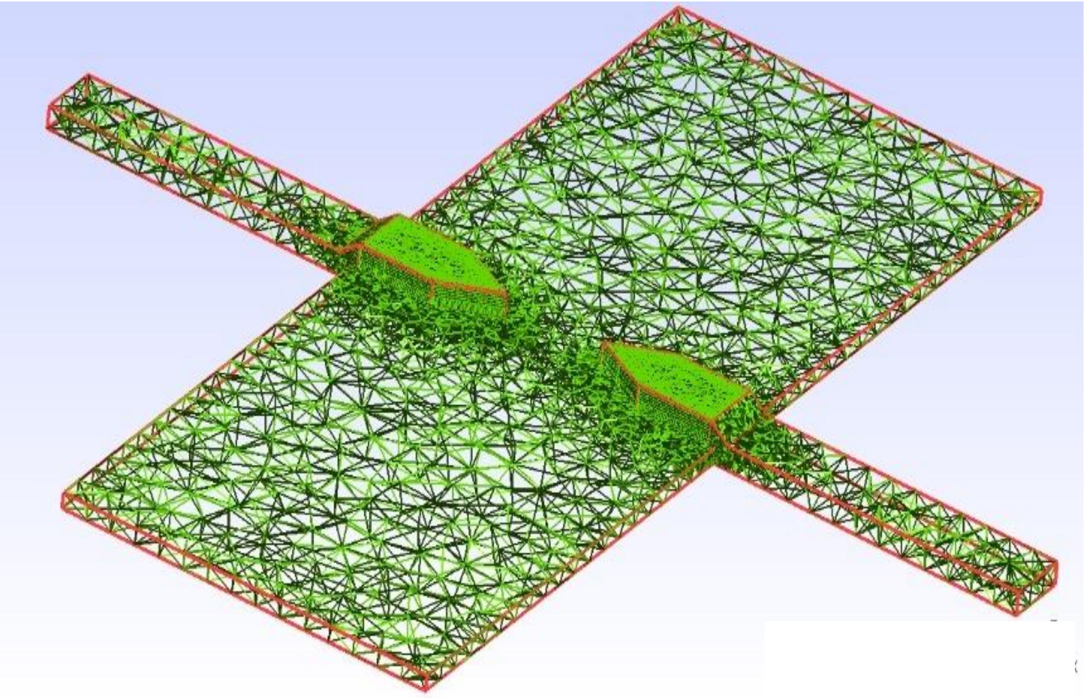

Fig. B 6. 3D-mesh for the FEM calculation of the SHE devices shown in Chapter II

Apart from the non-etched lateral edges of the SHE wire, the ferromagnet/normal metal interfaces are assumed to be transparent, without spin memory loss (*i.e.*, the probability of spin flip events at the interface is null), and thus the electrochemical potentials are continuous along the entire device. The boundary conditions are of Neumann type, and account for the current imposed to the device at the contact interfaces. The simulations were done using the free softwares *GMSH*[174] for geometry construction, mesh generation and post-processing, and with the associated solver *GETDP*[175]. The wires and the channel were taken long enough (*i.e.*, more than 3 times the spin diffusion length in the considered material, and much larger than the nanowire widths) so that the spin accumulation vanishes at their ends.

In the 3D FEM simulations, the polarization and the spin diffusion length of the ferromagnetic materials are taken from the literature and our own results on electrical transport in lateral spin-valves. The spin diffusion lengths of the SHE materials are either measured (Pt) or taken from the literature. The resistivities and the EHE have been measured directly on hall crosses patterned close to the devices, so that finally the only free parameter of the FEM simulations is the spin Hall angle. The extracted spin Hall angle is the value that reproduces the observed spin signal amplitude.

C. Electrical measurements

The resistance measurements were performed using a *Lock-in Amplifier*, with an applied AC current of 100 or 200 µA and a frequency f_o in the range *300-750 Hz*.

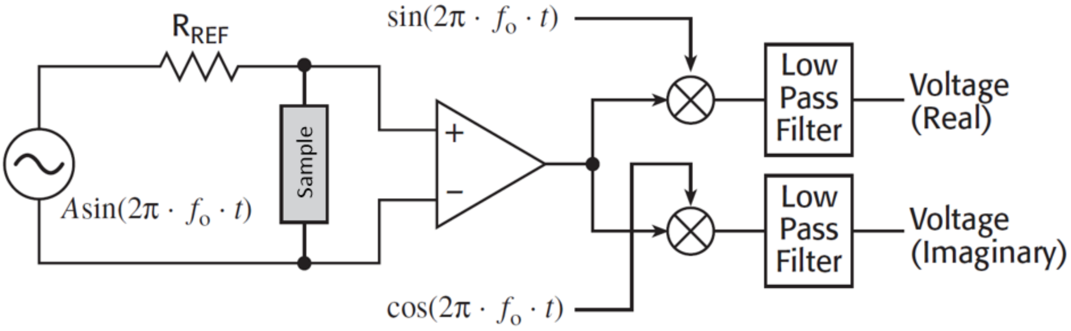

***Fig. C. 1**. Block diagram of a lock-in amplifier measurement setup.*

Fig. C. 2 plots the block diagram of the resistance measurements using a *Lock-in Amplifier*. The sample is introduced by a cable to a chamber of the electromagnets in which a uniform field is produced. The detected voltage is read by a PC whose LabVIEW-programs can record and analyze the data.

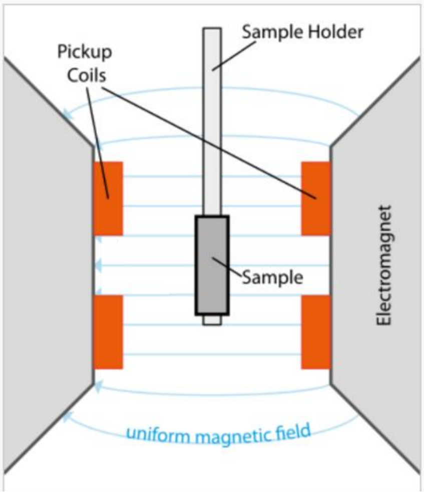

Fig. ***C. 2***. *Sample in the field created by the electromagnet*

D. Resumé en Français

La spin-orbitronique est basée sur l’utilisation de l’interaction spin-orbite pour réaliser la conversion directe ou inverse de courants de charge en courants de spin. L’évaluation de l’efficacité de cette conversion est un problème central : le besoin de développer des méthodes de mesure directes de cette conversion apparaît aujourd’hui comme l’un des défis majeurs de l’électronique de spin.

Cette thèse porte sur l’étude d’une nouvelle nanostructure permettant de caractériser l’effet Hall de spin, et sur la détection de parois magnétiques dans des nanofils par effet Hall de spin direct et inverse. Nous allons ici en résumer les principaux résultats.

Il existe différentes façons de détecter la conversion de courants de charge en courants de spin, les méthodes les plus utilisées étant optiques ou basées sur la résonance ferromagnétique. Des efforts importants ont été fournis afin de développer des méthodes purement électriques, non seulement par souci de simplicité, mais également parce que l’objectif à long terme est d’intégrer les effets spin-orbite dans des dispositifs spintroniques.

Certaines méthodes électriques, telles que la double barre de Hall en forme de H, sont limitées aux matériaux à grandes longueurs de diffusion de spin, comme les semiconducteurs, qui possèdent en général de faibles taux de conversion.

L’insertion de matériaux spin-orbite dans des vannes de spin latérales permet également d’observer la conversion dans des systèmes à large couplage spin-orbite, comme des métaux lourds ou des interfaces Rashba. Ceci étant, les nanodispositifs sont complexes : un canal non magnétique est requis pour réaliser le transfert de spins de la source vers le détecteur, ce qui multiplie les interfaces et rend délicate l’interprétation des données.

Dans ce manuscrit, nous proposons une méthode simple de mesure de la conversion directe et inverse dans un matériau à effet Hall de spin, en utilisant un système proche des bicouches ferromagnétique/non-magnétique utilisées dans la plupart des expériences portant sur l’étude des couples spin-orbites.

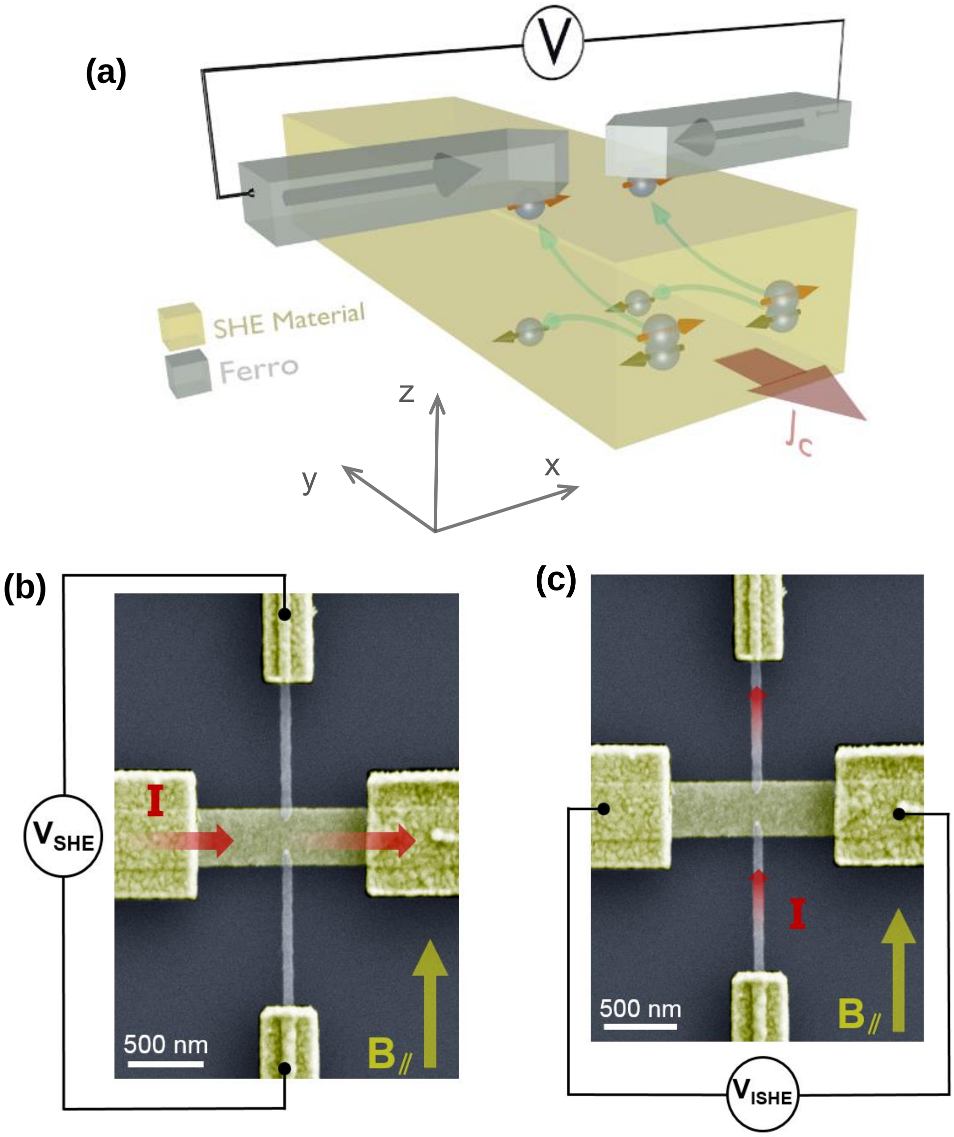

Fig. 10. *Principe de la mesure: (a) schéma de la nanostructure. Deux électrodes ferromagnétiques sont connectées à la surface d'une nanopiste à effet Hall de spin. Les flèches noires représentent la direction d'aimantation des électrodes ferromagnétiques. Un courant de charge* J_C *est envoyé le long de la nanopiste à effet Hall de spin, générant un courant de spin dans la direction Z. Une accumulation de spin apparaît ainsi à la surface de la nanopiste, qui peut être sondée par les électrodes ferromagnétiques. Configuration de mesure de l'effet Hall de spin (b) direct et (c) inverse.*

La nanostructure proposée est présentée sur la *Fig.1a*, et consiste en une nanopiste de matériau à effet Hall de spin connectée à deux électrodes ferromagnétiques transverses. Deux méthodes de détection peuvent être utilisées (cf. Figs. 1b et 1c), correspondant à la mesure de l'effet Hall de spin direct ou inverse.

Un exemple de signal de spin obtenu est donné dans la *Fig. 2a*, en utilisant une nanopiste de Pt et des électrodes de $Co_{60}Fe_{40}$. Le ratio R_{SHE} entre la tension mesurée et le courant appliqué est mesuré en fonction du champ magnétique appliqué dans la direction X, les variations du signal de spin étant dues aux renversements des électrodes.

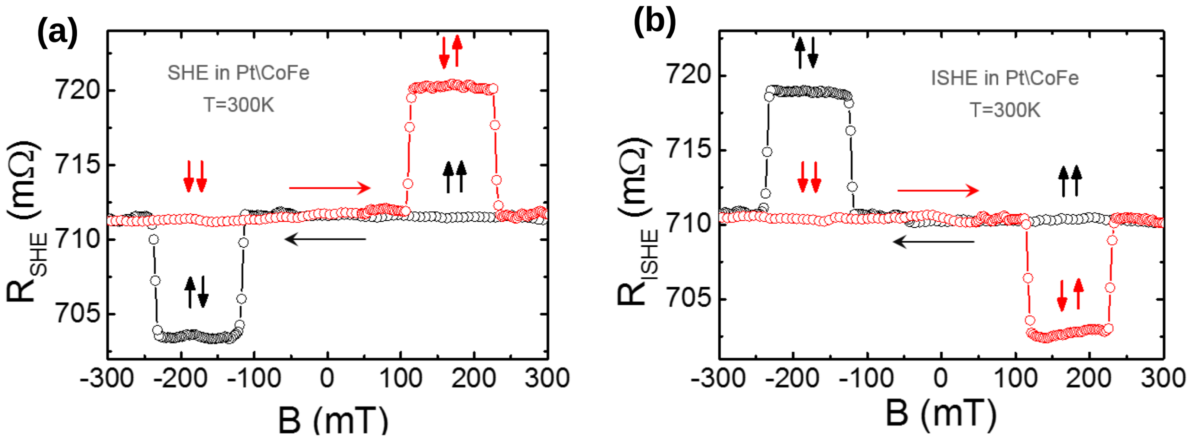

***Fig. 11.* Observation de l'effet Hall de spin direct et inverse:** *Exemples de signauxobtenus dans une nanostructure Pt\CoFe*

Ces signaux peuvent être reproduits par simulation, en prenant en compte à la fois l'effet Hall de spin et l'effet Hall extraordinaire. Ces simulations permettent d'extraire la valeur de l'angle de Hall de spin effectif du Pt, et si une dépendance en épaisseur est réalisée, la valeur de la longueur de diffusion de spin. Les comportements observés sont bien reproduits à la fois par ces simulations et par des modèles analytiques 1D.

Ce type de structure devrait en principe être applicable pour étudier la conversion de courants de spin en courants de charge par effet spin-orbite dans d'autres matériaux tels que des semiconducteurs, des oxydes, des gaz 2D d'électrons, ou des isolants topologiques.

Nous avons utilisé cette méthode pour mesurer l'angle de Hall de spin effectif de différents métaux (Pd, Au, Ta, Ti and W) et alliages (AuTa et AuW). Les résultats les plus importants sont résumés dans la table ci-dessous.

System	**λ_F (nm)**	**λ_N (nm)**	**ρ_F (µΩ.cm)**	**ρ_N (µΩ.cm)**	**p_F**	**Θ_{EHE} (%)**	**Θ_{SHE} (3D-FEM) (%)**
NiFe/Pt	3.5 ± 0.5	3.0 ± 0.6	30	28	0.28	0.32	7.5 ± 0.5
CoFe/Pt	3.5 ± 0.5	3.0 ± 0.6	20.5	28	0.58	0.63	19 ± 0.5
CoFe/Pd	3.5 ± 0.5	13[132]	20.5	21	0.58	0.63	4.5 ± 0.5
CoFe/Au	3.5 ± 0.5	35[136]	20.5	4.2	0.58	0.63	1.5 ± 0.3
CoFe/Ta	3.5 ± 0.5	1.8[151]	20.5	200	0.58	0.63	-2.7 ± 3.0
CoFe/W	3.5 ± 0.5	1.4[150]	20.5	135	0.58	0.63	-6.5 ± 1.0
CoFe/Ti	3.5 ± 0.5	13[152]	20.5	52	0.58	0.63	≈ 0

Les résultats sont qualitativement en accord avec ce qui était attendu au regard de la littérature existante. Le point le plus remarquable est sans doute la mesure d'un fort angle de Hall de spin pour Pt.

Un autre élément intéressant est la mesure d'angles différents lorsque la nature des électrodes change. La valeur effective de l'angle de Hall de spin du Pt a été mesurée en utilisant des électrodes de CoFe, Co, et NiFe, et en insérant éventuellement une couche de Cu entre les différentes couches ferromagnétiques et la couche de Pt. Les différences observées montrent que les interfaces jouent un rôle très important dans l'analyse quantitative de l'effet et que la mesure ne donne qu'un angle de Hall de spin effectif, limite inférieure de l'angle de Hall de spin réel. Dans certains échantillons, l'angle de Hall effectif du Pt atteint 27%. Il semble que l'interface NiFe/Pt soit, dans ce contexte, de relativement mauvaise qualité.

Enfin, nous avons montré que si l'effet Hall de spin est susceptible de générer des couples spin-orbite sur une paroi de domaine, il est également possible d'utiliser l'effet hall de spin ou l'effet Hall de spin inverse pour détecter la présence d'une paroi magnétique. Une paroi dans un nanofil peut en effet être utilisée pour injecter un pur courant de spin dans un nanofil de Pt adjacent. Ce pur courant de spin est alors transformé en un courant par effet Hall de spin inverse, ce qui permet de détecter la présence de la paroi (*cf. Fig. 3*).

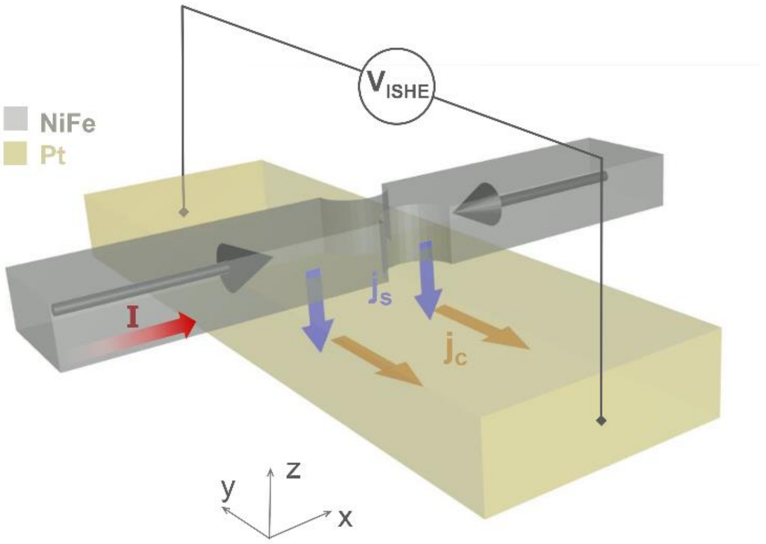

Figure 3. *Schéma de la nanostructure permettant la détection d'une paroi. Les flèches noires représentent la direction de l'aimantation lorsqu'une paroi est piégée. Un courant est appliqué le long du fil ferromagnétique, créant un courant de spin dans la direction Z, converti par effet Hall de spin inverse en un courant de charge le long du fil de Pt.*

Cette nanostructure permet la détection par effet Hall de spin direct ou inverse, et la mesure de l'angle de Hall de spin par comparaison avec des simulations. Notons enfin que le système utilisé est là encore très proche de ceux utilisés pour les études de couples spin-orbite.

Ces travaux ont donné lieu à publication dans Nano Letters et Applied Physics Letters. Les résultats concernant les effets d'interface, les alliages à base d'Au, et certains résultats sur les dispositifs de mesure sont en cours de publication. Au-delà, et grâce aux techniques développées durant cette thèse, l'auteur de ce manuscrit a contribué comme co-auteur à huit études publiées ou en cours de publication.

Bibliography

---

[1] Abragam, Anatole. *The principles of nuclear magnetism*. No. 32. Oxford university press, 1961.

[2] S. Maekawa and T. Shinjo (eds) Spin Dependent Transport in Magnetic Nanostructures (London: Taylor and Francis) (2002).

[3] I. Žutić, J. Fabian, and S. D. Sarma. Spintronics: Fundamentals and applications. *Rev. Mod. Phys.* **76**, 323 (2004).

[4] S. A., Wolf, D. D. Awschalom, R. A. Buhrman, J. M. Daughton, S. Von Molnar, M. L. Roukes, A. Yu Chtchelkanova, and D. M. Treger. Spintronics: a spin-based electronics vision for the future. *Science* **294**, 1488-1495 (2001).

[5] Thomson, William. On the electro-dynamic qualities of metals: effects of magnetization on the electric conductivity of nickel and of iron. *Proceedings of the Royal Society of London* **8**, 546-550 (1856).

[6] T. McGuire, and R. L. Potter. Anisotropic magnetoresistance in ferromagnetic 3d alloys. *IEEE Trans. Magn.* **11**, 1018-1038 (1975).

[7] B. Dieny et al. Giant magnetoresistance in soft ferromagnetic multilayers. *Phys. Rev. B* **43**, 1297(1991).

[8] Z. Wang, and R. H. Victora. Enhancement of giant magnetoresistance and oscillation by wave-vector filtering in Fe/Ag/Fe/InAs/Ag. *Phys. Rev. B* **94**, no. 24 (2016): 245415.

[9] Julliere, Michel. Tunneling between ferromagnetic films. *Phys. Lett. A* **54**, 225-226 (1975).

[10] J. S. Moodera, L. R. Kinder, T. M. Wong, and R. Meservey. Large magnetoresistance at room temperature in ferromagnetic thin film tunnel junctions. Phys. Rev. Lett. **74**, 3273 (1995).

[11] S. Ikeda, J. Hayakawa, Y. Ashizawa, Y. M. Lee, K. Miura, H. Hasegawa, M. Tsunoda, F. Matsukura, and H. Ohno. Tunnel magnetoresistance of 604% at 300 K by suppression of Ta diffusion in CoFeB∕MgO∕CoFeB pseudo-spin-valves annealed at high temperature. *Appl. Phys. Lett.* **93**, 082508 (2008).

[12] C. Chapper, A. Fert, and F. Nguyen Van Dau. The emergence of spin electronics in data storage. *Nat. Mater.* **6**, 813 (2007).

[13] Zhao, Weisheng, and Guillaume Prenat, eds. *Spintronics-based computing*. Springer, 2015.

[14] N. F. Mott. The electrical conductivity of transition metals. *Proceedings of the Royal Society of London A: Mathematical, Physical and Engineering Sciences*. *Roy. Soc.* **153**, 880 (1936).

[15] A. Fert and I. A. Campbell. Two-current conduction in nickel. *Phys. Rev. Lett.* **21**, 1190–1192 (1968).

[16] A. Fert and I. Campbell. Electrical resistivity of ferromagnetic nickel and iron based alloys. *J. Phys. F* **6**, 849–871 (1976).

[17] T. Valet and A. Fert. Theory of the perpendicular magnetoresistance in magnetic multilayers. *Phys. Rev. B* **48**, 7099 (1993).

[18] S. Takahashi, and S. Maekawa. Spin injection and detection in magnetic nanostructures. *Phys. Rev. B* **67**, 052409 (2003).

[19] S. Y. Garzon. Spin injection and detection in copper spin valve structures. PhD thesis, University of Maryland (College Park, Md.), 2005.

[20] Tai L. Chow (2006). Electromagnetic theory. Sudbury MA: Jones and Bartlett. p. Chapter 10.21; p. 402–403 ff. ISBN 0-7637-3827-1.

[21] L. Föppl and P. J. Daniell, Zur Kinematik des Born'schen starren Körpers, Nachrichten von der Königlichen Gesellschaft der Wissenschaften zu Göttingen, 519 (1913)

[22] Sakurai, J. J. In Tuan, SF, Ed.; Modern Quantum Mechanics, Revised Edition. Reading: Addison-Wesley Publishing Company, Inc, 1994 (Chapter 5).

[23] M. Vijayakumar, and M. S. Gopinathan. Spin-orbit coupling constants of transition metal atoms and ions in density functional theory. *Journal of Molecular Structure: THEOCHEM* **361**, 15-19 (1996).

[24] G. Dresselhaus. Spin-orbit coupling effects in zinc blende structures. *Phys. Rev.* **100**, 580 (1955).

[25] F. T. Vas’ko, Spin splitting in the spectrum of two-dimensional electrons due to surface potential. *JETP Lett.* **30**, 541–544 (1979).

[26] Y. Bychkov and E. Rashba, Oscillatory effects and the magnetic susceptibility of carriers in inversion layers. *J. Phys. C* **17**, 6039–6045 (1984).

[27] M. I. Dyakonov and V. I. Perel, Possibilty of orienting electron spins with current, *Sov. Phys. JETP Lett.* **13**, 467 (1971).

[28] M. I. Dyakonov and V. I. Pere. Current-induced spin orientation of electrons in semiconductors. *Phys. Lett. A* **35**, 459-460 (1971).

[29] A. A. Bakun, B. P. Zakharchenya, A. A. Rogachev, M. N. Tkachuk, and V. G. Fleisher. Observation of a surface photocurrent caused by optical orientation of electrons in a semiconductor. *Sov. Phys. JETP Lett.* **40**, 1293 (1984).

[30] M. I. D’yakonov and V. I. Perel. Spin orientation of electrons associated with the interband absorption of light in semiconductors. *Sov. Phys. JETP* **44**, 1252 (1971).

[31] M. I. D’yakonov and V. I. Perel’. Spin relaxation of conduction electrons in noncentrosymetric semiconductors. *Sov. Phys. Solid State* **13**, 3023 (1972).

[32] R. Karplus and J. M. Luttinger. Hall effect in ferromagnetics. *Phys. Rev.* **95**, 1154 (1954).

[33] E. H. Hall. On the rotational coefficient in nickel and cobalt. *Philos. Mag.* **12**, 157 (1881).

[34] N. Nagaosa, J. Sinova, S. Onoda, A. H. MacDonald and N.P. Ong. Anomalous hall effect. *Revi. Mod. Phys.* **82**, 1539 (2010).

[35] M. I. Dyakonov and A.V. Khaetskii. Spin Hall effect, in Spin Physics in Semiconductors, ser. in Solid-State Sciences, M. I. Dyakonov, Ed. New York: Springer, **157**, ch. 8, pp. 211–243 (2008); https://arxiv.org/ftp/arxiv/papers/1210/1210.3200.pdf

[36] M. I. Dyakonov. Magnetoresistance due to edge spin accumulation. *Phys. Rev. Lett*. **99**, 126601 (2007).

[37] A. Hoffmann. Spin Hall effects in metals. *IEEE Trans. Magn*. **49**, 5172-5193 (2013).

[38] J. Smit. The spontaneous Hall effect in ferromagnetics ii. *Physica* **24**, 39 (1958).

[39] L. Berger. Side-jump mechanism for the Hall effect in ferromagnets. *Phys. Rev. B* **2**, 4559 (1970).

[40] Y. Niimi and Y. Otani. Reciprocal spin Hall effects in conductors with strong spin orbit coupling: a review. Reports on Progress in Physics **78**, 124501 (2015).

[41] N. F. Mott and H. S. Massey. The Theory of Atomic Collisions. Oxford: Clarendon Press, 1965.

[42] A. Fert, A. Friederich, and A. Hamzic. Hall effect in dilute magnetic alloys. *J. Magn. Magn. Mater.* **24**, 231-257(1981).

[43] A. Fert and P. M. Levy. Spin Hall effect induced by resonant scattering on impurities in metals. *Phys. Rev. Lett.* **106**, 157208 (2011).

[44] Y. Tian, L. Ye, and X.-F. Jin. Proper scaling of the anomalous Hall effect, *Phys. Rev. Lett.* **103**, 087206 (2009).

[45] G. Y. Guo, S. Murakami, T.-W. Chen, and N. Nagaosa. Intrinsic spin Hall effect in platinum: first-principles calculations. *Phys. Rev. Lett*. **100**, 096401 (2008).

[46] T. Tanaka, H. Kontani, M. Naito, T. Naito, D. S. Hirashima, K. Yamada, and J. Inoue. Intrinsic spin hall effect and orbital Hall effect in 4 d and 5 d transition metals. *Phys. Rev. B* **77**, 1651172008.

[47] S. Zhang, P. M. Levy, and A. Fert. Mechanisms of spin-polarized current-driven magnetization switching. *Phys. Rev. Lett.* **88**, 236601 (2002).

[48] A. Brataas, A. D. Kent, and H. Ohno. Current-induced torques in magnetic materials. *Nat. Mater.* **11**, 372-381 (2012).

[49] A. Shpiro, P. M. Levy, and S. Zhang. Self-consistent treatment of nonequilibrium spin torques in magnetic multilayers. *Phys. Rev. B* **67**, 104430(2003).

[50] M. Hosomi, H. Yamagishi, T. Yamamoto, K. Bessho, Y. Higo, K. Yamane, H. Yamada *et al.* Novel nonvolatile memory with spin torque transfer magnetization switching: spin-ram. IEDM Tech. Dig. 459–462 (2005).

[51] Y. Huai. Spin-transfer torque MRAM (STT-MRAM): Challenges and prospects. *AAPPS Bulletin* **18**, 33-40(2008).

[52] C. J. Lin, S. H. Kang, Y. J. Wang, K. Lee, X. Zhu, W. C. Chen, X. Li et al. 45nm low power CMOS logic compatible embedded STT MRAM utilizing a reverse-connection 1T/1MTJ cell. In *2009 IEEE International Electron Devices Meeting (IEDM)*, pp. 1-4. IEEE, 2009.

[53] Y. Acremann, J. P. Strachan, V. Chembrolu, S. D. Andrews, T. Tyliszczak, J. A. Katine, M. J. Carey, B. M. Clemens, H. C. Siegmann, and J. Stöhr. Time-resolved imaging of spin transfer switching: beyond the macrospin concept. *Phys. Rev. Lett.* **96**, 217202 (2006).

[54] Y.Zhang, W. Zhao, Y.Lakys, J.-O. Klein, J.-V. Kim, D. Ravelosona, and C. Chappert. Compact modeling of perpendicular-anisotropy CoFeB/MgO magnetic tunnel junctions. *IEEE Transactions on Electron Devices* **59**, 819-826(2012).

[55] B. Dieny, R. C. Sousa, J. Herault, C. Papusoi, G. Prenat, U. Ebels, D. Houssameddine *et al.* Spin-transfer effect and its use in spintronic components. *International Journal of Nanotechnology* **7**, 591-614 (2010).

[56] S. Zhang, and Z. Li. Roles of nonequilibrium conduction electrons on the magnetization dynamics of ferromagnets. *Phys.Rev.Lett.* **93**, 127204 (2004).

[57] J. Grollier, P. Boulenc, V. Cros, A. Hamzić, A. Vaures, A.t Fert, and G. Faini. Switching a spin valve back and forth by current-induced domain wall motion. *App. Phys. Lett.* **83**, 509-511(2003).

[58] G. S. D. Beach, M. Tsoi, and J. L. Erskine. Current-induced domain wall motion. *J. Magn. Magn. Mater.* **320**, 1272-1281 (2008).

[59] A. Thiaville, Y. Nakatani, J. Miltat, and Y. Suzuki. Micromagnetic understanding of current-driven domain wall motion in patterned nanowires. *Europhys. Lett.* **69**, 990 (2005).

[60] D. Ravelosona, D. Lacour, J. A. Katine, B. D. Terris, and C. Chappert. Nanometer scale observation of high efficiency thermally assisted current-driven domain wall depinning. *Phys. Rev. Lett.* **95**, 117203 (2005).

[61] G. S. D. Beach *et al.* Dynamics offield-driven domain-wall propagation in ferromagnetic nanowires. *Nat. Mater.* **4**, 741–744 (2005); Hayashi *at al.* Influence of current on field-driven domain wall motion in permalloy nanowires from time resolved

measurements of anisotropic magnetoresistance. *Phys. Rev. Lett.* **96**, 197207(2006); Lepadatu *et al.* Experimental determination of spin-transfer torque nonadiabaticity parameter and spin polarization in permalloy. *Phys. Rev. B* **79**, 094402(2009).

[62] C. Chappert, A. Fert, and F. Nguyen Van Dau. The emergence of spin electronics in data storage. *Nat. Mater.* **6**, 813-823 (2007).

[63] S. Fukami, T. Suzuki, K. Nagahara, N. Ohshima, Y. Ozaki, Saito, S., ... and C. Igarashi, (2009, June). Low-current perpendicular domain wall motion cell for scalable high-speed MRAM. In *2009 Symposium on VLSI Technology*.

[64] D. A. Allwood, G. Xiong, C. C. Faulkner, D. Atkinson, D. Petit, and R. P. Cowburn. Magnetic domain-wall logic. *Science* **309**, 1688-1692(2005).

[65] I. M. Miron, G. Gaudin, S. Auffret, B. Rodmacq, A. Schuhl, S. Pizzini, J. Vogel, and P. Gambardella. Current-driven spin torque induced by the Rashba effect in a ferromagnetic metal layer. *Nat. Mater.* **9**, 230-234(2010).

[66] K. Garello, I. M. Miron, C. O. Avci, F. Freimuth, Y. Mokrousov, S. Blügel, S. Auffret, O. Boulle, G. Gaudin, P. Gambardella, Symmetry and magnitude of spin-orbit torques in ferromagnetic heterostructures. *Nat. Nanotech*. **8**, 587-593 (2013).

[67] G. Yu, P. Upadhyaya, Y. Fan, J. G. Alzate, W. Jiang, K. L. Wong, S. Takei *et al.* Switching of perpendicular magnetization by spin-orbit torques in the absence of external magnetic fields. *Nat. Nanotech.* **9**, 548-554 (2014).

[68] K.-S. Ryu, L. Thomas, S.-H. Yang, and S. Parkin. Chiral spin torque at magnetic domain walls. *Nat. Nanotech.* **8**, 527-533 (2013).

[69] A. J. Berger, E. RJ Edwards, H. T. Nembach, J. M. Shaw, A. D. Karenowska, M. Weiler, and T. J. Silva. Evidence for a common origin of spin-orbit torque and the Dzyaloshinskii-Moriya interaction at a $Ni_{80}Fe_{20}$/Pt interface. *arXiv preprint arXiv: 1611.05798* (2016).

[70] S. Emori, U. Bauer, S.-M. Ahn, E. Martinez, and G.S.D. Beach. Current-driven dynamics of chiral ferromagnetic domain walls. *Nat. Matter.* **12**, 611-616 (2013).

[71] S. Fukami*et al.* Magnetization switching by spin-orbit torque in an antiferromagnet-ferromagnet bilayer system. *Nat. Matter.* **15**, 535-535 (2016).

[72] D. MacNeill, G. M. Stiehl, M. H. D. Guimaraes, R. A. Buhrman, J. Park, and D. C. Ralph*.* Control of spin-orbit torques through crystal symmetry in WTe2/ferromagnet bilayers. *arXiv preprint arXiv:1605.02712* (2016).

[73] Q. Shao, G. Yu, Y.-W. Lan, Y. Shi, M.-Y. Li, C. Zheng, X. Zhu, L.-J. Li, P. K. Amiri, and Kang L. Wang*.* Strong Rashba-Edelstein Effect-Induced Spin-Orbit Torques in Monolayer Transition Metal Dichalcogenides/Ferromagnet Bilayers. *Nano Lett.* (2016).

[74] Y. Fan, P. Upadhyaya, X. Kou, M. Lang, S. Takei, Z. Wang, J. Tang *et al.* Magnetization switching through giant spin–orbit torque in a magnetically doped topological insulator heterostructure. *Nat. Matter.* **13**, 699-704 (2014).

[75] J. E. Hirsch. Spin Hall effect. *Phys. Rev. Lett.* **83**, 1834–1837 (1999).

[76] S. O. Valenzuela and M. Tinkham. Direct electronic measurements of the spin Hall effect. *Nature* **442**, 176–179 (2006).

[77] M. Morota, Y. Niimi, K. Ohnishi, D. H. Wei, T. Tanaka, H. Kontani, T. Kimura, and Y. Otani. Indication of intrinsic spin Hall effect in 4d and 5d transition metals. *Phys. Rev. B* **83**, 174405 (2011).

[78] M. I. Dyakonov and V. I. Perel. Current-induced spin orientation of electrons in semiconductors. *Phys. Lett. A* **35**, 459–460 (1971)

[79] Kato, Y. K., Myers, R. S., Gossard, A. C. & Awschalom, D. D. Observation of the Spin Hall effect in semiconductors. *Science* **306**, 1910–1913 (2004).

[80] T. Wakamura, H. Akaike, Y. Omori, Y. Niimi, S. Takahashi, A. Fujimaki, S. Maekawa, and Y. Otani. Quasiparticle-mediated spin Hall effect in a superconductor. *Nat. Matter.* **14**, 675-678(2015).

[81] J.-C. Rojas-Sánchez, L. Vila, G. Desfonds, S. Gambarelli, J. P. Attané, J. M. De Teresa, C. Magén, and A. Fert*.* Spin-to-charge conversion using Rashba coupling at the interface between non-magnetic materials. *Nat. Comm.* **4**, 2944 (2013).

[82] A. Manchon, H. C. Koo, J. Nitta, S. M. Frolov, and R. A. Duine*.* New perspectives for Rashba spin–orbit coupling. *Nat. Mater.* **14**, 871–882 (2015).

[83] S. Küfner, M. Fitzner, and F. Bechstedt*.* Topological α-Sn surface states versus film thickness and strain. *Phys. Rev*. B **90**, 125312 (2014).

[84] Sinova, J. Valenzuela, S. O. Wunderlich, J. Back, C. H., & Jungwirth, T. Spin Hall effects. *Rev. Mod. Phys.* **87,** 1213(2015).

[85] J. Stephens, R. K. Kawakami, J. Berezovsky, M. Hanson, D. P. Shepherd, A. C. Gossard, and D. D. Awschalom. Spatial imaging of magnetically patterned nuclear spins in GaAs. *Phys. Rev. B* **68**, 041307 (2003).

[86] J. Wunderlich, B. Kaestner, J. Sinova, and T. Jungwirth. Experimental observation of the spin-Hall effect in a two-dimensional spin-orbit coupled semiconductor system. Phys. Rev. Lett. **94**, 047204 (2005).

[87] S. Zhang, Spin Hall effect in the presence of spin diffusion. *Phys. Rev. Lett*. 85, 393 (2000).

[88] K. Ando, M. Morikawa, T. Trypiniotis, Y. Fujikawa, C. H. W. Barnes, and E. Saitoh. Photoinduced inverse spin-Hall effect: Conversion of light-polarization information into electric voltage. *App. Phys. Lett.* **96**, 082502(2010).

[89] H. Zhao, Eric J. Loren, H. M. Van Driel, and Arthur L. Smirl. Coherence control of Hall charge and spin currents. *Phys. Rev. Lett.* **96**, 246601(2006).

[90] Y. Tserkovnyak, A. Brataas, and G. EW Bauer. Enhanced Gilbert damping in thin ferromagnetic films. *Phys. Rev. Lett.* **88**, 117601 (2002).

[91] E. Saitoh, M. Ueda, H. Miyajima, and G. Tatara. Conversion of spin current into charge current at room temperature: Inverse spin-Hall effect. *Appl. Phys. Lett.* **88**, 182509 (2006).

[92] K. Ando, S. Takahashi, K. Harii, K. Sasage, J. Ieda, S. Maekawa, and E. Saitoh. Electric manipulation of spin relaxation using the spin Hall effect. *Phys. Rev. Lett.* **101**, no. 3 (2008): 036601.

[93] L. Liu, Takahiro Moriyama, D. C. Ralph, and R. A. Buhrman. Spin-torque ferromagnetic resonance induced by the spin Hall effect. *Phys. Rev. Lett.* **106**, 036601 (2011).

[94] O. Mosendz, V. Vlaminck, J. E. Pearson, F. Y. Fradin, G. E. W. Bauer, S. D. Bader, and A. Hoffmann. Detection and quantification of inverse spin Hall effect from spin pumping in permalloy/normal metal bilayers. *Phys. Rev. B* **82**, 214403 (2010).

[95] Ando, Kazuya, Saburo Takahashi, Junichi Ieda, Yosuke Kajiwara, Hiroyasu Nakayama, Tatsuro Yoshino, Kazuya Harii et al. Inverse spin-Hall effect induced by spin pumping in metallic system. *J. Appl. Phys.* **109**, 103913 (2011).

[96] A. Azevedo, L. H. Vilela-Leão, R. L. Rodríguez-Suárez, AF Lacerda Santos, and S. M. Rezende. Spin pumping and anisotropic magnetoresistance voltages in magnetic bilayers: Theory and experiment. *Phys. Rev. B* **83**, 144402 (2011).

[97] H. Nakayama, K. Ando, K. Harii, T. Yoshino, R. Takahashi, Y. Kajiwara, K.-i. Uchida, Y. Fujikawa, and E. Saitoh. Geometry dependence on inverse spin Hall effect induced by spin pumping in Ni 81 Fe 19/Pt films. *Phys. Rev. B* **85**, 144408 (2012).

[98] V. Vlaminck, J. E. Pearson, S. D. Bader, and A. Hoffmann. Dependence of spin-pumping spin Hall effect measurements on layer thicknesses and stacking order. *Phys. Rev. B* **88**, 064414 (2013).

[99] L. Bai, P. Hyde, Y. S. Gui, C-M. Hu, V. Vlaminck, J. E. Pearson, S. D. Bader, and A. Hoffmann. Universal method for separating spin pumping from spin rectification voltage of ferromagnetic resonance. *Phys. Rev. Lett.* **111**, 217602 (2013).

[100] V. Castel, N. Vlietstra, J. B. Youssef, and B. t J. van Wees. Platinum thickness dependence of the inverse spin-Hall voltage from spin pumping in a hybrid yttrium iron garnet/platinum system. *App. Phys. Lett.* **10**1, 132414 (2012).

[101] N. Vlietstra, J. Shan, V. Castel, J. Ben Youssef, G. E. W. Bauer, and B. J. Van Wees. Exchange magnetic field torques in YIG/Pt bilayers observed by the spin-Hall magnetoresistance. App. Phys. Lett.**103**,032401(2013).

[102] M. Obstbaum, M. Härtinger, H. G. Bauer, T. Meier, F. Swientek, C. H. Back, and G. Woltersdorf. Inverse spin Hall effect in $Ni_{81}Fe_{19}$/normal-metal bilayers. *Phys. Rev. B* **89**, 060407(2014).

[103] K. Kondou, H. Sukegawa, S. Mitani, K. Tsukagoshi, and S. Kasai. Evaluation of spin Hall angle and spin diffusion length by using spin current-induced ferromagnetic resonance. *Appl. Phys. Exp.* **5**, 073002 (2012).

[104] M.-H. Nguyen, D. C. Ralph, and R. A. Buhrman. Spin torque study of the spin Hall conductivity and spin diffusion length in platinum thin films with varying resistivity. *Phys. Rev. Lett.* **116**, 126601 (2016).

[105] L. Liu, C. F. Pai, Y. Li, H. W. Tseng, D. C. Ralph, and R. A. Buhrman. Spin-torque switching with the giant spin Hall effect of tantalum. *Science* **336**, 555-558 (2012).

[106] K. Ando, and E. Saitoh. Inverse spin-Hall effect in palladium at room temperature. *J. Appl. Phys.* **108**, 113925 (2010).

[107] C.T. Boone, H. T. Nembach, J. M. Shaw, and T. J. Silva. Spin transport parameters in metallic multilayers determined by ferromagnetic resonance measurements of spin-pumping. *J. Appl. Phys.* **113**, 153906 (2013).

[108] P. Laczkowski, J. C. Rojas-Sánchez, W. Savero-Torres, N. Reyren, C. Deranlot, J.-M. George, H. Jaffres *et al.* Extrinsic Spin Hall effect of AuW alloys. In *APS Meeting Abstracts*. 2016.

[109] K. Ando, and Eiji Saitoh. Observation of the inverse spin Hall effect in silicon. *Nat. Comm.* **3**, 629 (2012).

[110] M. Johnson, and R. H. Silsbee. Interfacial charge-spin coupling: Injection and detection of spin magnetization in metals. *Phys. Rev. Lett.* **55**, 1790 (1985).

[111] S. O. Valenzuela, and M. Tinkham. Electrical detection of spin currents: the spin-current induced Hall effect. *J. Appl. Phys*. **101**, 09B103 (2007).

[112] K. Olejník, J. Wunderlich, A. C. Irvine, R. P. Campion, V. P. Amin, J. Sinova, and T. Jungwirth. Detection of electrically modulated inverse spin Hall effect in an Fe/GaAs microdevice. *Phys. Rev. Lett.* **109**, 076601 (2012).

[113] L. Vila, T. Kimura, and Y. Ch. Otani. Evolution of the spin Hall effect in Pt nanowires: size and temperature effects. *Phys. Rev. Lett.* **99**, 226604 (2007).

[114] P. Laczkowski, J-C. Rojas-Sánchez, W. Savero-Torres, H. Jaffrès, N. Reyren, C. Deranlot, L. Notin et al. Experimental evidences of a large extrinsic spin Hall effect in AuW alloy. *App. Phys. Lett.* **104**, 142403 (2014).

[115] Y. Niimi, M. Morota, D. H. Wei, Cyrile Deranlot, M. Basletic, A. Hamzic, Albert Fert, and Y. Otani. Extrinsic spin Hall effect induced by iridium impurities in copper. *Phys. Rev. Lett.* **106**, 126601 (2011).

[116] K. Fujiwara, Y. Fukuma, J. Matsuno, H. Idzuchi, Y. Niimi, Y. C.Otani, and H. Takagi. 5d iridium oxide as a material for spin-current detection. *Nat. Comm.* **4**m 2893-2893 (2013).

[117] D. H. Wei, Yasuhiro Niimi, Bo Gu, Timothy Ziman, Sadamichi Maekawa, and Yoshichika Otani. The spin Hall effect as a probe of nonlinear spin fluctuations. *Nat. Comm.* **3**, 1058 (2012).

[118] H. Nakayama, M. Althammer, Y-T. Chen, K. Uchida, Y. Kajiwara, D. Kikuchi, T. Ohtani et al. Spin Hall magnetoresistance induced by a nonequilibrium proximity effect. *Phys. Rev. Lett.* **110**, 206601 (2013).

[119] M. Isasa, A. Bedoya-Pinto, S. Vélez, F. Golmar, F. Sánchez, L. E. Hueso, J. Fontcuberta, and F. Casanova. Spin Hall magnetoresistance at Pt/CoFe2O4 interfaces and texture effects. *App. Phys. Lett.* **105**, 142402 (2014).

[120] N. Vlietstra, J. Shan, V. Castel, B. J. van Wees, and J. Ben Youssef. Spin-Hall magnetoresistance in platinum on yttrium iron garnet: Dependence on platinum thickness and in-plane/out-of-plane magnetization. *Phys. Rev. B* **87**, 184421 (2013).

[121] M. Ehlert, C. Song, M. Ciorga, M. Utz, D. Schuh, D. Bougeard, and D. Weiss. All-electrical measurements of direct spin Hall effect in GaAs with Esaki diode electrodes. *Phys. Rev. B* **86**, 205204 (2012).

[122] L. Liu, Ching-Tzu Chen, and J. Z. Sun. Spin Hall effect tunnelling spectroscopy. *Nat. Phys.* **10**, 561-566 (2014).

[123] V. Sih, R. C. Myers, Y. K. Kato, W. H. Lau, A. C. Gossard, and D. D. Awschalom. Spatial imaging of the spin Hall effect and current-induced polarization in two-dimensional electron gases. *Nat. Phys.* **1**, 31–35 (2005).

[124] J. Wunderlich, B.-G. Park, A. C. Irvine, L. P. Zârbo, E. Rozkotová, P. Nemec, V. Novák, J.Sinova, and T. Jungwirth. Spin Hall effect transistor. *Science* **330**, 1801-1804 (2010).

[125] C. Brüne, A. Roth, E. G. Novik, M. König, H. Buhmann, E. M. Hankiewicz, W. Hanke, J. Sinova, and L. W. Molenkamp. Evidence for the ballistic intrinsic spin Hall effect in HgTe nanostructures. *Nat. Phys*. **6**, 448-454 (2010).

[126] E. M. Hankiewicz*et al.* Manifestation of the spin Hall effect through charge-transport in the mesoscopic regime. *Phys. Rev. B* **70**, 24 24130 (2004).

[127] E. S. Garlid, Q. O. Hu, M. K. Chan, C. J. Palmstrøm, and P. A. Crowell. Electrical measurement of the direct spin Hall effect in Fe/In x Ga 1− x As heterostructures. *Phys. Rev. Lett.* **105**, 156602 (2010).

[128] M. Isasa, M. C. Martínez-Velarte, E. Villamor, C. Magén, L. Morellón, J. M. De Teresa, M. R. Ibarra *et al.* Origin of inverse Rashba-Edelstein effect detected at the Cu/Bi interface using lateral spin valves. *Phys. Rev. B* **93**, 014420 (2016).

[129] Y. Niimi, Y. Kawanishi, D. H. Wei, C. Deranlot, H. X. Yang, M. Chshiev, T. Valet, A. Fert, and Y. Otani. Giant spin Hall effect induced by skew scattering from bismuth impurities inside thin film CuBi alloys. *Phys. Rev. Lett.* **109**, 156602 (2012).

[130] T. Kimura, Y. Otani, T. Sato, S. Takahashi, and S. Maekawa. Room-temperature reversible spin Hall effect. *Phys. Rev. Lett.* **98,** 156601 (2007).

[131] D.H. Wei, Y. Niimi, B. Gu, T. Ziman, S. Maekawa, and Y. Otani. The spin Hall effect as a probe of nonlinear spin fluctuations. *Nat. Comm.* **3**, 1058 (2012).

[132] M. Morota, Y. Niimi, K. Ohnishi, D. H. Wei, T. Tanaka, H. Kontani, T. Kimura, and Y. Otani. Indication of intrinsic spin Hall effect in 4 d and 5 d transition metals. *Phys. Rev. B* **83**, 174405 (2011).

[133] G. Zahnd, L. Vila, T. V. Pham, A. Marty, P. Laczkowski, W. Savero Torres, C. Beigné, C. Vergnaud, M. Jamet, and J. P. Attané. Comparison of the use of NiFe and CoFe as electrodes for metallic lateral spin-valves. *Nanotech.* **27**, 035201 (2015).

[134] Liu, Yi, Zhe Yuan, R. J. H. Wesselink, Anton A. Starikov, Mark van Schilfgaarde, and Paul J. Kelly. Direct method for calculating temperature-dependent transport properties. *Phys. Rev. B* **91**, 220405 (2015).

[135] J.-C. Rojas-Sánchez, N. Reyren, P. Laczkowski, W. Savero, J.P. Attané, C. Deranlot, M. Jamet, J. M. George, L. Vila and H. Jaffrès. Spin pumping and inverse spin hall effect in platinum: the essential role of spin-memory loss at metallic interfaces. *Phys. Rev. Lett.* **112**,106602 (2014).

[136] M. Isasa, E. Villamor, L. E. Hueso, M. Gradhand, and F. Casanova. Temperature dependence of spin diffusion length and spin Hall angle in Au and Pt. *Phys. Rev. B* **91**, 024402 (2015).

[137] Donahue, Michael Joseph, and Donald Gene Porter. *OOMMF User's guide*. US Department of Commerce, Technology Administration, National Institute of Standards and Technology, 1999.

[138] W. W. Schulz, Philip B. Allen, and Nandini Trivedi. Hall coefficient of cubic metals. *Phys. Rev. B* **45**.19 10886(1992).

[139] E. Sagasta, Y. Omori, M. Isasa, M. Gradhand, L. E. Hueso, Y. Niimi, Y.C. Otani, and F. Casanova. Tuning the spin Hall effect of Pt from the moderately dirty to the superclean regime. *Phys. Rev. B* **94**, 060412(R) (2016).

[140] Z. Feng, J. Hu, L. Sun, B. You, D. Wu, J. Du, W. Zhang et al. Spin Hall angle quantification from spin pumping and microwave photoresistance. *Phys. Rev. B* **85**, 214423 (2012).

[141] H. Y. Hung, G. Y. Luo, Y. C. Chiu, P. Chang, W. C. Lee, J. G. Lin, S. F. Lee, M. Hong, and J. Kwo. Detection of inverse spin Hall effect in epitaxial ferromagnetic Fe3Si films with normal metals Au and Pt. *J. Appl. Phys.* **113**, 17C507 (2013).

[142] W. Zhang, V. Vlaminck, J. E. Pearson, R. Divan, S. D. Bader, and A. Hoffmann. Determination of the Pt spin diffusion length by spin-pumping and spin Hall effect*. App. Phys. Lett.***103**, 242414 (2013).

[143] X. Wang, C. O. Pauyac, and A. Manchon. Spin-orbit-coupled transport and spin torque in a ferromagnetic heterostructure. *Phys. Rev. B* **89**, 054405 (2014).

[144] A. Ganguly, K. Kondou, H. Sukegawa, S. Mitani, S. Kasai, Y. Niimi, Y. Otani, and A. Barman. Thickness dependence of spin torque ferromagnetic resonance in Co75Fe25/Pt bilayer films. *App. Physi. Lett.* **104**, 072405 (2014).

[145] C.-F. Pai, Y. Ou, L. H. Vilela-Leão, D. C. Ralph, and R. A. Buhrman. Dependence of the efficiency of spin Hall torque on the transparency of Pt/ferromagnetic layer interfaces.Phys. Rev. B **92**, 064426(2015).

[146] W. Zhang, Han, W., Jiang, X., Yang, S. H., and S. S. Parkin. Role of transparency of platinum-ferromagnet interfaces in determining the intrinsic magnitude of the spin Hall effect. *Nat. Phys.* **11**, 496–502 (2015).

[147] M. Althammer, S. Meyer, H. Nakayama, M. Schreier, S. Altmannshofer, M. Weiler, H. Huebl *et al.* Quantitative study of the spin Hall magnetoresistance in ferromagnetic insulator/normal metal hybrids. *Phys. Rev. B* **87**, 224401(2013).

[148] L. Liu, A. Richardella, I. Garate, Y. Zhu, N. Samarth, and C.-T. Chen. Spin-polarized tunneling study of spin-momentum locking in topological insulators. *Phys. Rev.* B **91**, 235437 (2015).

[149] A. Dankert, J. Geurs, M. V. Kamalakar, S. Charpentier, and S. P. Dash. Room temperature electrical detection of spin polarized currents in topological insulators. *Nano Lett.* **15**, 7976-7981 (2015).

[150] J. Kim, P. Sheng, S. Takahashi, S. Mitani, and M. Hayashi. Spin Hall magnetoresistance in metallic bilayers. *Phys. Rev. Lett.* **116**, 097201 (2016).

[151] C. Hahn, G. de Loubens, O. Klein, M. Viret, V. V. Naletov, and J. B. Youssef. Comparative measurements of inverse spin Hall effects and magnetoresistance in YIG/Pt and YIG/Ta. *Phys. Rev. B* **87**, 174417 (2013).

[152] C. Du, H.Wang, F. Yang, and P. C. Hammel. Systematic variation of spin-orbit coupling with d-orbital filling: Large inverse spin Hall effect in 3d transition metals. *Phys. Rev. B* **90**, 140407 (2014).

[153] P. Laczkowski. Spin currents and spin Hall effect in lateral nano-structures. PhD thesis, Unv. Grenoble, 2012.

[154] P. Laczkowski *et al.* Large Spin Hall Angles driven by side jump mechanisms in Gold Based Alloys. Phys. Rev. Lett. (Submitted)

[155] J-C. Rojas-Sánchez, S. Oyarzún, Y. Fu, A. Marty, C. Vergnaud, S. Gambarelli, L. Vila *et al.*. Spin to Charge Conversion at Room Temperature by Spin Pumping into a New Type of Topological Insulator: α-Sn Films. *Phys. Rev. Lett.* **116**, 096602(2016).

[156] W. Gil, D. Görlitz, M. Horisberger, and J.Kötzler. Magnetoresistance anisotropy of polycrystalline cobalt films: Geometrical-size and domain effects. *Physical Review B* **72**, 134401 (2005).

[157] E. Villamor, M. Isasa, L. E. Hueso, and F. Casanova. Temperature dependence of spin polarization in ferromagnetic metals using lateral spin valves. *Physical Review B* **88**,184411(2013).

[158] Y. Liu, Z. Yuan, R. J. H. Wesselink, A. A. Starikov, and P. J. Kelly. Interface enhancement of Gilbert damping from first principles. *Phys. Rev. Lett.* **113**, 207202 (2014).

[159] L. Berger. Exchange interaction between ferromagnetic domain wall and electric current in very thin metallic films. *J. Appl. Phys*. **55**, 1954-1956 (1984).

[160] O. Boulle, G. Malinowski, and M. Kläui. Current-induced domain wall motion in nanoscale ferromagnetic elements. *Mater. Sci. Eng.: R: Rep.* **72**, 159-187(2011).

[161] D. Ilgaz, J. Nievendick, L. Heyne, D. Backes, J. Rhensius, T. A. Moore, M. Á. Niño *et al.* Domain-wall depinning assisted by pure spin currents. *Phys. Rev. Let*. **105**, 076601(2010).

[162] N. Motzko, B. Burkhardt, N. Richter, R. Reeve, P. Laczkowski, W. Savero Torres, L. Vila, J.-P. Attané, and M. Kläui. Pure spin current-induced domain wall motion probed by localized spin signal detection. *Phys. Rev. B* **88**, 214405 (2013).

[163] A. Brataas and M.D. H. Kjetil. Spin-orbit torques in action. Nat. Nanotech. **9**, 86-88 (2014).

[164] S. S. P. Parkin, M. Hayashi, and L. Thomas. Magnetic domain-wall racetrack memory. *Science* **320**, 190-194 (2008).

[165] S. Fukami, N. Ishiwata, N. Kasai, M. Yamanouchi, H. Sato, S. Ikeda, and H. Ohno. Scalability prospect of three-terminal magnetic domain-wall motion device. *IEEE Transac. Magn.* **48**, 2152-2157 (2012).

[166] W. Savero Torres, P. Laczkowski, V. D. Nguyen, J. C. Rojas Sanchez, L. Vila, A. Marty, M. Jamet, and J. P. Attane. Switchable Spin-Current Source Controlled by Magnetic Domain Walls. *Nano Lett.* **14**, 4016-4022(2014).

[167] W. Savero Torres, V. T. Pham, G. Zahnd, P. Laczkowski, V-D. Nguyen, C. Beigné, L. Notin *et al.* Using domain walls to perform non-local measurements with high spin signal amplitudes. *Appl. Phys. Lett.* **109**, 042405(2016).

[168] V. T. Pham, L. Vila, G. Zahnd, A. Marty, W. Savero Torres, M. Jamet, and J.-P. Attané. Ferromagnetic/nonmagnetic nanostructures for the electrical measurement of the Spin Hall effect. *Nano Lett.* **16**, 6755-6760. (2016).

[169] V. D. Nguyen, C. Naylor, L. Vila, A. Marty, P. Laczkowski, C. Beigne, L. Notin, Z. Ishaque, and J. P. Attane. Magnon magnetoresistance of NiFe nanowires: Size dependence and domain wall detection. *Appl. Phys. Lett.* **99**, 262504(2011).

[170] T. Kimura, J. Hamrle, and Y. Otani. Spin-polarized current induced in a single ferromagnetic strip due to inhomogeneous spin injection. *J. Appl. Phys.* **97**, 76102-76102 (2005).

[171] S. Chen, C. Qin, and Y. Ji. Asymmetric spin absorption across a low-resistance oxide barrier. *J. Appl. Phys.* **118**, 033901 (2015).

[172] G. Zahnd, V. T. Pham, A. Marty, M. Jamet, C. Beigné, L. Notin, C. Vergnaud, F. Rortais, L. Vila, and J-P. Attané. Introduction and pinning of domain walls in 50nm NiFe constrictions using local and external magnetic fields. *J. Magn. Magn. Matter.* **406**, 166-170 (2016).

173 T. S. Kim, B. C. Lee, and H.-W. Lee. Effect of ferromagnetic contacts on spin accumulation in an all-metallic lateral spin-valve system: Semiclassical spin drift-diffusion equations. *Phys. Rev. B* **78**, 214427 (2008).

[174] Geuzaine C. and Remacle J.-F., Gmsh: A 3-D finite element mesh generator with built-in pre- and post-processing facilities. *J. Numer. Methods Eng*. **79**, 1309 (2009).

[175] Geuzaine C. GetDP: a general finite-element solver for the de Rham complex. *Proc. Appl. Math. Mech.* **7**, 1010603 (2007).

[176] T. Schulz, Alejos, O., Martinez, E., Hals, K.M., Garcia, K., Vila, L., Lee, K., Lo Conte, R., Karnad, G.V., Moretti, S. and Ocker, B. Spin-orbit torques for current parallel and perpendicular to a domain wall. *Appl. Phys. Lett.* **107,** 122405 (2015).

[177] A. V. Khvalkovskiy, *V. Cros, D. Apalkov, V. Nikitin, M. Krounbi, K. A. Zvezdin, A. Anane, J. Grollier, and A. Fert.* Matching domain-wall configuration and spin-orbit torques for efficient domain-wall motion. *Physical Review B* **87**, 020402(2013).

[178] O. BoulleM L. D. Buda-Prejbeanu, E. Jué, I. M. Miron, and G. Gaudin. Current induced domain wall dynamics in the presence of spin orbit torques. *J. App. Phys.* **115**, 17D502 (2014).

[179] D. Bhowmik, M. E. Nowakowski, L. You, O.J. Lee, D. Keating, M. Wong, J. Bokor, and S. Salahuddin*.* Deterministic domain wall motion orthogonal to current flow due to spin orbit torque. *arXiv preprint arXiv:1407.6137* (2014).

[180] F. Cayssol, D. Ravelosona, C. Chappert, J. Ferré, and J. P. Jamet. Domain wall creep in magnetic wires. *Phys. Rev. Lett.* **92**, 107202 (2004).